LBL-38210
UC-400

Lawrence Berkeley Laboratory

UNIVERSITY OF CALIFORNIA

EARTH SCIENCES DIVISION

Rayleigh Scattering and Nonlinear Inversion of Elastic Waves

R. Gritto
(Ph.D. Thesis)

December 1995

Prepared for the U.S. Department of Energy under Contract Number DE-AC03-76SF00098

LBL - 38210
UC - 400

Rayleigh Scattering and Nonlinear Inversion of Elastic Waves

Roland Gritto

(Ph.D. Thesis)

Department of Geology and Geophysics
University of California, Berkeley

and

Earth Sciences Division
Ernest Orlando Lawrence Berkeley National Laboratory
University of California
Berkeley, CA 94720

December 1995

This work was done at the Center for Computational Seismology supported by the Director, Office of Energy Research, Office of Basic Energy Sciences of the U.S. Department of Energy under Contract No. DE-AC03-76SF00098.

Rayleigh Scattering and Nonlinear Inversion of Elastic Waves

by

Roland Gritto

Diplom (Ruhr-Universität Bochum) 1989

A dissertation submitted in partial satisfaction of the requirements for

the degree of

Doctor of Philosophy

in

Geophysics

in the

GRADUATE DIVISION

of the

UNIVERSITY of CALIFORNIA at BERKELEY

Commitee in charge:

Professor Lane R. Johnson, Chair

Professor Thomas V. McEvilly

Professor Neville G. W. Cook

1995

Rayleigh Scattering and Nonlinear Inversion of Elastic Waves

by

Roland Gritto

Abstract

Rayleigh Scattering and Nonlinear
Inversion of Elastic Waves
by
Roland Gritto
Doctor of Philosophy in Geophysics
University of California at Berkeley
Professor Lane R. Johnson, Chair

Rayleigh scattering of elastic waves by an inclusion is investigated and the limitations determined. In the near field of the inhomogeneity, the scattered waves are up to a factor of 300 stronger than in the far field, excluding the application of the far field Rayleigh approximation for this range. The investigation of the relative error as a function of parameter perturbation shows a range of applicability broader than previously assumed, with errors of 37% and 17% for perturbations of -100% and +100%, respectively. The validity range for the Rayleigh limit is controlled by large inequalities, and therefore, the exact limit is determined as a function of various parameter configurations, resulting in surprisingly high values of up to $k_pR = 0.9$. The nonlinear scattering problem can be solved by inverting for equivalent source terms (moments) of the scatterer, before the elastic parameters are determined. The nonlinear dependence between the moments and the elastic parameters reveals a strong asymmetry around the origin, which will produce different results for weak scattering approximations depending on the sign of the anomaly. Numerical modeling of cross hole situations shows that near field terms are important to yield correct estimates of the inhomogeneities in the vicinity of the receivers, while a few well positioned sources and receivers considerably increase the angular coverage, and thus the model resolution of the inversion parameters. The pattern of scattered energy by an inhomogeneity is complicated and varies depending on the object, the wavelength of the incident wave, and the elastic parameters involved.

Therefore, it is necessary to investigate the direction of scattered amplitudes to determine the best survey geometry. The inversion of a cross hole dataset to determine the location and elastic parameters of a fracture zone reveals the following results. The bulk modulus appears to be sensitive to voids and welded contacts, whereas the density is mostly affected by fractured zones. The shear modulus is least constrained, possibly due to the absence of S wave anisotropy information. However, P wave anisotropy is included and prevents the collapse of linear features into block-like structures during the inversion.

Meinen Eltern

(To My Parents)

Acknowledgements

When I came to Berkeley in the Fall of 1990, I did not know what to expect, but I was looking forward to absorb whatever may come. My hopes were not disappointed, as this is the most buzzing place I have ever attended to get an education, and I doubt that this will be topped in the future. Many people I met at Berkeley have had a big effect on my education and on my personal development, and this I will remember forever.

I was fortunate to work with a group of first class scientists which made this thesis, and whatever may follow, possible. My sincere gratitude goes to Lane Johnson, my advisor, who I admire for his scientific brilliance, his modest character (a rare combination in itself), and his never ending effort to be available to students and to help with scientific advice or financial support, and this not only for his own students. He created an atmosphere in which is was a pleasure to do research. Lane, you have my fullest admiration, and I will try to follow your example.

Tom McEvilly receives my sincere thanks, for providing a splendid working environment where we could generate and explore ideas and work free of all bureaucratic worries. I also would like to thank him for his willingness and efforts to review my thesis during a time when he was busy deploying seismometers in New Zealand. Thank you Tom for watching out for the FedEx truck every day.

I am grateful to Neville Cook for his willingness and interest to serve on my qualifying committee and to review my thesis during times of personal hardship. Neville, I wish you all the best for the future.

The examples above thought me how much the people at Berkeley are devoted to science and research and how stimulating this environment can be.

Valeri Korneev is without doubt the person who had the biggest impact on my thesis. I had no idea how fortunate I was, when I decided, based on Lane's suggestion, to collaborate with him and apply his theory to my problem. What followed was an intense school of scientific and cultural exchange that lead to one of the most fruitful experiences I had during my time at Berkeley. I still recall

the seemingly endless nights at the lab during his visits from Australia, and the miraculous recovery from exhaustion, after we finally got home and started to discuss world affairs over a good brew or a brandy until early in the morning. Many times we were sitting around, I worried about an insurmountable problem, and he just smiled and said "that reminds me of a Russian anecdote...". As usual he knew the answers already, or pulled it out of his vast mathematical knowledge. Lane once said that Valeri is more of an advisor to me than he can be himself, which shows how much time Valeri was willing to invest in my thesis. His name would be most appropriate on the approval page... There were many situations when we were uncertain, whether this approach would be applicable to the real world, and many times Valeri called me a "brave student" (or should he have said bold?), however, the moment that provided the strongest motivation for me came, when he once said he would feel like he made an accomplishment the day I would succeed in applying his approach to solve new geophysical problems. And in this sense I can tell you Valeri, this is just the beginning. Thanks for being such a good friend all this time.

I would like to thank my "office" mates Art Romero for many fruitful discussions on inversion theory and help on programming questions, and Bob Nadeau for his wizard-like knowledge on how to use UNIX to make all kind of impossible things possible, and for his relentless efforts in reminding me that there is such thing as a characteristic micro- earthquake. I also appreciate his questionable attempts to keep the mess on his desk from spreading throughout our "office". Never mind Bob, keep trying.

Tom Daley was always there to answer my questions when I was introduced to this new computer environment, as did John Peterson when I processed data that he measured years ago. Thanks for your great memory John. At the same time I would like to express my gratitude to Ernie Majer who manages CCS and always finds a way to spoil us with new terminals before we have a chance to get used to the old ones. I'm sure I will miss CCS even more, after I have left and had a chance to compare it to other places. Chuck Wicks and Rouben Amirbekian were always my strongholds on campus who I could freely discuss

many ideas with.

Outside academia (does that part of the world still exist?) I shared good times with many people. At the beginning it was Annette, Ann and Juan who helped to provide a nice transition from the wild Aussie life to the not much tamer campus environment. Andrea, Brit, Jan, Florian, Kristin, Lenise, Nelson, Rachel, Ray, Carlos, Anette, Paul, Ken, Bruno, Patty and Chaincy were great friends throughout most of my time outside the lab. Thank you for the many parties, skiing weekends, surf trips, game nights, soccer matches, coffees, beers, and salsa lessons we shared. It will be a lasting memory. Special thanks to Ann and John for introducing me to the wild world of white water rafting.

However, this all happened at Berkeley and there were many people working behind the scenes back "home". I would like to acknowledge the financial support of the DAAD, and personally Birgitt Böhme who helped me to secure support for an unprecedented 3 year tenure. But even without her management skills, she's the best that could have happened to the DAAD, as she always finds a personal link to the students in the new world and cares, beyond the financial needs, about the personal well-being as well. Even if that means reporting the weekly soccer results of the home team. Thanks a bunch, Birgitt.

There are many more friends back home that deserve to be acknowledged in here. However, there is a deadline for this thesis and I feel an urge to meet it. So let me thank you all, and you know who I mean, for always welcoming me with open arms during my visits back home, and in many cases for finding the long way out here to California to share with me and learn about my new life.

What I have accomplished so far, I owe to my family. Throughout these years from childhood to the very day, they have supported my in every possible way. Although it was not always easy, they never questioned my dreams and wishes. My sister Beate was always a reliable liaison, willing to help on last minute notice (which was usually the case). I never heard her complain she was to busy (which I too often said in recent months), I'll try to make it up to you. It was no easy decision to leave six years ago, particular under the circumstances, but my mother Luise and my father Wolfgang never questioned

my wish to go, which made it much easier for me. Although my father did not live to see this day, I'm sure he knew what I was leading to. To both of you I owe this accomplishment and therefore, I dedicate this thesis to you.

Thank you, I love you all.

Contents

Chapter 1

Introduction

Elastic waves propagating through the Earth are affected by structures on all scale lengths. These scale lengths range from several hundreds of kilometers for e.g. the core mantle boundary and subducting slabs, over several tens of kilometers for crustal structures, to a meter or less in heterogeneous surface layers.

The waves are affected by the inhomogeneities in several ways. Their travel time is delayed or advanced, depending on the nature of the inhomogeneity (Peterson, 1986; Nolet, 1987), and energy is scattered throughout the medium arriving at different times at the point of observation (Aki and Chouet, 1975). Furthermore, the direction of propagation is changed for most of the propagating energy every time the waves are reflected or refracted by inhomogeneities. In addition, zones of anelastic attenuation decrease the amplitude of the waves and dissipate their energy throughout the medium. The degree to which the waves are affected is a function of their wavelength in relation to the size of the inhomogeneities. The problem of propagating waves with small wavelengths through inhomogeneities of large scale length can be treated, to a certain degree, as wave propagation through a blockwise homogeneous medium, whereas waves with wavelengths on the scale of the inhomogeneities are best treated as scattering at the interfaces. Therefore, the question of which process best describes wave propagation through a medium depends on the frequencies and scale lengths under investigation.

Seismologists use the different effects on wave propagation to deduce parameters of the medium. Travel time changes are employed to derive velocity

perturbations (Aki et al.; 1976, Toomey et al., 1989), while changes in the amplitudes are used to determine elastic properties, such as the elastic moduli and the density, as well as intrinsic attenuation (Scherbaum, 1990; Romero, 1995). However, in recent years the demand to use seismic waves as a diagnostic tool to estimate high resolution models of the subsurface and to extract a variety of parameters, which can further be used to model subsurface processes, has increased. Despite this need to determine parameters beyond elastic wave velocities, most waveform approaches that utilize amplitude information solve for velocities rather than the elastic parameters of the medium (Wu et al., 1987, Lo et al., 1988; Tura et al., 1992). However, medium parameters, as represented by the elastic moduli, may not be correctly determined by velocities, as the moduli may cancel or reduce their effect in the equations of the velocities (Gritto et al., 1995b). Consequently the magnitude of changes in the subsurface structures may be larger in the elastic moduli. Therefore, the intention of this work is to study elastic wave scattering and to use scattered wavefields to invert for the elastic parameters mentioned above.

The present work is not submitted as a finished study; rather it is an attempt to investigate the feasibility to extract information from scattered waves that may provide more insight into the elastic parameters of the medium. In the past, various inversion techniques have been developed, each of which is applicable to certain conditions under which it works most favorably. Travel time tomography utilizes the first arrival time of the direct wave to determine the velocity structure of the medium. In order to invert for attenuation properties, the amplitudes of the first arrival are estimated to determine its variation over the path of propagation. These techniques use the properties of the direct wave in seismograms. In contrast, waveform algorithms are based on amplitude information evident in later phases, to determine the velocity structure and anelastic properties of the medium. However, these methods almost never use the full content of information present in the seismogram, but rather use the properties of P and S waves. All of these methods have in common that they neglect phases that appear after the main arrival of the direct body waves, although

these late phases may carry information about the medium properties. Therefore, a thorough study of the scattered phases is essential to determine whether their properties can reveal a more detailed picture of the subsurface structure. The present approach differs from other inversion techniques by the fact that it does not use the first direct arrival, but incorporates all scattered phases that appear at later times in the seismogram, and therefore, it is important to remove this energy before a successful inversion can be performed.

The techniques utilizing the scattered phases in seismograms are often referred to as diffraction tomography. The goal of these techniques is the location and determination of elastic parameters of the medium (Devaney, 1984; Woodward, 1992), and in this sense they are similar to the present approach. The advantage of these techniques is that their mathematical treatment is based on simplified far field Green functions. The inversion is performed in the frequency wavenumber (f-k) domain, where the resolving power of the inversion operator can be studied and the experimental design adjusted accordingly (Tura et al., 1993). However, the disadvantage of these techniques is that they rely on regular source and receiver spacing to allow the transformation into the f-k domain. In contrast, the present approach is based on an analytical solution that provides a more complete treatment of the scattering process. In addition, it does not rely on a regular source receiver geometry, but is capable of treating any irregular sized 3-dimensional geometry.

A commonly used imaging technique in exploration seismology is seismic migration. The idea is to determine the origin of reflected phases in seismogram sections. The amplitudes of these reflected phases are integrated along the reflection hyperbola over many traces and the result collapsed, or migrated, into the point of origin (Tygel et al. 1994, Yilmaz, 1987). Thus, assuming a background velocity model, interfaces reflecting energy in the subsurface can be pointwise reconstructed. The analogy to the technique presented in this thesis is that the inversion of scattered waves can be interpreted as integration along the hyperbola of scattered phases, and the result, under the assumption that the background parameters are known, collapsed into the location of the scattering

object. In addition to the location, the present method estimates the elastic parameters as well. However, in a strict sense, this approach is not a seismic migration technique.

The process of wave scattering by an inhomogeneous medium is of a complicated nature, and therefore, a thorough investigation is essential before scattered amplitudes can be converted to information of the subsurface structure. Consequently this study first investigates the problems arising in elastic wave scattering and incorporates the results to improve the inversion for medium parameters.

In order to evaluate the scattering of elastic waves by inhomogeneities, exact solutions are needed, some of which are available for simplified geometries. But even for these cases, as the exact solutions are difficult to implement, asymptotic approximations are developed. However, most of these approximations are based on assumptions which do not have fixed limits, and therefore, it is not always clear when the results are valid.

Chapter 2 investigates the validity range and the limitation of the low frequency Rayleigh approximation to the analytic solution for the scattering of elastic waves by a sphere shaped inhomogeneity. The Rayleigh approximation is a widely applied tool in waveform inversion algorithms, as it provides a means to linearize the inherently nonlinear problem of solving for the elastic parameters of the inhomogeneity. However, thus far no attempt has been undertaken to establish limitations for this approximation and strong inequalities are used to justify its application. Therefore, in order to qualify results determined through the use of the Rayleigh approximation, its limitations are tested and determined.

Once the process of scattering is better understood and limitations are established, information of the scattered amplitudes can be used to determine the properties of the inhomogeneity. Although this process is nonlinear in terms of the elastic parameters, Chapter 3 offers a direct solution to this problem based on the low frequency Rayleigh approximation under the assumption that scatterers can be represented by simplified geometries. The advantage of this method is a fast and direct way to solve for the elastic parameters without

limitations on the scatterer strength. Additionally, a time consuming iterative process to solve for strong contrasts can be avoided. Although this theory opens the field for a wider class of scatterers, it requires a better understanding of the scattering process. It will be shown that near field terms play an important role in cross hole geometries if the Rayleigh approximation is applied to invert the scattered wavefield. The direction of the scattered energy strongly depends on the strengths of the inhomogeneity and consequently, a successful field experiment requires a thorough study of the scattering process to optimize source and receiver geometries. Based on this fact, various numerical experiments are presented to address the aspect of optimum source and receiver geometries. The case of a high velocity inclusion with a reduction in density only, will be used to study the resolving power of the inversion to solve for a single elastic parameter without affecting the constant parameters.

Finally, Chapter 4 applies this new approach to a field experiment where the objective is to determine the location and the elastic parameters of a fractured zone in an otherwise undisturbed host rock. The challenge in this problem lies in the fact that the fracture zone, based on the theory, has to be modeled by a series of small inhomogeneities each representing a single scatterer. The success of such an experiment could lead to the treatment of a completely new class of irregularly shaped inhomogeneities represented by a series of single scatterers for the inversion of full waveform data.

Chapter 2

Low-Frequency Elastic Wave Scattering by an Inclusion

2.1 Introduction

Scattering of seismic waves is a fundamental process in the propagation of waves through the Earth. In recent years, numerous authors have turned to the theory of scattering to describe the complicated nature of seismograms that occur in various places, believed to be caused by inhomogeneities and sequences of layering within the structure of the Earth. Different scale lengths are the focus of attention, varying from mantle (Haddon and Cleary, 1974; Doornbos, 1976; Aki, 1980), over crustal (Aki, 1969; Wu, 1982; Sato, 1984), to regional and even local scales on the order of a few meters (Wu and Aki, 1985; Herraiz and Espinosa, 1987; Sams and Goldberg, 1990). The common objective of these studies is to apply statistical approaches to determine the heterogeneity and the elastic parameters of the medium and to distinguish between different attenuation processes like intrinsic and scattering attenuation (Frankel and Clayton, 1986; Frankel and Wennerberg, 1987; Frankel, 1991). Lately, the theory of localization, well established in quantum mechanics, solid state physics and optics, was introduced to seismology (O'Doherty and Anstey, 1971) to investigate scattering processes during propagation, and to determine possible limits in wave propagation (Richards and Menke, 1983; White, Sheng, Zang and Papanicolaou, 1987; White, Sheng and Nair, 1990), although presently it is unclear whether the common approach of treating the Earth as a self averaged

random medium is valid (Shapiro and Zien, 1993).

As an alternative to statistical methods, deterministic approaches are a valuable tool to estimate local parameters by measuring their properties in the medium. Such approaches require exact solutions for the scattering problem, but only a few exist for special cases. Even though these cases are based on simplified geometries for the numerous shapes and sizes of inhomogeneities that are present in the Earth, they are difficult to implement, and hence solutions in terms of asymptotic approximations are developed. The assumptions used in the derivation of asymptotic solutions are usually expressed in the form of strong inequalities where some combination of parameters is assumed to be much less or much larger than unity. For instance, for the case of Rayleigh scattering it is assumed that the parameter kR, where k is the wavenumber of the incident wave and R is the radius of the scatterer, satisfies the condition $kR \ll 1$. In the same manner, for the case of linearizing the inverse problem, we assume "very small" relative deviations of elastic parameters and density. Such assumptions are convenient at the stage of mathematical development, but they present problems when attempting to determine the actual bounds on parameters during application of the results. Indeed, in realistic situations while operating with parameters having finite values, there is always a problem in justifying the validity of the approximation and determining the accuracy of the solution. What is the actual difference between the exact solution and the approximation which has been used? What are the upper limits of the parameters which can be used and still retain a specified level of accuracy in the solution? For the case of Rayleigh scattering of elastic waves, it appears that the limits of the approximation have not yet been quantified. An additional problem occurs when more than one assumption is involved in that they may be contradictory. This is a possibility for the case of Rayleigh scattering ($\omega \rightarrow 0$) in the far field ($r \rightarrow \infty$), where the parameter $(\omega r)/(V_p)$ is assumed to be large. The intention of this chapter is to investigate the accuracy of several asymptotic solutions and quantify the limits under which these approximations are applicable. The study presents the error for the application of the asymptotic solutions as a

function of various parameters and estimates under which conditions a given approximation provides an acceptable solution to the scattering problem.

Recently, Korneev and Johnson (1993a, 1993b) derived a solution for the scattering of an elastic P wave by a spherical inclusion of arbitrary contrast and developed asymptotic solutions for this problem. Their low frequency Rayleigh approximation which is valid for an arbitrary distance between the observation point and the inhomogeneity is being investigated and compared to the solutions based on near field and far field approximations. The validity range for these limited approximations is presented with respect to the distance of observation and the relative contributions of the near and far field terms to the complete Rayleigh approximation is discussed. It should be noted here that, while these approximations were derived from the exact solution for a sphere, they depend only upon the volume of the scatterer and not upon its shape, and thus should be valid for the general class of inclusions with approximately equal dimensions.

The Rayleigh approximation can be used to model the scattering process of low frequency waves by an inhomogeneity. A common goal in seismology is to determine the elastic properties of this inhomogeneity by inversion techniques. However, since the dependence of the solution on the elastic parameters is nonlinear, the inversion of the data often is preceded by a linearization of the problem. For this purpose, a linearized solution in terms of the elastic parameters is derived and the error as a function of their perturbations assessed. Furthermore, the improvement of the approximation by accounting for higher order terms is investigated. The determination of the relative error is based on the parameter values of the inhomogeneity and the background medium. Often these values are unavailable, particularly in the planing stage of an experiment when anticipated errors play an important role. Therefore, an equation for the approximate error due to linearization of the problem is developed which is based entirely on the estimated parameter perturbations from the background values. Finally, the upper limit for the Rayleigh approximation ($kR \ll 1$) as a function of parameter perturbation is investigated.

2.2 Rayleigh Approximation for an Elastic Sphere of Arbitrary Contrast

A derivation of the exact scattering solution for a homogeneous elastic sphere was given by Korneev and Johnson (1993a, 1993b). In their second paper they derive a low frequency approximation for a spherical inclusion. However, because of its low frequency character, this approximation simultaneously provides a solution for a wide range of arbitrary shaped 3-dimensional structures. For reasons of clarity, the exact solution is restated followed by their derivation of the low frequency approximation.

The investigated scattering problem consists of an elastic inclusion defined by the parameters λ_1, μ_1 and ρ_1 (in the following, the index $\nu = 1$ denotes the medium of the inclusion) embedded in a homogeneous medium with constant parameters λ_2, μ_2 and ρ_2 (in the following, the index $\nu = 2$ refers to the background medium). The geometry for this situation is shown in Figure 2.1. A joint Cartesian (x, y, z) and spherical (r, θ, ϕ) coordinate system with its origin at the center of the inclusion is considered.

An incident plane P wave of the form

$$\widetilde{\mathbf{U}}_0 = e^{i\omega(t-z/V_{P_2})}\hat{\mathbf{z}} = \mathbf{U}_0 e^{i\omega t} \tag{2.1}$$

which is traveling in the background medium in a positive direction along the z-axis is considered in the following investigations. $\mathbf{U}_0$ denotes the Fourier transform of the incident wave. However, at the end of this section, a factor that accounts for an incident spherical wave generated by a point pressure source will be provided.

In the frequency domain, the total solution to the scattering problem can be written as a sum of the incident and the scattered fields

$$\widetilde{\mathbf{U}} = \mathbf{U} e^{i\omega t} = (\mathbf{U}_0 + \mathbf{U}_p + \mathbf{U}_s) e^{i\omega t} \tag{2.2}$$

where $\mathbf{U}_p$ and $\mathbf{U}_s$ denote the scattered P and S waves, respectively.

For the case of a plane P wave impinging upon a sphere of radius R, the total scattered field can be represented as

$$\begin{aligned}
\mathbf{U}_{sc} &= \mathbf{U}_P + \mathbf{U}_S \\
&= \sum_{l\geq 0} e^{-i\pi/2\,(l+1)}\,(2l+1)\Bigg\{a_l\Bigg[\left((l+1)\frac{h_l(k_p r)}{k_p r} - h_{l-1}(k_p r)\right) P_l(cos\theta)\hat{r} \\
&- \frac{h_l(k_p r)}{k_p r}\frac{\partial P_l(cos\theta)}{\partial\theta}\hat{\theta}\Bigg] + b_l\Bigg[l(l+1)\frac{h_l(k_s r)}{k_s r}\,P_l(cos\theta)\hat{r} \\
&+ \left(h_{l-1}(k_s r) - \frac{h_l(k_s r)}{k_s r}\right)\frac{\partial P_l(cos\theta)}{\partial\theta}\hat{\theta}\Bigg]\Bigg\}, \qquad (2.3)
\end{aligned}$$

where $h_k(x)$ are spherical Hankel functions of the second kind and P_l are the Legendre functions. The coefficients a_l and b_l depend upon the properties of the sphere as well as the background medium. They also depend on the wavenumber of the scattered fields. For a detailed discussion of the derivation refer to Korneev and Johnson (1993a).

For the development of the low frequency approximation, only those terms of the exact solution are used that are of lowest degree in frequency. These terms (ω^3) are of third order and appear only in the first three coefficients ($l = 0, 1, 2$) of the exact solution.

$$\begin{aligned}
a_0 &= i\frac{\xi^3}{6}\frac{\frac{3}{2}(\lambda_1-\lambda_2)+\mu_1-\mu_2}{\frac{1}{2}(\frac{3}{2}\lambda_1+\mu_1)+\mu_2} \\
a_1 &= -i\frac{\xi^3}{9}\left(\frac{\rho_1}{\rho_2}-1\right), \qquad b_1 = i\frac{\eta^3}{9}\left(\frac{\rho_1}{\rho_2}-1\right) \\
a_2 &= i\xi^3\frac{4}{45}\left(\frac{\mu_1}{\mu_2}-1\right)\frac{\gamma^2}{D}, \quad b_2 = -i\eta^3\frac{2}{45}\left(\frac{\mu_1}{\mu_2}\right)\frac{\gamma}{D} \qquad (2.4)
\end{aligned}$$

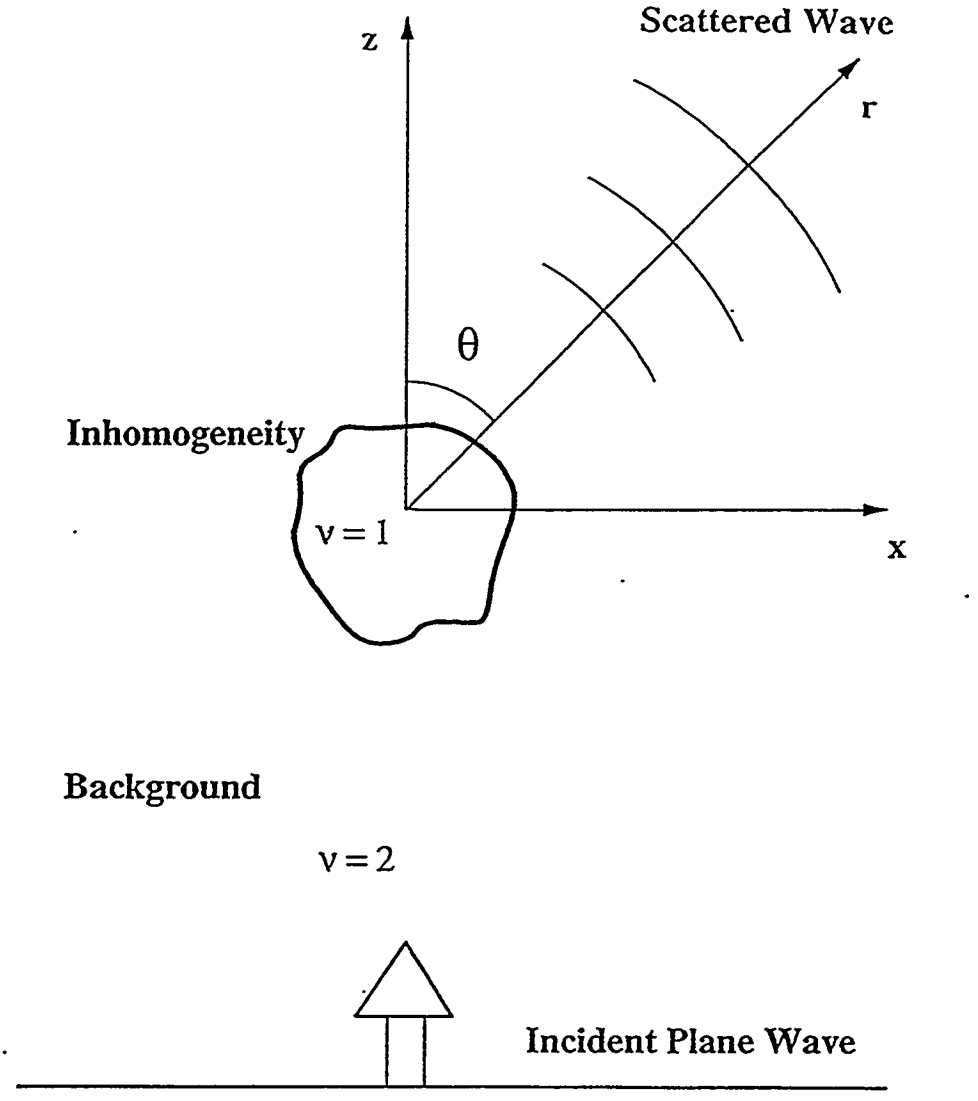

Figure 2.1: Geometry of the problem. The properties of the inhomogeneity and the background are denoted by $\nu = 1$ and $\nu = 2$, respectively. A plane wave is incident in the positive z direction, while the oberservation of the scattered wave is a function of $\hat{r}$ and $\hat{\theta}$.

with

$$V_{p_\nu} = \sqrt{\frac{\lambda_\nu + 2\mu_\nu}{\rho_\nu}}\,, \quad V_{s_\nu} = \sqrt{\frac{\mu_\nu}{\rho_\nu}}\,, \quad k_p = \frac{\omega}{V_{p_2}}\,, \quad k_s = \frac{\omega}{V_{s_2}}$$

$$\xi = k_p R\,, \quad \eta = k_s R\,, \quad \gamma = \frac{V_{s_2}}{V_{p_2}}$$

$$D = 1 + \frac{2}{15}\left(\frac{\mu_1}{\mu_2} - 1\right)(3 + 2\gamma^2). \tag{2.5}$$

Thus, a low frequency approximation with no restrictions upon the elastic parameters is obtained as:

$$\mathbf{U}_{sc} = \mathbf{U}_p + \mathbf{U}_s$$

with

$$\begin{aligned}
\mathbf{U}_p &= (\mathbf{U}_p)_r \hat{\boldsymbol{r}} + (\mathbf{U}_p)_\theta \hat{\boldsymbol{\theta}} \\
&= A\Bigg\{\Bigg[-\frac{1}{2}\frac{\frac{3}{2}(\lambda_1 - \lambda_2) + \mu_1 - \mu_2}{\frac{1}{2}(\frac{3}{2}\lambda_1 + \mu_1) + \mu_2} W^p_{0r}(Z_p) + \left(\frac{\rho_1}{\rho_2} - 1\right) W^p_{1r}(Z_p)\cos\theta \\
&+ \frac{2}{3}\left(\frac{\mu_1}{\mu_2} - 1\right)\frac{\gamma^2}{D} W^p_{2r}(Z_p)(1 - 3\cos^2\theta)\Bigg]\hat{\boldsymbol{r}} \\
&- \left[-\left(\frac{\rho_1}{\rho_2} - 1\right) W^p_{1\theta}(Z_p)\sin\theta + 2\left(\frac{\mu_1}{\mu_2} - 1\right)\frac{\gamma^2}{D} W^p_{2\theta}(Z_p)\sin 2\theta\right]\hat{\boldsymbol{\theta}}\Bigg\}
\end{aligned} \tag{2.6}$$

$$\mathbf{U}_s = (\mathbf{U}_s)_r \hat{\boldsymbol{r}} + (\mathbf{U}_s)_\theta \hat{\boldsymbol{\theta}}$$

$$= B\left\{\left[2\left(\frac{\rho_1}{\rho_2}-1\right)W^s_{1r}(Z_s)cos\theta + 2\left(\frac{\mu_1}{\mu_2}-1\right)\frac{\gamma^2}{D}W^s_{2r}(Z_s)(3cos^2\theta-1)\right]\hat{r}\right.$$

$$\left. + \left[-\left(\frac{\rho_1}{\rho_2}-1\right)W^s_{1\theta}(Z_s)sin\theta + \left(\frac{\mu_1}{\mu_2}-1\right)\frac{\gamma}{D}W^s_{2\theta}(Z_s)sin2\theta\right]\hat{\theta}\right\} \qquad (2.7)$$

The new functions are defined as follows

$$A = k_p^2\frac{V}{4\pi}\frac{e^{-ik_pr}}{r}\,, \quad B = k_s^2\frac{V}{4\pi}\frac{e^{-ik_sr}}{r} \qquad (2.8)$$

where V is the volume of the inclusion, and

$$W^p_{0r}(Z_p) = 1-\frac{i}{Z_p}$$

$$W^p_{1r}(Z_p) = 1-2\frac{1+iZ_p}{Z_p^2}\,, \quad W^p_{2r}(Z_p) = 1+\frac{9i-4iZ_p^2-9Z_p}{Z_p^3}$$

$$W^s_{1\theta}(Z_s) = 1-\frac{1+iZ_s}{Z_s^2}\,, \quad W^s_{2\theta}(Z_s) = 1+3\frac{2i-iZ_s^2-2Z_s}{Z_s^3}$$

$$W^p_{1\theta}(Z_p) = \frac{1+iZ_p}{Z_p^2}\,, \quad W^p_{2\theta}(Z_p) = \frac{3i-iZ_p^2-3Z_p}{Z_p^3}$$

$$W^s_{1r}(Z_s) = \frac{1+iZ_s}{Z_s^2}\,, \quad W^s_{2r}(Z_s) = \frac{3i-iZ_s^2-3Z_s}{Z_s^3} \qquad (2.9)$$

with

$$Z_p = k_pr = \frac{\omega r}{V_{p2}}\,, \quad Z_s = k_sr = \frac{\omega r}{V_{s2}}. \qquad (2.10)$$

The above approximation has used the lowest degree in frequency only, and is

based on the assumption that

$$k_{max}R = \frac{\omega R}{V_{min}} \ll 1, \tag{2.11}$$

where V_{min} denotes the minimum velocity and k_{max} represents the corresponding wavenumber. This result, generally known as the Rayleigh approximation, does not depend upon the shape of the inclusion but only upon its volume.

The W functions in equation (2.9) contain the distance dependence of the observation point from the center of the sphere and are valid for all values of $r \geq R$. Thus, the expression in equations (2.6) and (2.7) is a complete solution containing near and far field contributions. From this solution it is evident that the P wave of the scattered field contains a contribution in the $\hat{\theta}$-direction, while the S wave contains a factor in the $\hat{r}$-direction. Thus, the P and S waves are not decoupled and their polarization is complicated in the near field. However, as the distance of observation increases, the relative contributions of the W functions change in such a way that the solution takes on the form of the far field approximation.

To obtain the far field approximation, we have to satisfy the following conditions for the W functions in their limits:

$$|W^p_{0r}(Z_p)| \approx 1, |W^p_{1r}(Z_p)| \approx 1, |W^p_{2r}(Z_p)| \approx 1, |W^s_{1\theta}(Z_s)| \approx 1, |W^s_{2\theta}(Z_s)| \approx 1 \tag{2.12}$$

$$|W^p_{1\theta}(Z_p)| \approx 0, |W^p_{2\theta}(Z_p)| \approx 0, |W^s_{1r}(Z_s)| \approx 0, |W^s_{2r}(Z_s)| \approx 0. \tag{2.13}$$

In this limit, the scattered field can be divided into an $\hat{r}$- and a $\hat{\theta}$-component, both revealing a $1/r$ dependence for scattered waves in the far field:

$$\mathbf{U}_p = k_p^2 \frac{V}{4\pi} \frac{e^{-ik_p r}}{r} \left\{ -\frac{1}{2} \frac{\frac{3}{2}(\lambda_1 - \lambda_2) + \mu_1 - \mu_2}{\frac{1}{2}(\frac{3}{2}\lambda_1 + \mu_1) + \mu_2} + \left(\frac{\rho_1}{\rho_2} - 1 \right) cos\theta \right.$$

$$+ \frac{2}{3}\left(\frac{\mu_1}{\mu_2}-1\right)\frac{\gamma^2}{D}(1-3cos^2\theta)\Big\}\hat{r} \tag{2.14}$$

$$\mathbf{U}_s = k_s^2\frac{V}{4\pi}\frac{e^{-ik_sr}}{r}\Big\{-\left(\frac{\rho_1}{\rho_2}-1\right)sin\theta+\left(\frac{\mu_1}{\mu_2}-1\right)\frac{\gamma}{D}sin2\theta\Big\}\hat{\theta}. \tag{2.15}$$

The natural polarization in the $\hat{r}$- and $\hat{\theta}$-direction for the P and S wave, respectively, is evident.

The effect on the amplitude of the scattered field of the ratio between R and the wavelength λ_p of the incident P wave can easily be addressed by putting the solution (2.6) and (2.7) in the form

$$\mathbf{U}_p+\mathbf{U}_s=(k_pR)^3\,\mathbf{F}(Z_p,\theta)=(2\pi\frac{R}{\lambda_p})^3\,\mathbf{F}(Z_p,\theta) \tag{2.16}$$

(using $Z_p=\gamma Z_s$) where the function $\mathbf{F}(Z_p,\theta)$ also depends upon the parameter perturbations, but does not depend on the radius R of the inclusion. Thus, when $R\rightarrow\lambda_p$, the amplitudes increase, until the approximation reaches its limit at $(k_pR)_{lim}$ (Rayleigh limit).

In the near field where $Z_p\ll 1.0, Z_s\ll 1.0$ the P and S components of the scattered field may be combined to form an asymptotic solution depending on both $\hat{r}$ and $\hat{\theta}$, by expanding e^{-ik_pr} and e^{-ik_sr} in equation (2.8) and keeping only the lowest degree in Z_p.

$$\begin{aligned}\mathbf{U}_{sc} = \frac{V}{4\pi r^3}\Big\{&\Big[\frac{i}{2}\frac{\frac{3}{2}(\lambda_1-\lambda_2)+\mu_1-\mu_2}{\frac{1}{2}(\frac{3}{2}\lambda_1+\mu_1)+\mu_2}Z_p+\frac{1}{\gamma^2}\left(\frac{\rho_1}{\rho_2}-1\right)Z_p^2cos\theta\\ &+ i\left(1-\frac{\gamma^2}{3}\right)\left(\frac{\mu_1}{\mu_2}-1\right)\frac{Z_p}{D}(3cos^2\theta-1)\Big]\hat{r}\\ &-\Big[\frac{(1+\gamma^2)}{2\gamma^2}\left(\frac{\rho_1}{\rho_2}-1\right)Z_p^2sin\theta+i\gamma^2\left(\frac{\mu_1}{\mu_2}-1\right)\frac{Z_p}{D}sin2\theta\Big]\hat{\theta}\Big\}.\end{aligned} \tag{2.17}$$

With the definitions for Z_p and Z_s in equation (2.10), it becomes apparent that the amplitude for the near field approximation contains components which are proportional to $1/r$ and $1/r^2$. The sum of the $\hat{r}$ and $\hat{\theta}$-component indicates the complicated polarization, as the P and S-wave are not decoupled yet.

So far, the scattering problem involving considering an incident plane P wave with a source located at infinity has been treated. However, the problem can as well be addressed for the case of an inhomogeneity in the near or far field of a point pressure source exciting a spherical P wave

$$\mathrm{U}_0 = -\nabla \frac{e^{-ik_p r_0}}{r_0}, \tag{2.18}$$

where r_0 is the distance between the point source and the center of the inclusion.

The consideration of a spherical incident wave introduces additional functions for the distance dependence of the scattered field of the form

$$\begin{aligned} C_0 &= q \\ C_1 &= \frac{Z_{p0} - i}{Z_{p0}} q \\ C_2 &= \frac{Z_{p0}^2 - 3iZ_{p0} - 3}{Z_{p0}^2} q \end{aligned} \tag{2.19}$$

with

$$q = \frac{k_p}{r_0}, \quad Z_{p0} = k_p r_0 = \frac{\omega r_0}{V_{p2}}. \tag{2.20}$$

The C_l have to be multiplied onto those W_l functions in equation (2.9) that have the same degree in l to provide the correct distance dependent functions

for the case of a single point pressure source at an arbitrary distance from the inhomogeneity. However, in this chapter the problem of an incident plane P wave is treated only. This restriction permits all of the displacement fields to be represented in terms of unitless values for the purpose of simplicity in presenting numerical results.

2.3 Comparison Between Low Frequency Total Solution and the Approximations in the Near and Far Field

For the comparison of the various approximations listed above, the scattered amplitude for a given spherical inclusion with radius R along a profile of observation extending from $r = R$ (near field) to $r \gg R$ (far field) is computed. The profiles are determined for various scattering angles between $\theta = 0°$ and $\theta = 180°$ (symmetry exists along the $0° - 180°$ axis of incidence) to present a qualitative view of the angular dependence. The results are computed for an inhomogeneity with a 10% increase in V_p and V_s velocity as well as density with respect to the background. The structure (eq. 2.16) of the scattered field makes it possible to investigate the unitless function F independently of the radius R of the inclusion, thus producing results with more universal application. In Figure 2.2 (a,b,c) absolute values of the r-component of $\mathbf{F}(Z_p, \theta)$ are plotted as functions of $Z_p = k_p r$ of the incident wave for three different angles $\theta = 0°(a)$, $90°(b)$, $180^0(c)$. In order to compare results of a different geometry with these curves, the minimum value of the parameter $k_p R$ has to be determined for the new geometry, and subsequently the normalized amplitudes to the right of the new limit on the abscissa will be comparable after multiplication by the corresponding value of $(k_p R)^3$. This minimum should be equal to, or less than the Rayleigh limit $(k_p R)_{lim}$, which depends upon the parameter perturbations. A detailed discussion on the validity range of the Rayleigh limit

is presented in section 2.5.

For each value of θ in Figure 2.2 (a,b,c) three curves are shown, representing the $\hat{r}$-component of the total field (solid line, eqs. 2.6 and 2.7), the near field (dashed line, eq. 2.17), and the far field (dotted line, eqs. 2.14 and 2.15) of the Rayleigh approximation. The graphs are plotted using a logarithmic scale for both axis. Thus, the far field solution with a distance dependence of $1/r$ appears as a straight line with a slope of -1, whereas the near field solution revealing both a $1/r$ and $1/r^2$ dependence produces two constant slopes. In the very near field the $1/r^2$ term is dominant, creating a slope of -2, while for larger distances the dominance of the $1/r$ term is apparent by a change in slope to -1. The transition between these two slopes is defined by contributions from both factors. However, the application of the approximations at various distances of observation requires a careful investigation of their validity range. All curves are computed between $k_p r = 10^{-2}$ ($r = 1R$) and $k_p r = 10^3$ ($r = 10^5 R$), although only the total field is valid for the whole range, as found from comparison with the exact solution for the sphere. The near field solution is applicable in the vicinity of the inhomogeneity, whereas the far field yields correct values at a greater distance from the inhomogeneity only. This is supported by Figure 2.2a). The total field solution coincides very well with the near field solution for small values of $k_p r$, whereas the discrepancy becomes larger for greater distances of observation. Similarly, it differs from the far field solution in the near field, while asymptotically, the two solutions merge in the far field. The oscillatory nature of the total solution in the $\hat{r}$- and the $\hat{\theta}$-component is based on the near field contribution of the S wave ($\mathrm{k_s}$ vector in the $\hat{r}$-component) and P wave ($\mathrm{k_p}$ vector in the $\hat{\theta}$-component), respectively. The interference between both components is present in the near field only and decreases in the far field.

The most intriguing result is the large amplitude difference between the total and the far field solution of magnitude (≈ 300) for the very near field $k_p r = 10^{-2}$ ($r = R$). This difference decays continuously until good agreement is reached at a distance of approximately $k_p r \approx 4\pi$ ($r \approx 2\lambda$). Between $k_p r = 10^{-2}$ and $k_p r \approx 4\pi/10$ ($r \approx 0.2\lambda$), the near field provides a better approximation than

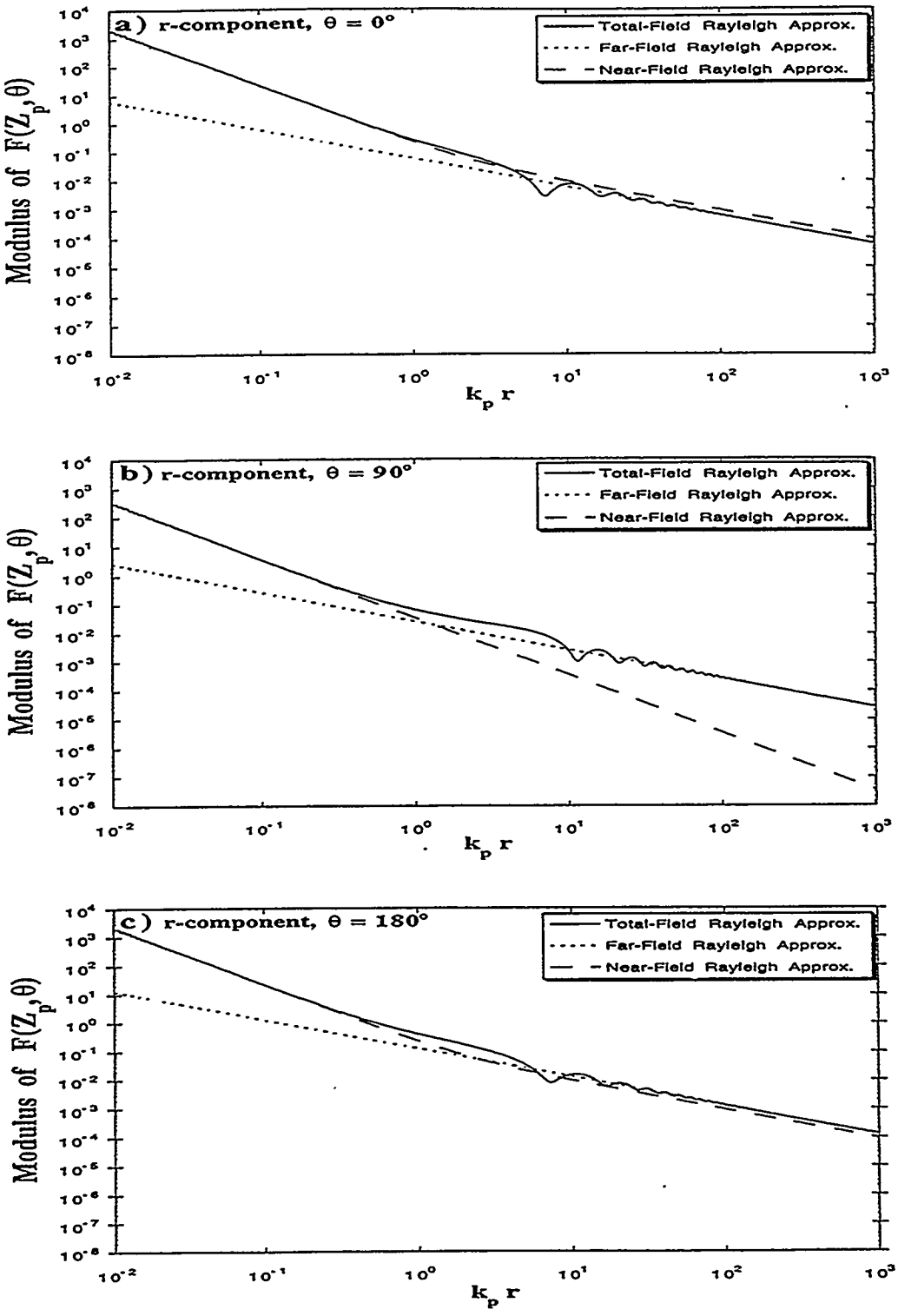

Figure 2.2: Normalized modulus of amplitude factor $\mathbf{F}(Z_p, \theta)$ (eq. 2.16). Radial component of the low-frequency scattered fields for a high velocity and high density inclusion of +10%.

the far field solution. In between these distances ($0.2\lambda < r < 2\lambda$), a range that is referred to as the mid field, both solutions present an alternating fit to the total field because of its oscillatory behavior. Figure 2.2a) presents pure forward scattering ($\theta = 0°$), while Figures 2.2b) and 2.2c) show the results for a scattering angle of $\theta = 90°$ and $\theta = 180°$ (backscattering), respectively. It is evident that the main features described above still apply in these cases, although the amplitude difference between total and far field for $r = R$ decrease by one order of magnitude for $\theta = 90°$, before it regains the initial value for $\theta = 180°$. For the scattering angle of $\theta = 90°$, a drop in amplitude of the near field solution below the values of the far field solution is noticeable yet without bearing as the solution is not valid in this range.

The $\hat{\theta}$-components of the same fields are presented in Figures 2.3a) - 2.3c). Because the amplitude of the $\hat{\theta}$-component is zero for $\theta = 0°$ and $\theta = 180°$, the results for $\theta = 45°$, $\theta = 90°$ and $\theta = 135°$ are shown. Again, the total field coincides well with the near and the far field solution in the near and far field range, respectively. However, it is evident that the amplitude difference in the near field decreases to a factor of 15 for $\theta = 45°$ and $\theta = 135°$, and shows no significant difference for $\theta = 90°$, while the amplitudes are slightly larger for the far field solution. The mid field region is characterized by a misfit for both near field and far field solutions, although the total field solution reveals less oscillations.

The oscillatory nature of the total field solution causes similar oscillations of the relative error between the total field and the far or near field solutions. Because of this it is useful to define the mean value of the error as the smooth trend through the residuals which minimizes the effect of the rapidly fluctuating values. For the relative error in the $\hat{r}$-component, a mean value of 15% at a distance of 2λ is found. However, the oscillations around this value can be as high as 35% and as low as 2%. At a distance of 10λ, for example, the mean error has decreased to 5% with variations between 8% and 2%. The values for the $\hat{\theta}$-component reveal a smaller error over the entire distance of observation. At 2λ, the mean value of the relative error is 2%, with fluctuations between 4%

and 0%, and this decreases gradually with increasing distance of observation.

The comparison between the total and far field solution indicates the advantage of near field components in the total field solution. The high amplitudes of the scattered waves in the near field suggest an improvement for the determination of the elastic properties, under the assumption that corrections for the incident field can be applied. Thus the deployment of recording instrumentation in the vicinity of inhomogeneities together with the observation of the incident field could improve the results for inverting scattered energy. In addition the limit for the validity of the far field solution indicates that for an observation distance less than 2λ, this solution produces wrong results, while it can be applied to distances greater than 2λ.

The presented results are computed for an inhomogeneity with a 10% increase in V_p and V_s velocities as well as in its density with respect to the background. Because the modulus of the amplitudes is computed in this study, investigations of a negative perturbation produce the same shape and relations of the amplitude curves for equal magnitude of perturbation. To determine the sign of the perturbation, the separate use of real and imaginary part is more appropriate. However, the investigation of scattering diagrams as a function of combinations of parameter perturbations is beyond the purpose of this work, and are treated by Sato (1984), Wu and Aki (1985), and Tarantola (1986).

2.4 Extension and Evaluation of the Rayleigh-Born Approximation

Thus far, scattering solutions for arbitrary contrast in the elastic parameters have been treated only. In equation (2.4) the coefficients are nonlinear in terms of the elastic parameters λ and μ. This can be problematic, if a solution for the inversion of the scattering problem in terms of the elastic parameters is sought. A common practice, therefore, is to solve the linearized inversion problem. This linearization is often referred to as the Born approximation. The

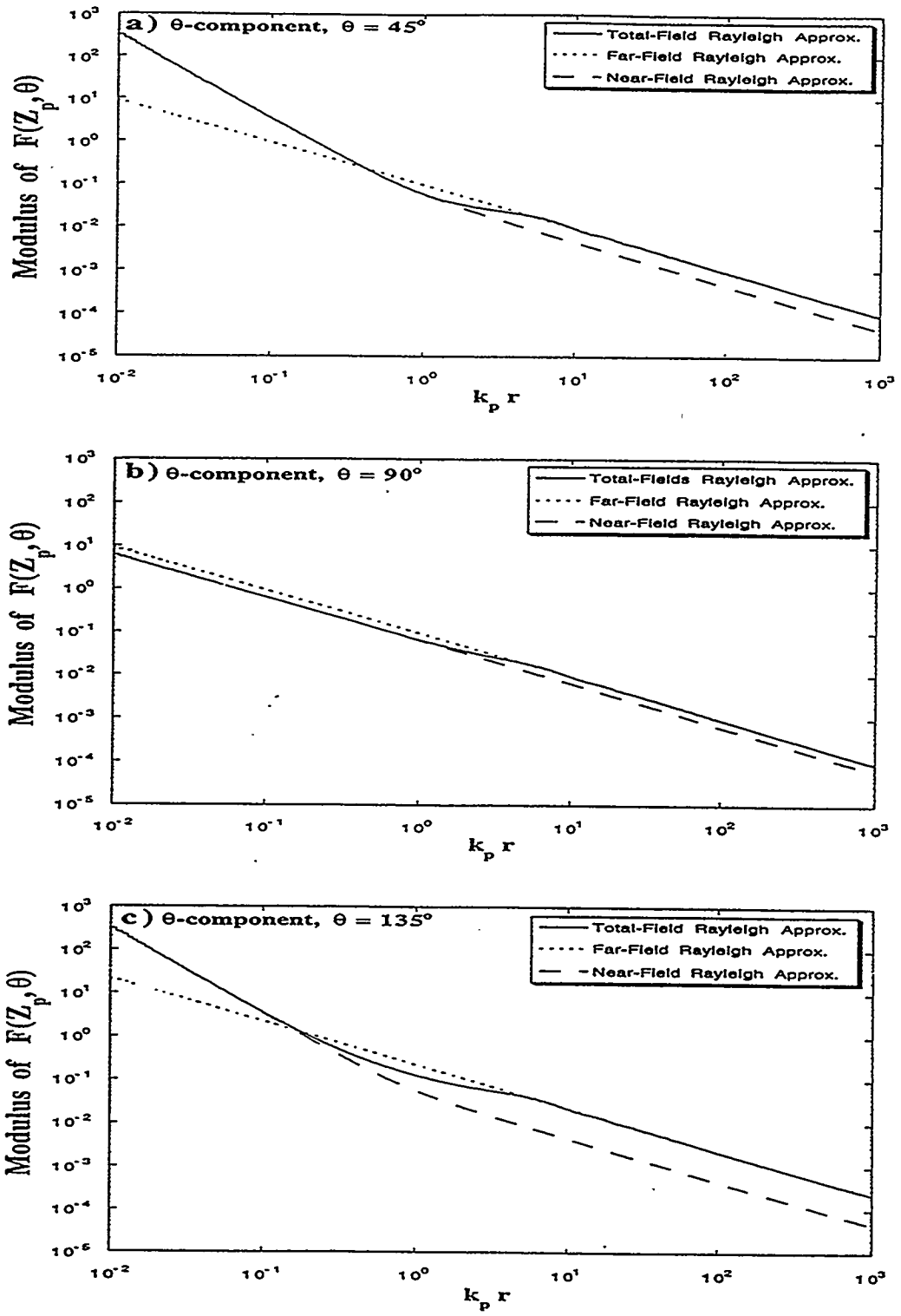

Figure 2.3: Normalized modulus of amplitude factor $\mathbf{F}(Z_p, \theta)$ (eq. 2.16). Azimuthal component of the low-frequency scattered fields for a high velocity and high density inclusion of +10%.

actual conditions for the validity of the Born approximation include the size of the inclusion, the perturbation of its elastic parameters with respect to the background, and the phase shift between different scattered phases (Hudson and Heritage, 1991). In the Rayleigh scattering regime, the wavelength is large compared to the scatterer size, and for the case of a weak inhomogeneity, the consideration of a possible phase shift can be neglected. Thus, for this case, the Born approximation is valid, and is often referred to as the Rayleigh-Born approximation. To linearize the problem, the coefficients are expressed in a converging binomial series expansion assuming the perturbations in the parameters are smaller than the background values. The approximate solution is found by keeping the linear term of the series expansion while disregarding higher orders. This step is valid only for small perturbations.

$$\frac{|\delta\lambda|}{\lambda_2} = \frac{|\lambda_1 - \lambda_2|}{\lambda_2} \ll 1, \quad \frac{|\delta\mu|}{\mu_2} = \frac{|\mu_1 - \mu_2|}{\mu_2} \ll 1, \quad \frac{|\delta\rho|}{\rho_2} = \frac{|\rho_1 - \rho_2|}{\rho_2} \ll 1. \qquad (2.21)$$

Expanding the coefficients in equation (2.4) in terms of the elastic parameters and keeping the first terms only yields a linearized solution to the scattering problem which has the form

$$\mathbf{U}_{sc}^{(1)} = \mathbf{U}_{p}^{(1)} + \mathbf{U}_{s}^{(1)}$$

with

$$\begin{aligned}
\mathbf{U}_{p}^{(1)} &= A\Bigg\{\Bigg[-\frac{1}{2}\frac{\frac{3}{2}\delta\lambda + \delta\mu}{\frac{1}{2}(\frac{3}{2}\lambda_1 + \mu_1) + \mu_2} W_{0r}^{p}(Z_p) + \frac{\delta\rho}{\rho_2} W_{1r}^{p}(Z_p)cos\theta \\
&+ \frac{2}{3}\frac{\delta\mu}{\mu_2}\gamma^2 W_{2r}^{p}(Z_p)(1 - 3cos^2\theta)\Bigg]\hat{r} \\
&- \Bigg[-\frac{\delta\rho}{\rho_2} W_{1\theta}^{p}(Z_p)sin\theta + 2\frac{\delta\mu}{\mu_2}\gamma^2 W_{2\theta}^{p}(Z_p)sin2\theta\Bigg]\hat{\theta}\Bigg\} \qquad (2.22)
\end{aligned}$$

$$\mathbf{U}_s^{(1)} = B\left\{\left[2\frac{\delta\rho}{\rho_2}W_{1r}^s cos\theta + 2\frac{\delta\mu}{\mu_2}\gamma^2 W_{2r}^s(Z_s)(3cos^2\theta - 1)\right]\hat{r}\right.$$

$$\left. + \left[-\frac{\delta\rho}{\rho_2}W_{1\theta}^s(Z_s)sin\theta + \frac{\delta\mu}{\mu_2}\gamma W_{2\theta}^s(Z_s)sin2\theta\right]\hat{\theta}\right\}. \qquad (2.23)$$

In order to evaluate the error made by applying the linearized solution, both the linear and the quadratic term of the expansion for the coefficients in equation (2.4) are used and a more exact approximation to the nonlinear solution, referred to as the quadratic approximation, is derived. This gives

$$\mathbf{U}_{sc}^{(2)} = \mathbf{U}_p^{(2)} + \mathbf{U}_s^{(2)}$$

where

$$\mathbf{U}_p^{(2)} = A\left\{\left[-\frac{1}{2}\left(\frac{\frac{3}{2}\delta\lambda + \delta\mu}{\frac{1}{2}\left(\frac{3}{2}\lambda_2 + \mu_2\right) + \mu_2} - \frac{1}{2}\frac{\left(\frac{3}{2}\delta\lambda + \delta\mu\right)^2}{\left(\frac{1}{2}\left(\frac{3}{2}\lambda_2 + \mu_2\right) + \mu_2\right)^2}\right)W_{0r}^p(Z_p)\right.\right.$$

$$+ \frac{\delta\rho}{\rho_2}W_{1r}^p(Z_p)cos\theta$$

$$\left. + \frac{2}{3}\left(\frac{\delta\mu}{\mu_2} - \frac{2}{15}\left(\frac{\delta\mu}{\mu_2}\right)^2(3 + 2\gamma^2)\right)\gamma^2 W_{2r}^p(Z_p)(1 - 3cos^2\theta)\right]\hat{r}$$

$$- \left[-\frac{\delta\rho}{\rho_2}W_{1\theta}^p(Z_p)sin\theta\right.$$

$$\left.\left. + 2\left(\frac{\delta\mu}{\mu_2} - \frac{2}{15}\left(\frac{\delta\mu}{\mu_2}\right)^2(3 + 2\gamma^2)\right)\gamma^2 W_{2\theta}^p(Z_p)sin2\theta\right]\hat{\theta}\right\} \qquad (2.24)$$

$$\mathbf{U}_s^{(2)} = B\left\{\left[2\frac{\delta\rho}{\rho_2}W_{1r}^s cos\theta\right.\right.$$

$$+ \quad 2\left(\frac{\delta\mu}{\mu_2} - \frac{2}{15}\left(\frac{\delta\mu}{\mu_2}\right)^2(3+2\gamma^2)\right)\gamma W^s_{2r}(Z_s)(3cos^2\theta - 1)\Big]\hat{r}$$

$$+ \quad \Big[-\frac{\delta\rho}{\rho_2}W^s_{1\theta}(Z_s)sin\theta$$

$$+ \quad \left(\frac{\delta\mu}{\mu_2} - \frac{2}{15}\left(\frac{\delta\mu}{\mu_2}\right)^2(3+2\gamma^2)\right)\gamma W^s_{2\theta}(Z_s)sin2\theta\Big]\hat{\theta}\Big\}. \tag{2.25}$$

Equations (2.6), (2.7), (2.22), (2.23), (2.24) and (2.25) are the basis for the evaluation of the error in approximating the nonlinear solution. The evaluations are undertaken in the far field of the inhomogeneity, allowing the application of the commonly used far field approximation. First, the error is evaluated in terms of the scattering angle to investigate the possible effects of the scattering direction. Therefore, the amplitude of the scattered field are determined for all angles between 0^o and 360^o using the three equations mentioned above. The result is given in Figure 2.4. For both components, the amplitude values of the linear approximation exceeds the nonlinear solution, while the quadratic approximation underestimates it. This is caused by the alternating sign in the series expansion with increasing order.

A problem for the estimation of the relative error between the approximations and the nonlinear solution for every scattering angle arises from the vanishing amplitude values at $\theta \approx 0^o, 75^o, 180^o, 285^o, 360^o$. These singularities produce unphysically high values for the relative error. Therefore, the error in the $\hat{r}$- and $\hat{\theta}$-component will be related to the mean square amplitude

$$\overline{(U_{sc})^2_c} = \frac{1}{2}\int_0^\pi |U_{sc}(\theta)|^2_c \, sin\theta d\theta. \tag{2.26}$$

Here, $c = r, \theta$ denotes the components of the scattered wave. Hence the relative error becomes

$$\Delta e_c^{(\varepsilon)} = \left(\frac{(U_{sc}^{(\varepsilon)}(\theta) - U_{sc}(\theta))_c^2}{\overline{(U_{sc})_c^2}} \right)^{1/2}, \tag{2.27}$$

where $\varepsilon = 1, 2$ represents the linear and quadratic Rayleigh-Born approximation, while $U_{sc}^{\varepsilon}(\theta)$ and $U_{sc}(\theta)$ denote the scattered field of equations (2.22), (2.23), (2.24), (2.25), (2.6) and (2.7), respectively. Thus, the error is normalized for each component by the average scattered amplitude of the same component. Figure 2.5 reveals the results. For the $\hat{r}$-component, a relatively smooth distribution of the error can be seen. The scattering problem is symmetric along the 0°-180° axis. One evident feature is the decrease of the error between the forward and the 90° scattering direction by a factor of ~ 3. Further, it can be seen that for this particular example of a velocity and density perturbation of +10%, the introduction of the quadratic term in the series expansion reduces the error compared to the linear approximation by a factor of more than 5. The same improvement is found for the $\hat{\theta}$-component. Distinct lobes at angles of approximately 45° to both sides of the axis of wave incidence are visible. For both components no particular difference between forward and backscattering is evident. This representation of the error reveals the strong dependence on the scattering angle and provides some insight in the improvement to be gained by taking into account the quadratic term in the series expansion.

Next, in order to estimate the error as a function of perturbation in the elastic parameters, the difference between the Rayleigh-Born and the nonlinear approximation is integrated over all scattering angles θ

$$\overline{(\mathrm{U}_{sc}^{(\varepsilon)} - \mathrm{U}_{sc})^2} = \frac{1}{2} \int_0^{\pi} \left| U_{sc}^{(\varepsilon)}(\theta) - U_{sc}(\theta) \right|^2 sin\theta d\theta, \tag{2.28}$$

and related to the nonlinear approximate solution integrated over all scattering angles θ

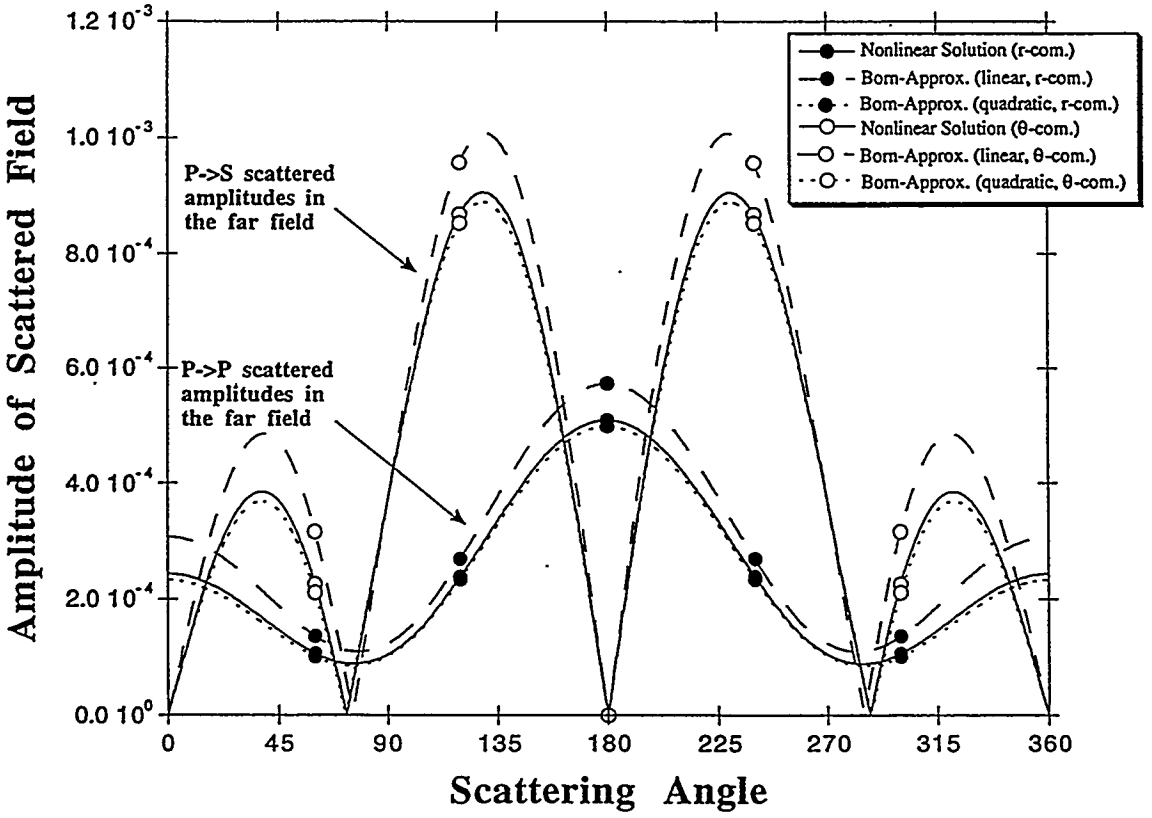

Figure 2.4: Amplitudes of scattered fields as a function of scattering angle.

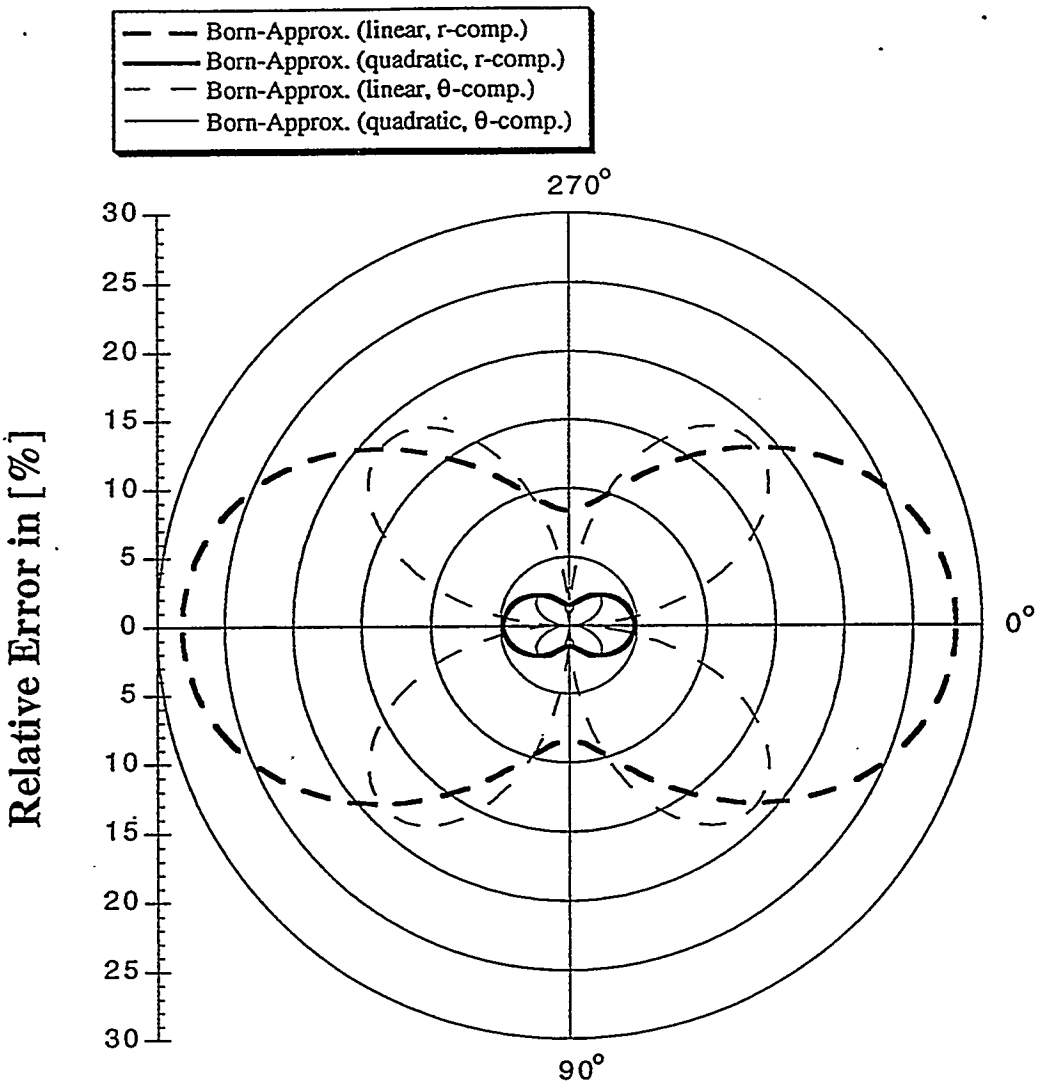

Figure 2.5: Relative error of the radial and azimuthal component of the linear and quadratic Rayleigh-Born approximation.

$$\overline{U_{sc}^2} = \frac{1}{2}\int_0^{\pi} |U_{sc}|_c^2 \, sin\theta d\theta. \tag{2.29}$$

This allows to compare the total average scattered amplitude for the nonlinear and the approximate solution and to investigate it as a function of parameter perturbation. Hence the error becomes

$$\Delta e^{(\epsilon)} = \left(\frac{(U_{sc}^{(\epsilon)} - U_{sc})^2}{\overline{U_{sc}^2}} \right)^{1/2}, \tag{2.30}$$

where the notation is equivalent to equations (2.26) and (2.27). The result is shown in Figure 2.6 for positive and negative parameter perturbations in λ, μ and ρ. The quadratic approximation reveals a smaller error compared to the linear approximation over the entire range for both cases of a positive and negative perturbation. However, the best improvement is achieved for perturbations less than 20%. While -100% constitutes a lower limit for the error, it was found that above a perturbation of $+200\%$, the error for the linear approximation becomes less than for the quadratic approximation (although physically this is an acceptable statement, mathematically the extension beyond $+100\%$ is incorrect, since the assumption for the series expansion of the elastic parameters (eq. 2.21) was that the absolute value of the relative parameter perturbation remains smaller than one).

It should be noted that the solution in equations (2.6) and (2.7) depends linearly on the perturbation in density. Therefore, the scattering problem for an inhomogeneity with a change in density only, can be exactly described by the linear approximation in equations (2.22) and (2.23).

The difference in the errors between the linear and quadratic Rayleigh-Born approximation can be used in the inversion of a linearized problem. After the first iteration of the inversion, the quadratic Rayleigh-Born approximation is computed and the difference from the linear approximation can be applied to

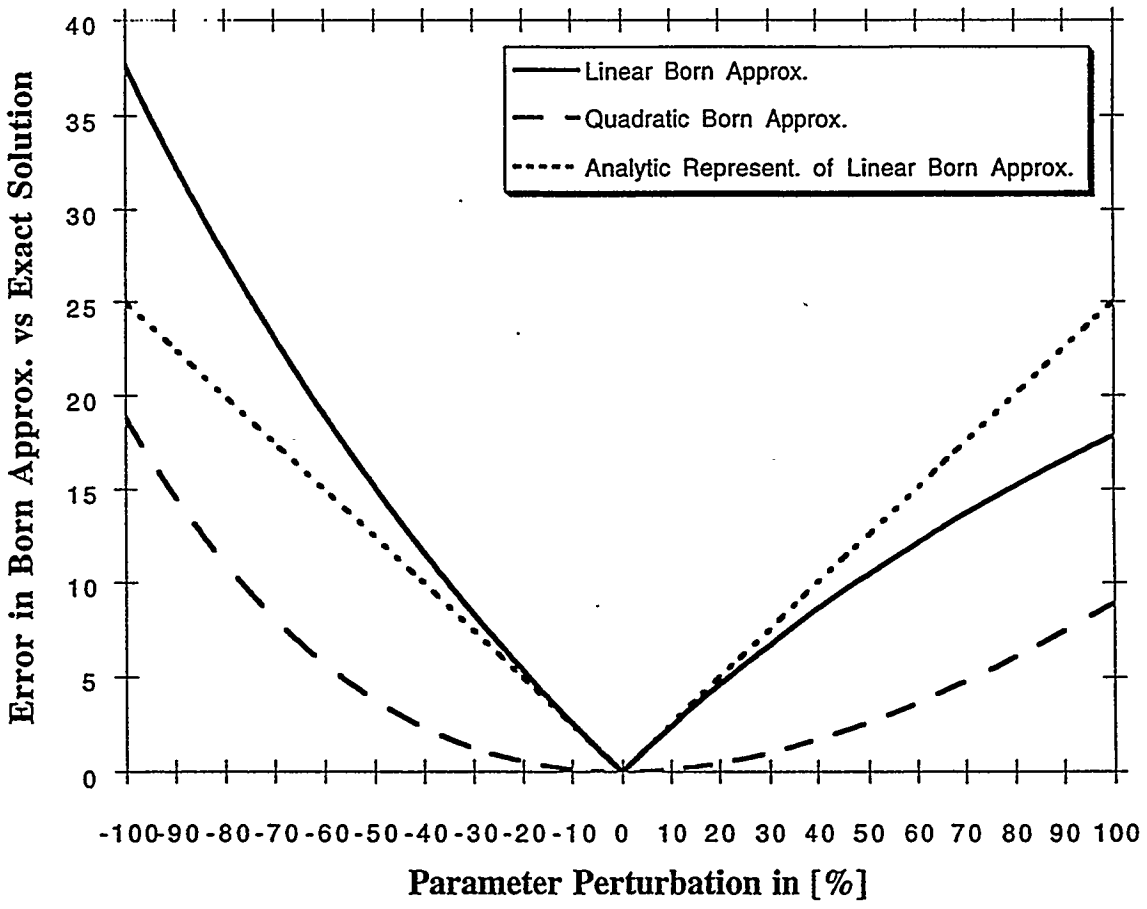

Figure 2.6: Relative average error of the linear and quadratic Rayleigh-Born approximation as a function of parameter perturbation.

adjust the first preliminary result. The corrected result will be the input for the second iteration. This scheme, should ensure a faster converging solution to the problem of inverting for the parameters of a scatterer.

In the following, a quantitative estimation of the relative error of the linear approximation based purely on the relative perturbations in the elastic parameters from the background values is presented. This provides an important estimate for the error due to linearization of an experiment where no absolute values are available, except for assumed perturbations of the inhomogeneity from the background. The error is based on the equation (2.30)

$$\Delta e^{(1)} = \left(\frac{(U_{sc}^{(1)} - U_{sc})^2}{\overline{U_{sc}^2}} \right)^{1/2} \approx \left(\frac{(U_{sc}^{(1)} - U_{sc}^{(2)})^2}{\overline{U_{sc}^{(1)2}}} \right)^{1/2} . \tag{2.31}$$

This has the advantage that only perturbation terms of the elastic parameters remain in the resulting equation. Assuming equal perturbation for

$$\frac{\delta\lambda}{\lambda_2} = C, \quad \frac{\delta\mu}{\mu_2} = C, \quad \frac{\delta\rho}{\rho_2} = nC \quad \text{and} \quad \gamma = \frac{V_s}{V_p} = \sqrt{\frac{1}{3}}, \tag{2.32}$$

it is found that

$$\Delta e^{(1)} = \frac{|C|}{2\sqrt{3n^2+1}}. \tag{2.33}$$

Thus for the case of similar perturbations in the density and the elastic parameters ($n = 1$) this yields $C/4$, whereas no density contrast ($n = 0$) produces an error of $C/2$. The dependence of this error on the perturbation in elastic parameters is shown in Figure 2.6 (dashed line). A good agreement between the linear approximation and the estimated error is found up to a parameter perturbation of 20%. The derived equation provides a means to estimate the

minimum error in the total averaged scattered amplitude due to the linearization of the problem. It should be mentioned that for the case of an inversion, additional errors associate with ill conditioning of the experiment and poor signal to noise ratios, for example, will increase the total error for the estimated parameters of the inclusion.

2.5 Investigation and Evaluation of the Rayleigh Limit

The Rayleigh approximation generally is based on the assumption that the parameter k_pR is small compared to 1,

$$k_pR = \frac{\omega R}{V_p} \ll 1, \tag{2.34}$$

although the actual magnitude of the limit is not known. The value of k_pR depends not only on the wavelength, the velocity of the background, and the dimensions of the scatterer, but also on the perturbations in the elastic parameters from the background values. Therefore, the Rayleigh limit of k_pR is investigated as a function of perturbation in the elastic parameters. For a given perturbation and fixed value of k_pR, the average square amplitude is computed over all scattering angles, for the exact solution for the sphere (eq. 2.3) and for the Rayleigh approximation in the far field (eqs. 2.14 and 2.15). The two solutions tend to deviate with increasing k_pR for a fixed perturbation value. The Rayleigh limit is determined from the value of k_pR that is reached for a predefined maximum deviation of these two solutions. The result is shown in Figure 2.7. The maximum deviation between the two solutions is set to 5%, 10% and 20%, while the parameter perturbation was chosen to vary, when possible, between -100% and $+300\%$. Three different relations between the perturbations of elastic moduli and density were selected. In addition, the velocity and

density ratios are indicated to demonstrate the effect of the parameter perturbations. In the presented examples, the sign and increase in perturbation are kept equal for λ and μ, while the associated change in ρ varies in sign and magnitude. Figure 2.7a) denotes the situation of a 50% reduced density increase in relation to the other parameters. The curves for the Rayleigh limit show a parallel trend for the different errors, with a smooth flat level between -75% and $+100\%$. For higher perturbations a slow decrease in the Rayleigh limit is observable. However, towards -100% the limit drops steeply, indicating a small value for the Rayleigh limit of a very low-velocity inclusion. This result has a natural explanation in the fact that k_pR inside the inclusion becomes large and violates the Rayleigh limit condition. Changing the relation between the parameter perturbations will affect the shape of the curves as seen in the next examples. In Figure 2.7b), the density is kept at a constant level which produced a maximum in the Rayleigh limit for perturbations between -25% and -50%. This maximum is caused by the mutual influence of an underestimation of the behavior of the Rayleigh solution for low-velocity obstacles in the Mie diffraction region ($k_pR \approx 1$) and a general overestimation of the trend of the solution at high frequencies. At some point these two processes compensate each other. Numerical examples illustrating this phenomena and a discussion may be found in Korneev and Johnson (1993b). For a third relation between the elastic parameters (Fig. 2.7c)), the maximum is reached for a lower negative perturbation with a different amplitude. In both cases the trend of the curves for positive perturbations remains the same, indicating a continuously increasing deviation between the Rayleigh approximation and the exact solution.

The results clearly suggest that the Rayleigh limit has a more flexible interpretation than indicated by condition (2.34). Depending on the acceptable error between the Rayleigh approximation and the exact solution, values for the Rayleigh limit vary between 0.3 and 0.8 for a positive increase in parameter perturbation, and the limits reaches values of up to 0.9 for negative perturbations. The constant shift between the graphs for the three errors over the entire range of perturbation indicates a relation between the error and the Rayleigh

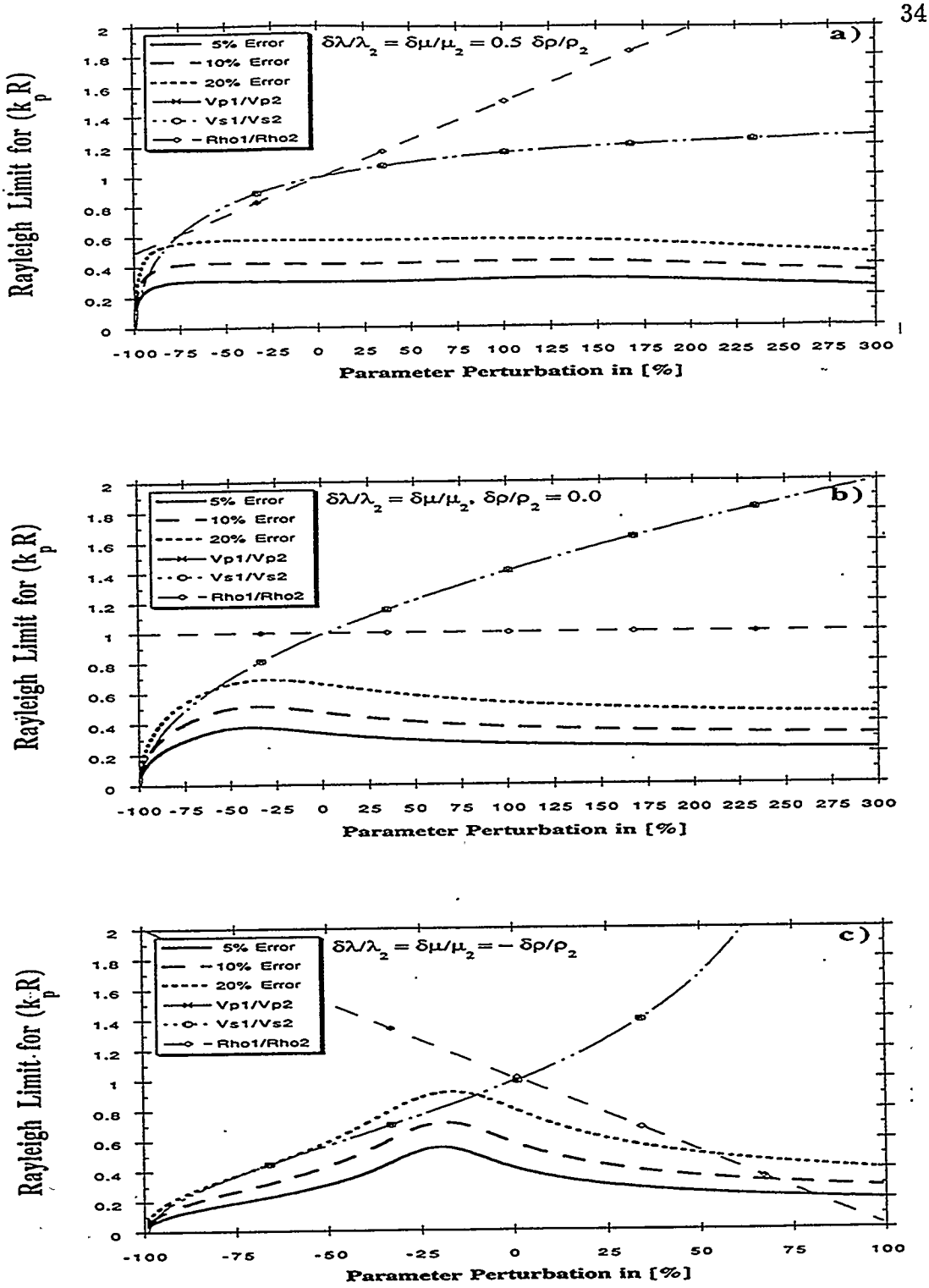

Figure 2.7: Rayleigh limit for the parameter k_pR as a function of parameter perturbation. The three curves correspond to three investigated error limits of 5%, 10% and 20%. Also plotted are the velocity and density ratios associated with the chosen relation between the elastic parameters.

limit $(k_pR)_{lim}$ which can be found from the equation

$$\Delta e = d\,(k_pR)^2_{lim}, \tag{2.35}$$

where Δe is the allowed error, and d a constant, defined by the perturbation in the elastic parameters from the background. In order to approximate the magnitude of d, the exact solution for the sphere (eq. 2.3) is chosen, and a low frequency approximation is derived based on frequency terms up to fifth order (ω^5), thus using the first four coefficients ($l = 0, 1, 2, 3$) of the exact solution. By comparing the parameter k_pR of this improved approximation and the Rayleigh approximation based on third order terms (eqs. 2.6 and 2.7), we are able to evaluate d. The notation and assumptions from equation (2.32) yield in the vicinity of zero perturbation

$$d \approx 0.4 \left(\frac{7n^2 + 5n + 2}{6.4n^2 + 1.6} \right)^{1/2}. \tag{2.36}$$

Thus, for the low frequency Rayleigh approximation (eqs. 2.6 and 2.7), equation (2.35) provides a means to estimate the error of the Rayleigh limit with a minimum knowledge of the parameters involved.

2.6 Conclusions

The intention of this chapter was to investigate the accuracy of several asymptotic solutions to the problem of low frequency elastic wave scattering and to provide means to evaluate scattering experiments in their planing stage. The results were kept in universal format, allowing for a convenient application to various scattering problems in seismology, varying from local over crustal to mantle scale lengths.

A low frequency total field solution to the problem of elastic Rayleigh scattering was investigated and produced, within the Rayleigh limits, exact results over the entire distance range of observation. This solution was subsequently compared to pure near and far field solutions. The generally used far field solution cannot be applied to the case of an inhomogeneity situated within a distance less than two wavelengths from the point of observation. Within this distance, the near field terms dominate the amplitude of the scattered wave, and P and S waves cannot be separated. This case, dependent on the wavelength of the incident wave, may arise in cross hole experiments when the inhomogeneity is located close to the observation well (Chapter 3.5) and in experiments where the scattering object is sited in the uppermost crust beneath the detecting system. The inversion for the perturbation in the elastic parameters will fail if a Green function is applied that does not contain the appropriate near field terms. However, at a distance farther than 2λ, the near field terms have decayed sufficiently and the far field solution can be applied. At this distance, the mean value of the relative error between total and far field solution is 15% and 2% for the $\hat{r}$ and $\hat{\theta}$-components, respectively. The generalized amplitude distance relations (Figs. 2.2, 2.3) can be used to determine the scattered amplitudes for any case of low frequency elastic wave scattering as long as the results are normalized by the actual experiment parameter $k_p R$.

The availability of an exact solution made it possible to compute errors for the application of the Rayleigh approximation and associated solutions and to investigate them as a function of various parameters. The representation of the nonlinear Rayleigh approximation as a linear and quadratic Rayleigh-Born approximation revealed, for the relative error, a strong dependence on the scattering angle for both the $\hat{r}$- and $\hat{\theta}$-component. For a fixed parameter perturbation, it was found that the $\hat{r}$-component incurs a larger error for forward scattering than for scattering perpendicular to the direction of incidence. Four distinct lobes about 45^o off the axis of wave incidence developed for the error in the $\hat{\theta}$-component. In both cases the application of the quadratic Rayleigh-Born approximation reduced this error by a factor of 5. These results suggest that if

the orientation of primary source, scatterer and receiver are known, then it is possible to estimate the accuracy of the approximation due to linearization of the problem.

The increase in magnitude of parameter perturbation caused increasing magnitudes in the relative error for linear and quadratic approximations, although the exact amount depends on the sign of the perturbation. For a positive increase of 100%, the maximum error amounts to 9% and 17% for the quadratic and linear Rayleigh-Born approximation, respectively. A decrease in elastic parameters caused a larger error. For the case of a void (−100%), the deviation was determined to be 19% for the quadratic and 37% for the linear approximation. As a consequence, a more flexible interpretation of the magnitude of parameter perturbation is justified. As could be seen, the inequality (eq. 2.21) represents a very conservative limit, whereas a linearization in the case of perturbations below $\sim$ 20% should produce reliable results. In the case of inversion for the parameter perturbations, the difference between the linear and quadratic Rayleigh-Born approximation can be applied to correct the result after every iteration in the inversion procedure. A faster and more stable algorithm should be the result.

In order to facilitate the estimation of the relative error due to linearization of the problem, an approximation of the error was derived, entirely based on the deviations in the elastic parameters from the background. This enables one to estimate the error prior to an experiment based on a minimum of information and may help to improve the planing of the investigations. It was found that the equation provides an adequate representation of the relative error in the linear Rayleigh-Born approximation for a parameter perturbation of up to $\pm$20%.

One of the assumptions of the Rayleigh approximation is that the value of k_pR is small compared to 1. However, thus far no exact evaluation of this limit has been performed. The investigation of the Rayleigh limit for k_pR as a function of perturbation in the elastic parameters (allowing for various errors between the exact solution and Rayleigh approximation) produced surprisingly high values for the limit over almost the entire range of perturbation between

-100% and $+300\%$. Maximum values of more than 0.9 were reached. A relation between the Rayleigh limit and the accepted error as a function of parameter perturbation was found. The high values for the Rayleigh limit allow the validity of Rayleigh scattering (eq. 2.34) to be extended further toward the range of Mie scattering ($R \rightarrow \lambda$), and thus open a broader range for the application of elastic wave Rayleigh scattering.

The results of this chapter have direct consequences for the planing stage and the successful conduction of seismic experiments in which scattered waves are measured and inverted to determine subsurface properties. The investigation of the near field limit for the influence of a scatterer is important for cross-hole experiments (e.g.), where the sources may be close to an inhomogeneity of unknown location. If a Green function containing near field terms is available, the placement of receivers within a distance of 2λ from the inhomogeneity could prove beneficial as large scattered amplitudes can be recorded. The possible extension of the Rayleigh limit to higher values is an advantage for the parametrization of inversion techniques. Most inversion techniques inverting scattered data rely on the Rayleigh approximation as a means to linearize the problem which implies that the inhomogeneities are point scatterers. Therefore a fine discretization of the medium is necessary to meet the requirement of a long wavelength relative to the scatterer size. However, the new results relax this limit and consequently a coarser grid spacing or, similarly, higher frequencies could be applied to the inversion technique. The investigation of these factors is the subject of the following chapter.

Chapter 3

Theory and Numerical Inversion of the Nonlinear Scattering Problem

3.1 Introduction

The inversion of scattered elastic waves to determine subsurface structures has become an active area of research in recent years. The need to determine medium properties like elastic constants, scattering and anelastic attenuation (Lees et al., 1994), to detect and locate fracture zone (Vasco et al. 1995), partially molten zones (Zucca et al., 1989; Romero et al., 1993) and hydrocarbon deposits, for example, led to the development of waveform inversion in addition to travel time tomography techniques.

Elastic waves propagating through an inhomogeneous medium are affected in two ways. Their travel time is delayed or advanced depending on the nature of the inhomogeneities, and energy from the incident wave is scattered throughout the medium arriving at different times at the point of observation. The bulk of this scattered energy is delayed and becomes evident as various phases arriving after the direct wave in the seismogram (Aki, 1969; Korn, 1990). This energy is generally referred to as coda. However, the coda contains valuable information about the medium and is the target of waveform inversion techniques (Tura, 1990).

Although the determination of the velocity structure by travel time inversion is a viable tool to subsurface imaging, it lacks the ability to estimate elastic properties, e.g. revealing information on the state of anelastic attenuation in

the medium. Furthermore, a problem which may arise in the use of velocities is that effects present in the elastic moduli and density may be diminished by the tendency to cancel each other in the equations for the P wave and S wave velocity, $\sqrt{(K+4\mu/3)/\rho}$ and $\sqrt{\mu/\rho}$, respectively. Gritto et al. (1995 b) showed that the bimodal character of a medium, deduced from borehole data, is only weakly observable in the velocity logs, but clearly evident in the bulk and shear modulus as well as the density. Therefore, it could prove advantageous to invert for the elastic moduli, as they may be more sensitive to changes of the subsurface structure.

Recently, Korneev and Johnson (1993 a,b) derived a solution for the scattering of an elastic P wave by a spherical inclusion of arbitrary contrast. In this section an asymptotic solution for this problem, the low frequency Rayleigh approximation investigated in Chapter 2, will be used to solve the problem of inverting for the location and elastic parameters of inhomogeneities. This approximation offers several advantages. As presented by Gritto et al. (1995 a), it was shown that near field terms of the Rayleigh approximation dominate over far field terms up to a distance of 2 λ of the incident wave from the inhomogeneity. Thus, for the case of a typical cross hole experiment, where the target often is an inhomogeneity with unknown location, the use of long wavelengths may cause the receiver to be within 2 λ of the inhomogeneity. Therefore, near field terms become necessary and are considered in the present formulation. Simultaneously, because of the long wavelengths, the solution to the problem becomes less dependent on the shape of the inhomogeneity and should be applicable to a wider class of scatterers.

The problem of inverting for the elastic parameters of inhomogeneities is inherently nonlinear. Therefore, in the past the problem has been linearized assuming small perturbations in the elastic properties with respect to the background medium which generally limits the application to the treatment of weak inhomogeneities (Chapter 2.4) (Lo et al., 1988). As shown in Chapter 2, this weak scattering assumption can be relaxed to a certain degree without tolerating too large errors. However, in many cases encountered in subsurface imaging

the inhomogeneities reveal strong contrasts, and therefore the linearized inversion fails to produce reliable results. The Rayleigh approximation, as stated in equations (2.6) and (2.7), exhibits a practical feature that can be used to solve this problem. As will be shown in the present chapter, it is possible to solve the scattered wavefield for the elastic parameters in an exact and direct way, therefore, extending the applicability of the inversion to a completely new class of strong inhomogeneities in the subsurface.

The degree of nonlinearity of the elastic parameters as a function of perturbation varies considerably over the magnitude of perturbation encountered in inversion problems. This relationship is investigated and conclusions for linear and nonlinear inversions are drawn.

Various techniques are available to solve inverse problems. In many cases of tomographic inversion a discretization of the model space is chosen to express the problem in matrix formulation. This work is based on the same principle using singular value decomposition (SVD) to invert the matrix describing the problem. The disadvantage of this time consuming inversion process is balanced by the insight gained in understanding the inversion which is essential in the process of developing a new approach. Using SVD, important problems like resolving power, variance of the result, stability of the inversion, and related questions will be studied for various geometries.

Chapter 2 addressed the importance of near field terms in the vicinity of inhomogeneities. The influence of near field terms on the quality of the inversion of cross hole data will be shown for a typical underground geometry. Results include inversions based on Green functions with and without near field terms. The model resolution for these two cases is investigated and results indicate a possible source of misinterpretation for the case of a far field Green function, if the final interpretation is based on the model resolution. Furthermore, the importance of sufficient coverage of well placed sources and receivers to achieve best resolution will be addressed.

The case of strong nonlinear scattering will be investigated using the model of a cavity representing a strong scatterer. The feasibility to resolve the strong

contrast between the cavity and the surrounding medium will be tested. The 3-dimensional scattering of energy by an inclusion is a function of many parameters. The distribution of energy can vary greatly depending on the incident wave, its wavelegths in relation to the size of the inhomogeneity, the distance of observation from the inclusion, and the elastic parameters of the medium. Thus it is essential to study the scattering properties of the medium under investigation first, before a successful survey can be planed. For the case of a cavity, it will be shown which typical survey geometries are most favorable for the inversion of scattered waves.

3.2 The Non-Linear Inversion Problem

The solution to the scattering problem outlined in Chapter 2 will be the basis for the 3-dimensional inversion for the location and the elastic parameters of an inhomogeneity. The inversion is based on the assumptions that the locations of sources and receivers are known as well as the elastic parameters of the background medium. However, mathematically there is no restriction on the location and the spacing between receivers and source locations. In the following, a point pressure source exciting P waves and a receiver located at distances of r_0 and r, respectively, from the center of the inclusion are assumed (Figure 3.1).

In Chapter 2, the equation governing the scattering process, are expressed in terms of the Lamé parameter λ, the shear modulus μ, and the density ρ. For a better understanding of the physical processes describing the scattering problem, the Lamé parameter henceforce will be substituted by the bulk modulus K which facilitates the description and the understanding of the nonlinear scattering case. This substitution provides a means to decompose the scatterer into equivalent force terms and to relate them to the physics of the problem. Thus rewriting equations (2.6) and (2.7) in terms of K, μ and ρ yields

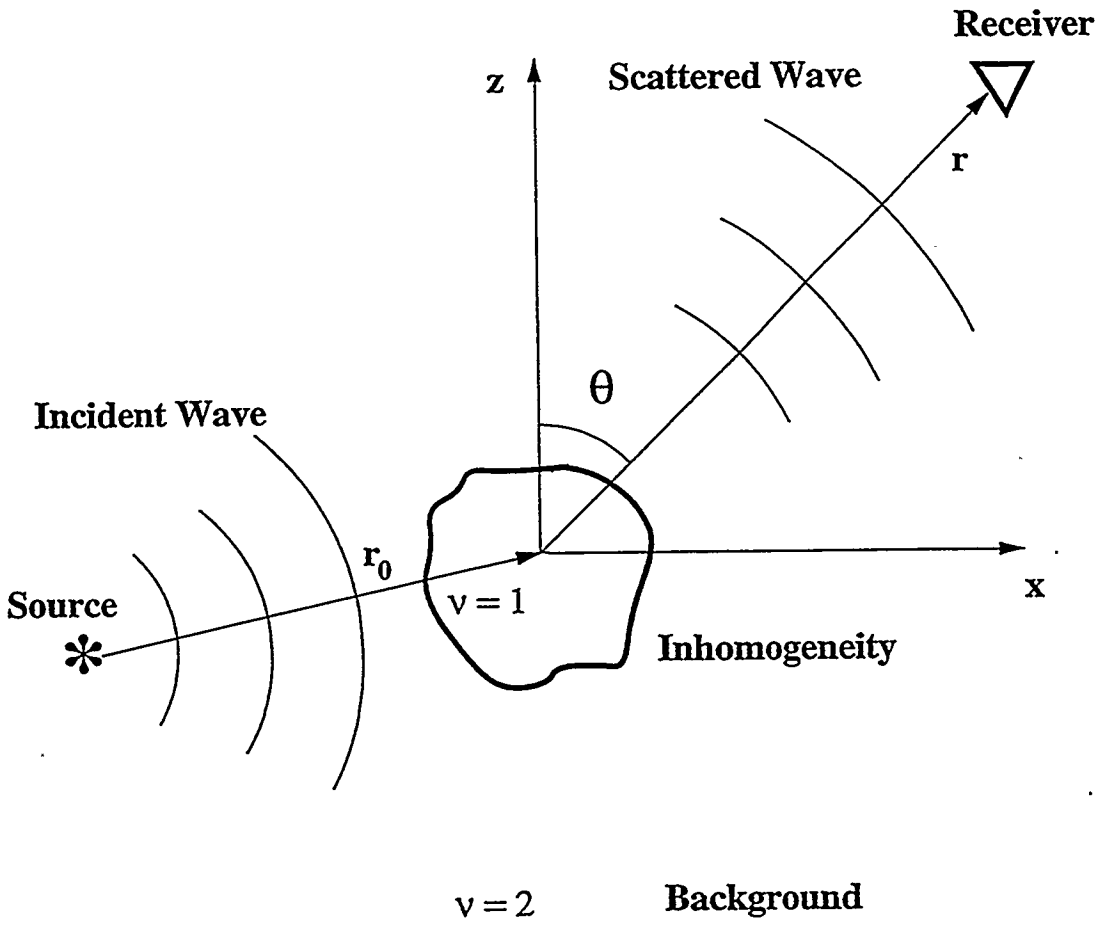

Figure 3.1: Geometry of the problem. The properties of the inhomogeneity and the background are denoted by $\nu = 1$ and $\nu = 2$, respectively. A spherical wave, generated by a point pressure source, is incident upon the inhomogeneity. Again, the scattered wave is a function of $\hat{r}$ and $\hat{\theta}$.

$$
\begin{aligned}
\mathbf{U}_p &= (\mathbf{U}_p)_r\hat{\boldsymbol{r}} + (\mathbf{U}_p)_\theta\hat{\boldsymbol{\theta}} \\
&= A\Bigg\{\Bigg[\frac{-\left(\frac{K_1}{K_2}-1\right)}{\left(1-\frac{4}{3}\gamma^2\right)+\left(\frac{K_1}{K_2}-1\right)}C_0W_{0r}^p(Z_p) + \left(\frac{\rho_1}{\rho_2}-1\right)C_1W_{1r}^p(Z_p)cos\theta \\
&+ \frac{2}{3}\left(\frac{\mu_1}{\mu_2}-1\right)\frac{\gamma^2}{D}C_2W_{2r}^p(Z_p)(1-3cos^2\theta)\Bigg]\hat{\boldsymbol{r}} \\
&- \Bigg[-\left(\frac{\rho_1}{\rho_2}-1\right)C_1W_{1\theta}^p(Z_p)sin\theta \\
&+ 2\left(\frac{\mu_1}{\mu_2}-1\right)\frac{\gamma^2}{D}C_2W_{2\theta}^p(Z_p)sin2\theta\Bigg]\hat{\boldsymbol{\theta}}\Bigg\} \qquad (3.1)
\end{aligned}
$$

$$
\begin{aligned}
\mathbf{U}_s &= (\mathbf{U}_s)_r\hat{\boldsymbol{r}} + (\mathbf{U}_s)_\theta\hat{\boldsymbol{\theta}} \\
&= B\Bigg\{\Bigg[2\left(\frac{\rho_1}{\rho_2}-1\right)C_1W_{1r}^s(Z_s)cos\theta + 2\left(\frac{\mu_1}{\mu_2}-1\right)\frac{\gamma}{D}C_2W_{2\theta}^p(Z_s)(3cos^2\theta-1)\Bigg]\hat{\boldsymbol{r}} \\
&+ \Bigg[-\left(\frac{\rho_1}{\rho_2}-1\right)C_1W_{1\theta}^s(Z_s)sin\theta + \left(\frac{\mu_1}{\mu_2}-1\right)\frac{\gamma}{D}C_2W_{2\theta}^s(Z_s)sin2\theta\Bigg]\hat{\boldsymbol{\theta}}\Bigg\} \qquad (3.2)
\end{aligned}
$$

using the definitions of equations (2.8), (2.9), (2.10), (2.19) and (2.20).

From equations (3.1) and (3.2) it is obvious that the scattered amplitude is nonlinear in terms of K and μ. However, because of the similar structure of the coefficients a_2 and b_2 in equation (2.4) which is based on the symmetry in the shape of the scatterer, it is possible to introduce the substitution

$$
m_K = \frac{\left(\frac{K_1}{K_2}-1\right)}{q_K+\left(\frac{K_1}{K_2}-1\right)}, \qquad q_K = \left(1-\frac{4}{3}\gamma^2\right)^{-1} \qquad (3.3)
$$

$$m_\mu = \frac{\left(\frac{\mu_1}{\mu_2} - 1\right)}{q_\mu + \left(\frac{\mu_1}{\mu_2} - 1\right)}, \qquad q_\mu = \left(\frac{2}{15}\left(3 + 2\gamma^2\right)\right)^{-1} \tag{3.4}$$

$$m_\rho = \left(\frac{\rho_1}{\rho_2} - 1\right) \tag{3.5}$$

which yields a system of equations which is linear in the new nondimensional parameters m_K, m_μ and m_ρ

$$\begin{aligned}
\mathbf{U}_p &= (\mathbf{U}_p)_r \hat{\boldsymbol{r}} + (\mathbf{U}_p)_\theta \hat{\boldsymbol{\theta}} \\
&= A\Bigg\{\Bigg[-m_K C_0 W^p_{0r}(Z_p) + m_\rho C_1 W^p_{1r}(Z_p) cos\theta + \frac{2}{3}\gamma^2 \frac{m_\mu}{q_\mu} C_2 W^p_{2r}(Z_p)(1 - 3cos^2\theta)\Bigg]\hat{\boldsymbol{r}} \\
&- \Bigg[m_\rho C_1 W^p_{1\theta}(Z_p) sin\theta + 2\gamma^2 \frac{m_\mu}{q_\mu} C_2 W^p_{2\theta}(Z_p) sin2\theta\Bigg]\hat{\boldsymbol{\theta}}\Bigg\}
\end{aligned} \tag{3.6}$$

$$\begin{aligned}
\mathbf{U}_s &= (\mathbf{U}_s)_r \hat{\boldsymbol{r}} + (\mathbf{U}_s)_\theta \hat{\boldsymbol{\theta}} \\
&= B\Bigg\{\Bigg[2m_\rho C_1 W^s_{1r} cos\theta + 2\gamma \frac{m_\mu}{q_\mu} C_2 W^p_{2\theta}(Z_s)(3cos^2\theta - 1)\Bigg]\hat{\boldsymbol{r}} \\
&+ \Bigg[-m_\rho C_1 W^s_{1\theta}(Z_s) sin\theta + \gamma \frac{m_\mu}{q_\mu} C_2 W^s_{2\theta}(Z_s) sin2\theta\Bigg]\hat{\boldsymbol{\theta}}\Bigg\}.
\end{aligned} \tag{3.7}$$

In the following m_K, m_μ and m_ρ will be referred to as moments, although they must not be confused with the common seismological definition of a moment of an earthquake as a measure of size. However, the term moment is

justified as reference to a source excitation mechanism in the sense that m_K is responsible for a volume change, and therefore, excites scattered P waves only, whereas m_μ and m_ρ represent a force couple and a single force, respectively, exciting both, scattered P and S waves (Wu and Aki, 1985; Tarantola, 1986).

Equations (3.6) and (3.7), revealing a linear relation between the scattered amplitudes and m_K, m_μ and m_ρ, can easily be inverted to solve for the moments. The substitution in equations (3.3) and (3.4) introduced a closed form of the functions including m_K and K_1, and m_μ and μ_1, and therefore, once the moments m_K, m_μ, and m_ρ are found, equations (3.3), (3.4), and (3.5) can be transformed to solve for the moduli and the density, yielding

$$K_1 = \left(q_K \frac{m_K}{1 - m_K} + 1\right) K_2 \tag{3.8}$$

$$\mu_1 = \left(q_\mu \frac{m_\mu}{1 - m_\mu} + 1\right) \mu_2 \tag{3.9}$$

$$\rho_1 = (m_\rho + 1)\, \rho_2. \tag{3.10}$$

The advantage of solving for the moments, rather than the elastic parameters directly, is two-fold. The first and foremost benefit is the option to solve the nonlinear scattering problem in a direct and exact way. Arbitrarily large contrasts can be calculated exactly without much computational effort by solving for the elastic parameters directly, greatly increasing the applicability beyond conventional methods relying on linearized solutions. Second, the moments m_K, m_μ and m_ρ are dimensionless quantities, therefore producing functions of comparable magnitudes, which results in a more stable inversion process. In

contrast, solving for the elastic parameters directly, which by comparison reveal a difference in magnitude of 10^6 (e.g. bulk or shear modulus compared to density), can cause unstable inversion conditions even for well conditioned cases.

3.3 Characterization of the Nonlinear Dependence of the Elastic Parameters on the Moments

The characterization of the nonlinear nature of the scattering problem provides an insight into the difficulties that may occur if a linearized approximation is applied. Equations (3.8) and (3.9) can be transformed to relate dimensionless properties of the elastic parameters to the dimensionless moments m_K and m_μ. Rewriting equations (3.8) and (3.9) in terms of the relative perturbations in K and μ, it is possible to derive an equivalent dependence for both moments, yielding

$$\frac{\delta K}{K_2} = q_K \, F(m_K) \tag{3.11}$$

$$\frac{\delta \mu}{\mu_2} = q_\mu \, F(m_\mu), \tag{3.12}$$

where the nonlinear dependence for both moduli is represented by the same function

$$F(m) = \frac{m}{1-m} \tag{3.13}$$

and m denotes the inversion parameters m_K and m_μ.

This function is plotted in Figure 3.2. The values for m range from $-\infty$ to 1.0. At $m = 1.0$ the solid line approaches the physical limit. For this case, the moduli of the inhomogeneity are much greater than those of the background. The limit is represented by a rigid body that does not deform under loading (e.g. the displacement vanishes). Decreasing m between 1 and 0 rapidly decreases the value for the moduli and the inhomogeneity gradually becomes weaker. At $m = 0$ the moduli of the inhomogeneity and the background have equal values (homogeneous medium). For $m < 0$, the moduli continue to decrease until they vanish for $m \to -\infty$, representing the case of a vacuum.

The curvature of the graph clearly indicates the asymmetry about $m = 0$. For $m \to 1$ the graph becomes strongly nonlinear and overly sensitive to small changes in m, whereas for $m \to -\infty$ the graph becomes approximately linear. This has two implications. First, the common problem of inverting waveforms scattered by small deviations about $m = 0$ is complicated by the fact that small negative perturbations have a different dependence on m than small positive perturbations. Therefore, linearized approximations of the inversion problem will have a distinct performance depending on the sign of the perturbation. Second, since the dependence of the elastic parameters on the moments becomes almost linear for extreme negative perturbations, e.g. a cavity, large changes in the moments produce small changes in the elastic properties only. Therefore, it could prove difficult to distinguish, based on scattered waves, between a cavity and a low density yet solid inhomogeneity. Simultaneously, for large positive perturbations small changes in the moments produce large changes in the elastic parameters, and thus the inversion of large positive contrasts may not be reliable due to unstable results.

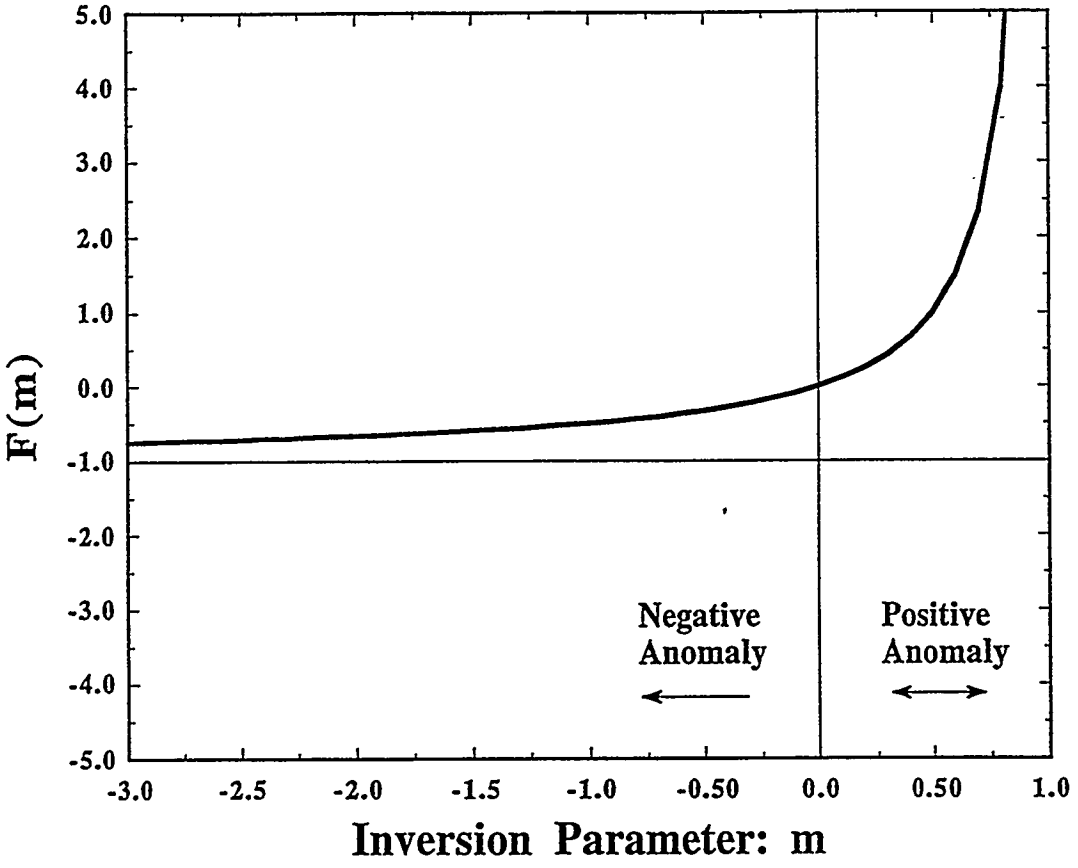

Figure 3.2: Nonlinear dependence of the deviation in the elastic moduli with respect to the moments m_K, and m_μ. The deviation in the moduli is represented by $F(m)$, while the moments are given by m.

3.4 Matrix Formulation of the Scattering Problem and the Solution by Singular Value Decomposition

In Chapter 3.2 the scattering problem was formulated in terms of the moments m_K, m_μ and m_ρ as functions of the spherical coordinates $\hat{r}$ and $\hat{\theta}$ (eqs. 3.6 and 3.7). This section is concerned with reformulating the problem in matrix form and subsequently solving it by singular value decomposition (SVD). Since all of the seismic field data are recorded by components arranged in cartesian coordinates, a rotation from spherical to cartesian coordinates is applied prior to the matrix formulation.

Combining equations (3.6) and (3.7) yields the total scattered field

$$\mathbf{U}^{tot}_{sc,r,\theta} = \mathbf{U}_{p,r,\theta} + \mathbf{U}_{s,r,\theta}. \tag{3.14}$$

Introducing functions containing all distance dependences the scattered field can be written as

$$\begin{aligned}
\mathbf{U}^{tot}_{sc,r,\theta} \;=\; & k^{pp}_{Kr} m_K \hat{r} \;+\; k^{pp}_{\rho r} m_\rho \hat{r} \;+\; k^{pp}_{\mu r} m_\mu \hat{r} \\
& +\; k^{pp}_{\rho\theta} m_\rho \hat{\theta} \;+\; k^{pp}_{\mu\theta} m_\mu \hat{\theta} \\
& +\; k^{ps}_{\rho r} m_\rho \hat{r} \;+\; k^{ps}_{\mu r} m_\mu \hat{r} \\
& +\; k^{ps}_{\rho\theta} m_\rho \hat{\theta} \;+\; k^{ps}_{\mu\theta} m_\mu \hat{\theta}
\end{aligned} \tag{3.15}$$

with

$$k^{pp}_{Kr} \;=\; AC_0 W^p_{0r}(Z_p)\,, \quad k^{pp}_{\rho r} = AC_1 W^p_{1r}(Z_p) cos\theta$$

$$
\begin{aligned}
k^{pp}_{\mu r} &= \frac{2}{3} A \frac{\gamma^2}{q_\mu} C_2 W^p_{2r}(Z_p)(1 - 3cos^2\theta) \\
k^{pp}_{\rho\theta} &= -AC_1 W^p_{1\theta}(Z_p) sin\theta \ , \quad k^{pp}_{\mu\theta} = -2A \frac{\gamma^2}{q_\mu} C_2 W^p_{2\theta}(Z_p) sin2\theta \\
k^{ps}_{\rho r} &= 2BC_1 W^s_{1r}(Z_s) cos\theta \ , \quad k^{ps}_{\mu r} = 2B \frac{\gamma}{q_\mu} C_2 W^s_{2r}(Z_s)(3cos^2\theta - 1) \\
k^{ps}_{\rho\theta} &= -BC_1 W^s_{1\theta}(Z_s) sin\theta \ , \quad k^{ps}_{\mu\theta} = B \frac{\gamma}{q_\mu} C_2 W^s_{2\theta}(Z_p) sin2\theta. \qquad (3.16)
\end{aligned}
$$

The rotation between the two coordinate systems is achieved by introducing direction cosines ζ rotating the components $\hat{r}$ and $\hat{\theta}$ to $\hat{x}$, $\hat{y}$ and $\hat{z}$, yielding

$$
\begin{aligned}
\mathbf{U}^{tot}_{sc,x,y,z} &= \mathbf{U}_{p,x,y,z} + \mathbf{U}_{s,x,y,z} \\
&= k^{pp}_{Kr}\, m_K\, \zeta_{rx}\, \hat{x} \ + \ k^{pp}_{Kr}\, m_K\, \zeta_{ry}\, \hat{y} \ + \ k^{pp}_{Kr}\, m_K\, \zeta_{rz}\, \hat{z} \\
&+ k^{pp}_{\rho r}\, m_\rho\, \zeta_{rx}\, \hat{x} \ + \ k^{pp}_{\rho r}\, m_\rho\, \zeta_{ry}\, \hat{y} \ + \ k^{pp}_{\rho r}\, m_\rho\, \zeta_{rz}\, \hat{z} \\
&+ k^{pp}_{\mu r}\, m_\mu\, \zeta_{rx}\, \hat{x} \ + \ k^{pp}_{\mu r}\, m_\mu\, \zeta_{ry}\, \hat{y} \ + \ k^{pp}_{\mu r}\, m_\mu\, \zeta_{rz}\, \hat{z} \\
&+ k^{pp}_{\rho\theta}\, m_\rho\, \zeta_{\theta x}\, \hat{x} \ + \ k^{pp}_{\rho\theta}\, m_\rho\, \zeta_{\theta y}\, \hat{y} \ + \ k^{pp}_{\rho\theta}\, m_\rho\, \zeta_{\theta z}\, \hat{z} \\
&+ k^{pp}_{\mu\theta}\, m_\mu\, \zeta_{\theta x}\, \hat{x} \ + \ k^{pp}_{\mu\theta}\, m_\mu\, \zeta_{\theta y}\, \hat{y} \ + \ k^{pp}_{\mu\theta}\, m_\mu\, \zeta_{\theta z}\, \hat{z} \\
&+ k^{ps}_{\rho r}\, m_\rho\, \zeta_{rx}\, \hat{x} \ + \ k^{ps}_{\rho r}\, m_\rho\, \zeta_{ry}\, \hat{y} \ + \ k^{ps}_{\rho r}\, m_\rho\, \zeta_{rz}\, \hat{z} \\
&+ k^{ps}_{\mu r}\, m_\mu\, \zeta_{rx}\, \hat{x} \ + \ k^{ps}_{\mu r}\, m_\mu\, \zeta_{ry}\, \hat{y} \ + \ k^{ps}_{\mu r}\, m_\mu\, \zeta_{rz}\, \hat{z} \\
&+ k^{ps}_{\rho\theta}\, m_\rho\, \zeta_{\theta x}\, \hat{x} \ + \ k^{ps}_{\rho\theta}\, m_\rho\, \zeta_{\theta y}\, \hat{y} \ + \ k^{ps}_{\rho\theta}\, m_\rho\, \zeta_{\theta z}\, \hat{z} \\
&+ k^{ps}_{\mu\theta}\, m_\mu\, \zeta_{\theta x}\, \hat{x} \ + \ k^{ps}_{\mu\theta}\, m_\mu\, \zeta_{\theta y}\, \hat{y} \ + \ k^{ps}_{\mu\theta}\, m_\mu\, \zeta_{\theta z}\, \hat{z}. \qquad (3.17)
\end{aligned}
$$

Finally combining the distance dependent functions and direction cosines yields

$$\begin{aligned}
\mathbf{U}_{sc,x}^{tot} &= (c_{Kx}\, m_K + c_{\mu x}\, m_\mu + c_{\rho x}\, m_\rho)\ \hat{x} \\
\mathbf{U}_{sc,y}^{tot} &= (c_{Ky}\, m_K + c_{\mu y}\, m_\mu + c_{\rho y}\, m_\rho)\ \hat{y} \\
\mathbf{U}_{sc,z}^{tot} &= (c_{Kz}\, m_K + c_{\mu z}\, m_\mu + c_{\rho z}\, m_\rho)\ \hat{z}
\end{aligned} \tag{3.18}$$

where the c functions are defined as

$$\begin{aligned}
c_{Kx} &= k_{Kr}^{pp}\, \zeta_{rx} \\
c_{Ky} &= k_{Kr}^{pp}\, \zeta_{ry} \\
c_{Kz} &= k_{Kr}^{pp}\, \zeta_{rz} \\
c_{\mu x} &= k_{\mu r}^{pp}\, \zeta_{rx} + k_{\mu\theta}^{pp} \zeta_{\theta x} + k_{\mu r}^{ps}\, \zeta_{rx} + k_{\mu\theta}^{ps}\, \zeta_{\theta x} \\
c_{\mu y} &= k_{\mu r}^{pp}\, \zeta_{ry} + k_{\mu\theta}^{pp} \zeta_{\theta y} + k_{\mu r}^{ps}\, \zeta_{ry} + k_{\mu\theta}^{ps}\, \zeta_{\theta y} \\
c_{\mu z} &= k_{\mu r}^{pp}\, \zeta_{rz} + k_{\mu\theta}^{pp} \zeta_{\theta z} + k_{\mu r}^{ps}\, \zeta_{rz} + k_{\mu\theta}^{ps}\, \zeta_{\theta z} \\
c_{\rho x} &= k_{\rho r}^{pp}\, \zeta_{rx} + k_{\rho\theta}^{pp} \zeta_{\theta x} + k_{r_r}^{ps}\, \zeta_{rx} + k_{r_\theta}^{ps}\, \zeta_{\theta x} \\
c_{\rho y} &= k_{\rho r}^{pp}\, \zeta_{ry} + k_{\rho\theta}^{pp} \zeta_{\theta y} + k_{r_r}^{ps}\, \zeta_{ry} + k_{r_\theta}^{ps}\, \zeta_{\theta y} \\
c_{\rho z} &= k_{\rho r}^{pp}\, \zeta_{rz} + k_{\rho\theta}^{pp} \zeta_{\theta z} + k_{m_{\rho r}}^{ps}\, \zeta_{rz} + k_{m_{\rho\theta}}^{ps}\, \zeta_{\theta z}.
\end{aligned} \tag{3.19}$$

At this point it is convenient to rewrite equation (3.17) in matrix form as

$$\begin{bmatrix} U^{tot}_{sc,x} \\ U^{tot}_{sc,y} \\ U^{tot}_{sc,z} \end{bmatrix} = \begin{bmatrix} c_{m_{Kx}} & c_{m_{\mu x}} & c_{m_{\rho x}} \\ c_{m_{Ky}} & c_{m_{\mu y}} & c_{m_{\rho y}} \\ c_{m_{Kz}} & c_{m_{\mu z}} & c_{m_{\rho z}} \end{bmatrix} \begin{bmatrix} m_K \\ m_\mu \\ m_\rho \end{bmatrix} \tag{3.20}$$

or in short form

$$\mathrm{U} = \mathrm{C}\,\mathrm{M}. \tag{3.21}$$

Asssuming a typical cross borehole experiment with M source receiver combinations and a background medium which is parametrized into N volume elements (voxels), the matrix U is of dimensions $3M \times 1$, while C and M have dimensions $3M \times 3N$ and $3N \times 1$, respectively.

Since equation (3.20) is linear in m_K, m_μ and m_ρ, these moments can easily be computed by inverting the matrix C

$$\mathrm{M} = \mathrm{C}^{-1}\mathrm{U}. \tag{3.22}$$

A variety of methods exist to invert the matrix C, however, the method chosen here is SVD as it provides good diagnostic insight into the inversion problem. The C matrix can be decomposed into the product of three matrices (Menke, 1989)

$$\mathrm{C} = \mathrm{W}\Lambda\mathrm{V}^{\mathrm{T}} \tag{3.23}$$

where W is a matrix of orthogonal eigenvectors spaning the data space, while similarly V is a matrix of eigenvectors that span the model space. The matrix Λ is the diagonal matrix of non negative elements called singular values. The

singular values are arranged in decreasing order with the possibility of zero values. However, before the inverse can be computed the zero singular values and the related vectors in W and V have to be eliminated from the system. Thus the rank of the matrix is reduced which is indicated by the index p denoting the number of non-zero singular values. Once the decomposition is computed, the inverse of C is readily given by

$$\mathbf{C}^{-1} = \mathbf{V}_\mathbf{p}\Lambda_\mathbf{p}^{-1}\mathbf{W}_\mathbf{p}^\mathbf{T} \tag{3.24}$$

and thus, the solution to the inversion problem is given by

$$\widehat{\mathbf{M}} = \mathbf{V}_\mathbf{p}\Lambda_\mathbf{p}^{-1}\mathbf{W}_\mathbf{p}^\mathbf{T}\mathbf{U} \tag{3.25}$$

where $\widehat{\mathbf{M}}$ denotes the estimate of M. Furthermore, the decomposition of C into the matrices $\mathbf{W}_\mathbf{p}$ and $\mathbf{V}_\mathbf{p}^\mathbf{T}$ allows the performance of the inversion to be investigated. A measure of the resolving power of the model parameters can be computed using the matrix $\mathbf{V}_\mathbf{p}$ by

$$\mathbf{R} = \mathbf{V}_\mathbf{p}\mathbf{V}_\mathbf{p}^\mathbf{T}. \tag{3.26}$$

In a perfectly resolved model, R is equal to the identity matrix I. If model parameters become dependent on each other and can no longer be resolved, the value of the diagonal decreases and spreads out to neighboring elements. In this sense the rows of R are a qualitative measure for the resolution of each model parameter.

The variance for the model estimate is given by the covariance matrix

$$cov\widehat{\mathbf{M}} = \sigma_\mathbf{d}^2\mathbf{V}_\mathbf{p}\Lambda_\mathbf{p}^{-2}\mathbf{V}_\mathbf{p} \tag{3.27}$$

where σ_d^2 is the variance in the data, which is assumed to be uniform and independent of the model parameters. Thus, for a given data variance, the covariance of the model can be computed using SVD.

In addition to zero singular values, it may happen, for ill-conditioned problems, that these values are very small (close to zero). In these cases the estimate $\widehat{\mathrm{M}}$ of the model in equation (3.25) may have very large components which may be unrealistic in a physical sense. Therefore, a common practice is to damp the system of equations and stabilize its solution. In the present case damping is achieved by setting to zero small singular values and their associated column and row vectors in $\mathbf{W}$ and $\mathbf{V}^{\mathbf{T}}$, respectively. This causes the rank of the system to decrease. However, because the information contained in the omitted equations is negligible, the solution of the inversion is not affected while the result becomes more stable. The question of how many singular values have to be deleted to produce a stable and reliable solution is most important, yet no simple answer exists. In many cases, a trial and error approach is attempted to find the most stable inversion result. However, in this work a more objective measure will be presented.

Figure 3.3 shows a trade-off curve for a typical inversion problem. The uncertainty, defined as the normalized standard deviation of the model, is plotted against model resolution. For an overdetermined undamped system, the model resolution is perfect as one solution can always be found. However, the associated uncertainty reveals very large values that can reach magnitudes larger than the model estimate, thus rendering the inversion result useless. Damping the system causes the resolution to decrease together with the uncertainty, thus gradually decreasing the error of the estimate. However, a reliable model estimate has to have a well balanced resolution and uncertainty which requires a search for the right damping. For a trade-off curve with normalized axis, the best solution is provided by the resolution and uncertainty values associated with the point on the curve closest to the origin, which can be found by seeking the minimum length of a vector t between the origin and the curve. To deter-

mine this point, the undamped model estimate is computed and t determined by

$$|\mathrm{t}| = \sqrt{(1.0 - R)^2 + \left(sd\left(\widehat{M}\right)\right)^2} \tag{3.28}$$

where $sd\left(\widehat{M}\right)$ is the standard deviation or uncertainty of the model, and $(1.0-R)$ was used to compute the component of the t vector on the resolution axis (Figure 3.3). Damping the system is achieved by setting to zero the singular values and their associated vectors in W and $\mathbf{V}^{\mathbf{T}}$ and recomputing for every step the resolution R, the uncertainty $sd\left(\widehat{M}\right)$, and t. This process iteratively is repeated until t starts to increase again, at which point the previous values for the model estimate, resolution, and uncertainty are chosen as the optimum inversion result. Figure 3.4 shows the length of the vector t as a function of the iteration process. At inversion step number 38 the length starts to increase again, and the result of step number 37 is the optimum inversion. The resulting vector is shown in Figure 3.3. This procedure provides a fast and objective way to compute the most stable solution without repeating the time consuming SVD of the background matrix for every new damping step, as the damping is performed after the initial SVD.

3.5 Numerical Modeling of Near Field Inversion Cases

It was shown in Chapter 3.2 that the nonlinear scattering problem can be solved directly if the low frequency approximation (Rayleigh scattering) is applied. The advantage of quasi independence on the shape of the inhomogeneity, caused by the the long wavelength relative to the size of the scatterer, is paid for by the need to include near field terms in the solution. In a typical cross hole experiment with source and receiver wells separated by distances on the order of 10 m - 20 m, the location of the target prior to the investigation is

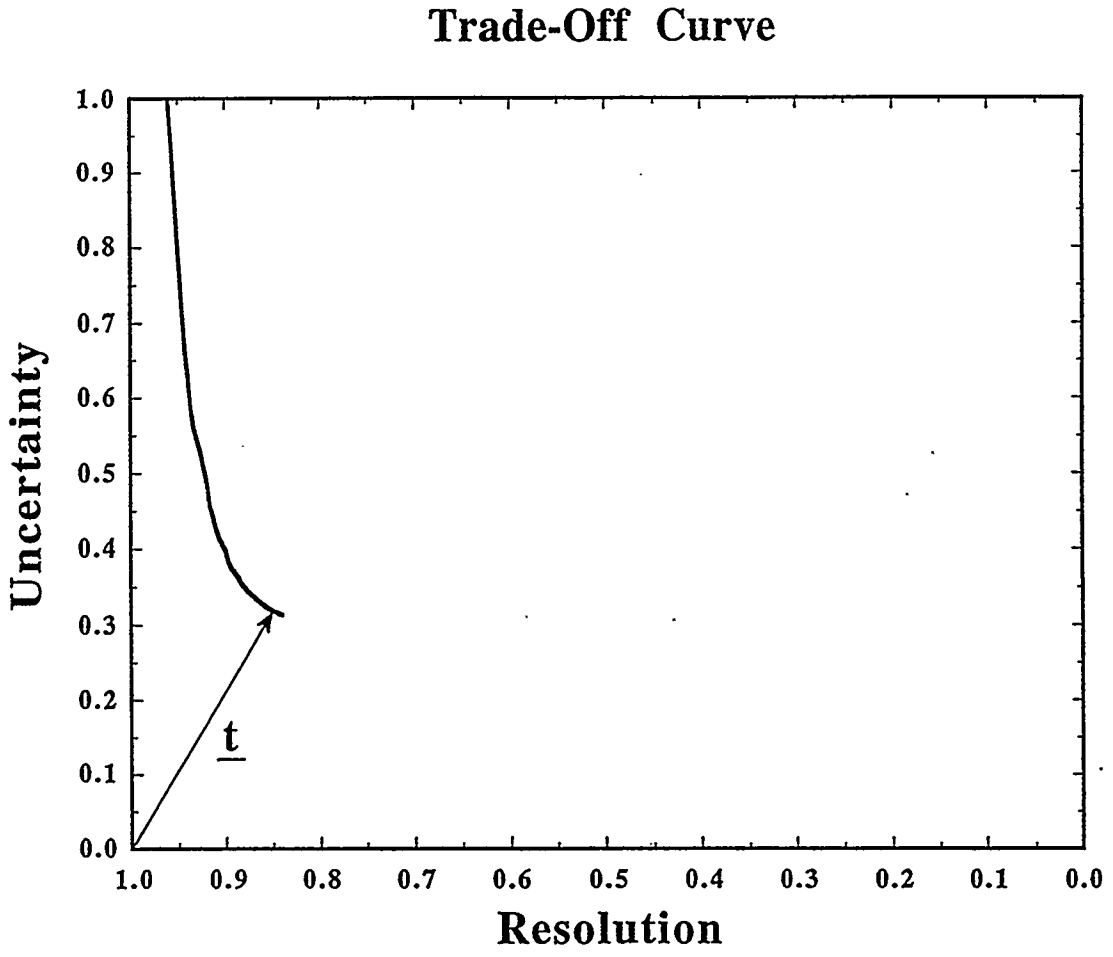

Figure 3.3: Trade-off curve for a typical inversion problem. The uncertainty, defined as normalized standard deviation of the model, is plotted versus the model resolution. The resolution axis is flipped to match perfect resolution with minimum uncertainty at the origin of the plot.

often unknown. However, the near field influence of an inhomogeneity extends to a distance of 2 wavelengths beyond the inhomogeneity (Chapter 2). Thus in the case of Rayleigh scattering, when the wavelength is much larger than the scatterer dimension, the receivers may well lie within the near field of the inhomogeneity. To illustrate this problem, the effect of a solution containing near field terms is evaluated with respect to a solution containing far field terms only, based on a numerical model of a field experiment.

This field experiment was conducted at the FRI site in the southern part of the Grimsel test facility in the Swiss Alps. The facility is run by the Swiss National Coorporative for Storage of Nuclear Waste (NAGRA) to conduct research on topics ranging from measurements of rock mechanical properties to hydrological studies to determine permeabilities of fractured zones in granite. A cross hole tomographic experiment was conducted to determine the location and extend of two fractured zones crossing an area of approximately 20 m by 10 m in size. A more detailed description of the FRI field site can be found in Chapter 4.1.

The numerical model of this test site extends 20 m in length and 10 m across. Sources and receivers are deployed in intervals of 2 m along the sides of the model (Figure 3.5). The background parameters are 5500 m/s and 3200 m/s for the P and S wave velocities, respectively, while the density is 2650 Kg/m^3. The attenuation in the model is determined by the relation

$$\begin{aligned} Q_p^{-1} &= \frac{(K_i + \frac{4}{3}\mu_i)}{(K_r + \frac{4}{3}\mu_r)} \\ Q_s^{-1} &= \frac{\mu_i}{\mu_r} \end{aligned} \tag{3.29}$$

where the indices i and r denote the imaginary and real part of the moduli, respectively. The complex parts of the elastic parameters are chosen such that the quality factor for the background amounts to $Q_{p,s} = 100$.

Three weak zones are defined as linear features running across the model

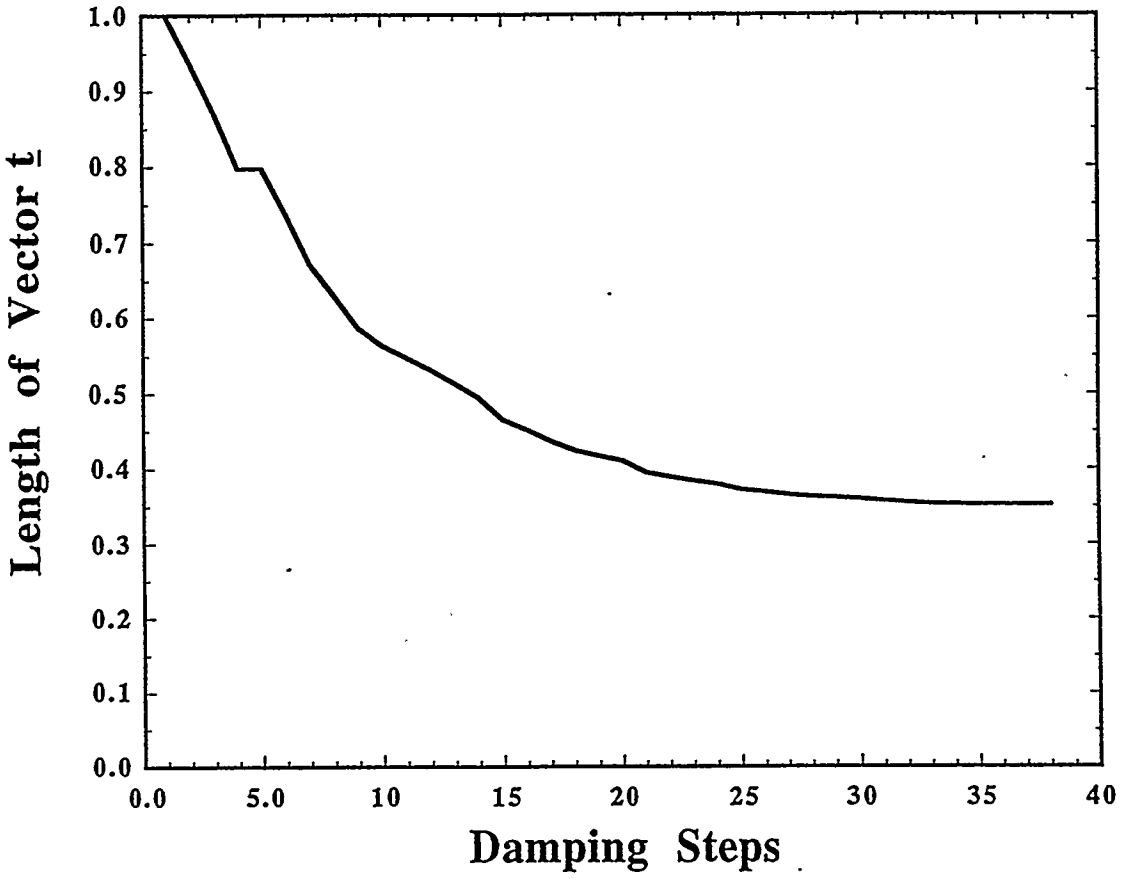

Figure 3.4: Length of the trade-off curve vector t as a function of damping steps.

from the upper left to the lower right corner (Figure 3.5, left panel), consisting of a decrease by -11 %, -5 % and -10 % in the velocities and density with respect to the background medium. Simultaneously, the quality factor was reduced to $Q_{p,s} = 10$. The parametrization of the model consists of 50 voxels with constant side lengths of 2 m. A single frequency for the forward modeling and the inversion is chosen to ensure that the wavelength of the incident wave is long compared to the inhomogeneities (one voxel in this model) and thus the requirements for Rayleigh scattering are met. Given the background velocity, a frequency of f = 445 Hz is chosen such that the resulting wavelength (λ = 12.4 m) is about six times larger than a single voxel. There are several objectives for this experiment. First, is it feasible to invert for the structure and to resolve the model parameters from each other considering the long wavelength used? Second, if so, is it feasible to distinguish between the 3 weak zones with almost identical properties, and third, what effect do the near field terms in the solution have on the quality of the inversion? For the nonlinear forward modeling, equation (3.1) is used to generate the scattered field at the receivers. The weak zone is modeled as a series of single inhomogeneities, for each of which the scattered field is computed independently before the superposition of all scattered fields is determined at each receiver site. The inversion is performed with the same parametrization as for the forward modeling, while the data is kept noise free, therefore providing a means to evaluate the performance of the inversion in relation to the use of a low frequency signal and the consideration or dismissal of near field terms alone.

The inversion is performed by solving the system of equations (3.20) containing near field terms and substituting the moments m_K, m_μ and m_ρ in equations (3.5), (3.6) and (3.7) to determine the elastic parameters K_1, μ_1 and ρ_1. The result is presented in Figures 3.5 and 3.6 showing the bulk modulus at the top, the shear modulus in the middle, and the density at the bottom of the plot. The real parts of the properties are shown in Figure 3.5 It is evident that the fractured zones are recovered, revealing distinct amplitudes for the three degrees of weakness for most of the fractured area. A decrease in resolution can be seen

by fading colors in the center of the image particularly for the bulk modulus and to a lesser degree for the density. The bulk modulus is the least constrained of the three properties, as it is only affecting P wave propagation, and thus, for the purpose of an inversion, can only be reconstructed from P to P scattered phases, whereas the shear modulus and the density can be determined from P to P and P to S wave scattering. Therefore, a reduction in model resolution due to a non-optimum geometry will first be apparent in the bulk modulus. In the present example the minimum resolution is about 0.75 for some pixels in the central row of the panel for the bulk modulus, indicating that they cannot be perfectly resolved from neighboring elements. Nevertheless, the surrounding pixels reveal a high level of resolution, indicates that these model parameters have been sufficiently resolved, and in this sense, they are independent to a high degree.

The imaginary parts (Figure 3.6) reveal a decrease in the quality of the inversion result. Whereas the shear modulus shows an acceptable result for the fracture zone as a whole, the result for the bulk modulus indicates a trend in amplitudes only, coinciding with the strike of the disturbance. The reason for the decrease in quality of the imaginary parts lies in the correlation between the real and imaginary parts. The larger amplitudes of the real parts represent a higher noise level for the small amplitudes of the imaginary parts. Therefore, the relative error is much larger for the imaginary parts, causing the reduction in quality.

Eliminating the near field terms in equation (3.20) and recomputing the inversion yields the result shown in Figure 3.7. Again, the model is plotted in the left panel for comparison. As can be easily seen, the inversion fails to produce any meaningful result, either in the amplitudes or in the geometric structure of the anomalies. However, the model resolution produced values comparable to those of the inversion including near field terms. Thus in a cross hole situation, the lack of near field terms can lead to situations where the inversion produces erroneous results which wrongfully are supported by acceptable model resolution. In such a case without further knowledge, a misleading evaluation of these

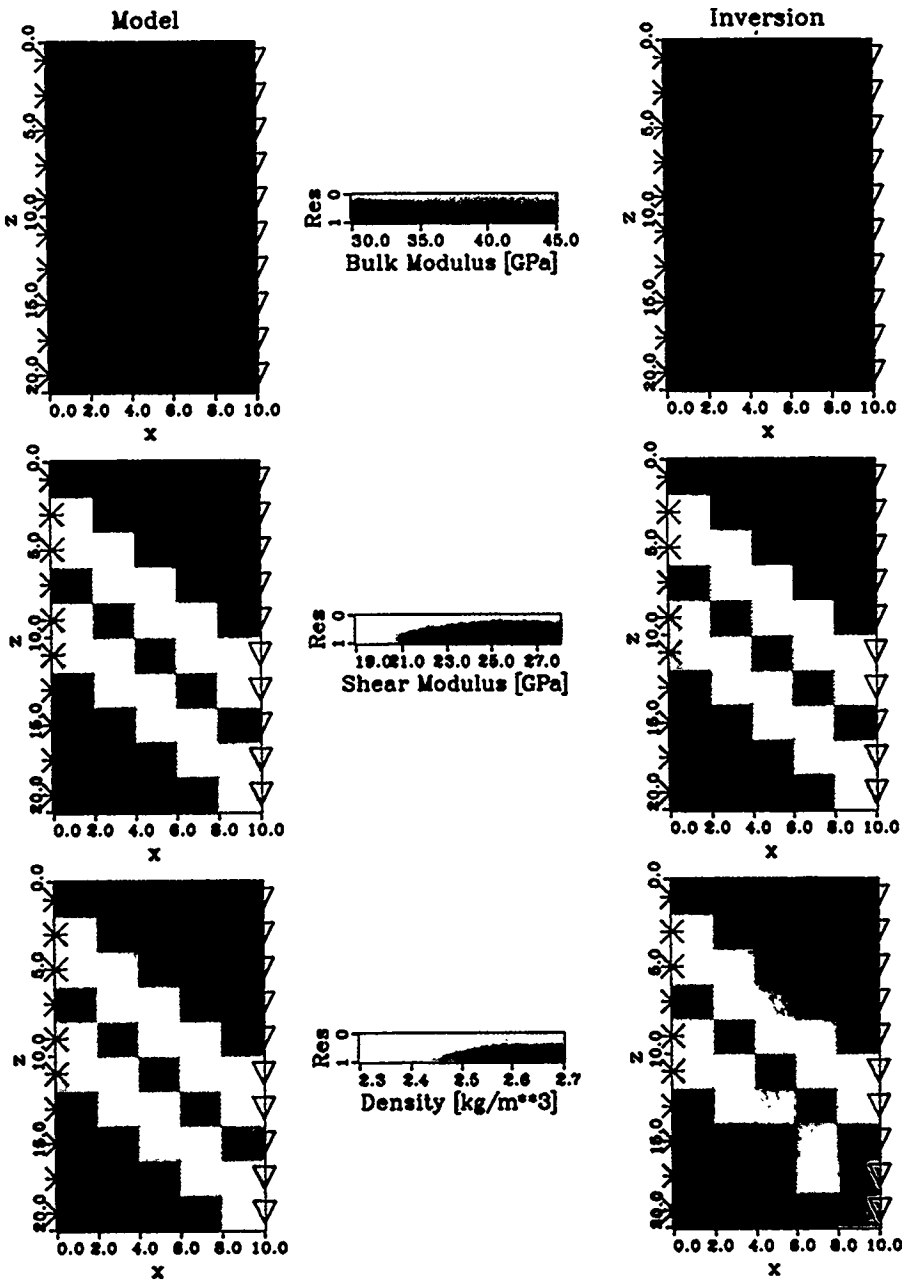

Figure 3.5: Inversion results for the real part of the elastic parameters computed with the total field Green function. The left panel shows the model, while the inversion result is given on the right. The bulk and shear modulus, as well as the density are presented in the top, middle and bottom of the plot respectively. Sources are denoted by stars, whereas receivers are given by triangles. The resolution is represented by the intensity of the color. Full saturation reveals perfect resolution, whereas fading to white indicates total loss of model resolution.

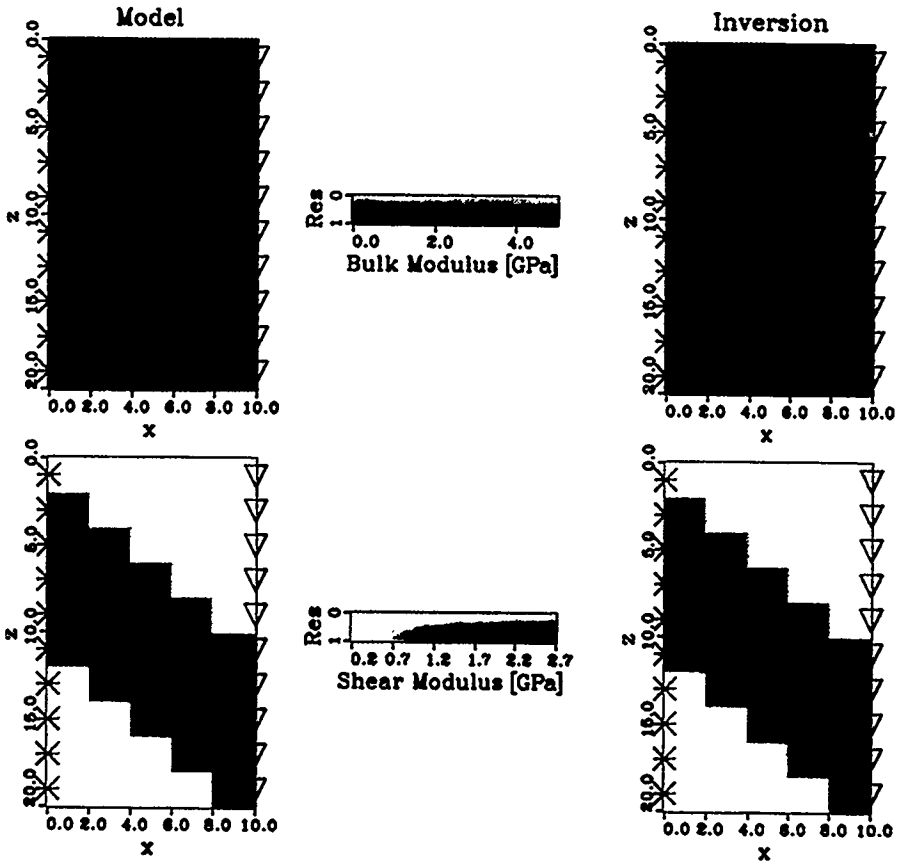

Figure 3.6: Inversion results for the imaginary part of the bulk and shear modulus computed with the total field Green funtion.

results can cause severe interpretation errors.

To investigate the improvement of the inversion result based on a better source receiver geometry, two receivers are added to the upper and bottom side of the model area. The improved geometry is shown in Figure 3.8 which reveals the inversion results for the real parts, whereas Figure 3.9 shows the results for the imaginary parts again. The improvement of the inversion is evident in both plots. All features are clearly recovered while the model resolution increased in those panels which revealed non perfect results before. The improvement is most remarkable for the imaginary parts which reveal an almost perfect inversion result. To emphasize this improvement, Figure 3.10 shows the resolution for the old and improved geometry for the real parts alone. In this figure the resolution is plotted in a color scheme with red denoting zero and green indicating perfect model resolution. The result derived from the old geometry is plotted in the left panel. The lowest value of about 0.75 for the bulk modulus can be found in the center towards the edges of the model. The shear modulus shows perfect resolution while the density reveals slight decreases in the central part of the model as well. The improvement is evident in the right panel with prefect model resolution for all parameters. In all cases the resolution increased not only at the edges of the model, close to the new receiver locations, but in the central parts of the model as well.

It can be learned from this example that a well designed geometry can provide favorable inversion results. In near field situations additional receivers at the side of the model add to the information content of the system by improving the angular coverage. Mathematically, this means that the scattered field described by the equations (3.1 and 3.2) becomes more distinct for different source receiver pairs, as for this case, the angle θ between a single pixel and the receivers takes on different values, in comparison to the case with all receivers lined up at one side of the model. Thus the situation can be avoided where the equations become almost equal, contributing little independent information to the solution of the system. This lack of information produces small singular values in the decomposition of the coefficient matrix, which will cause unstable

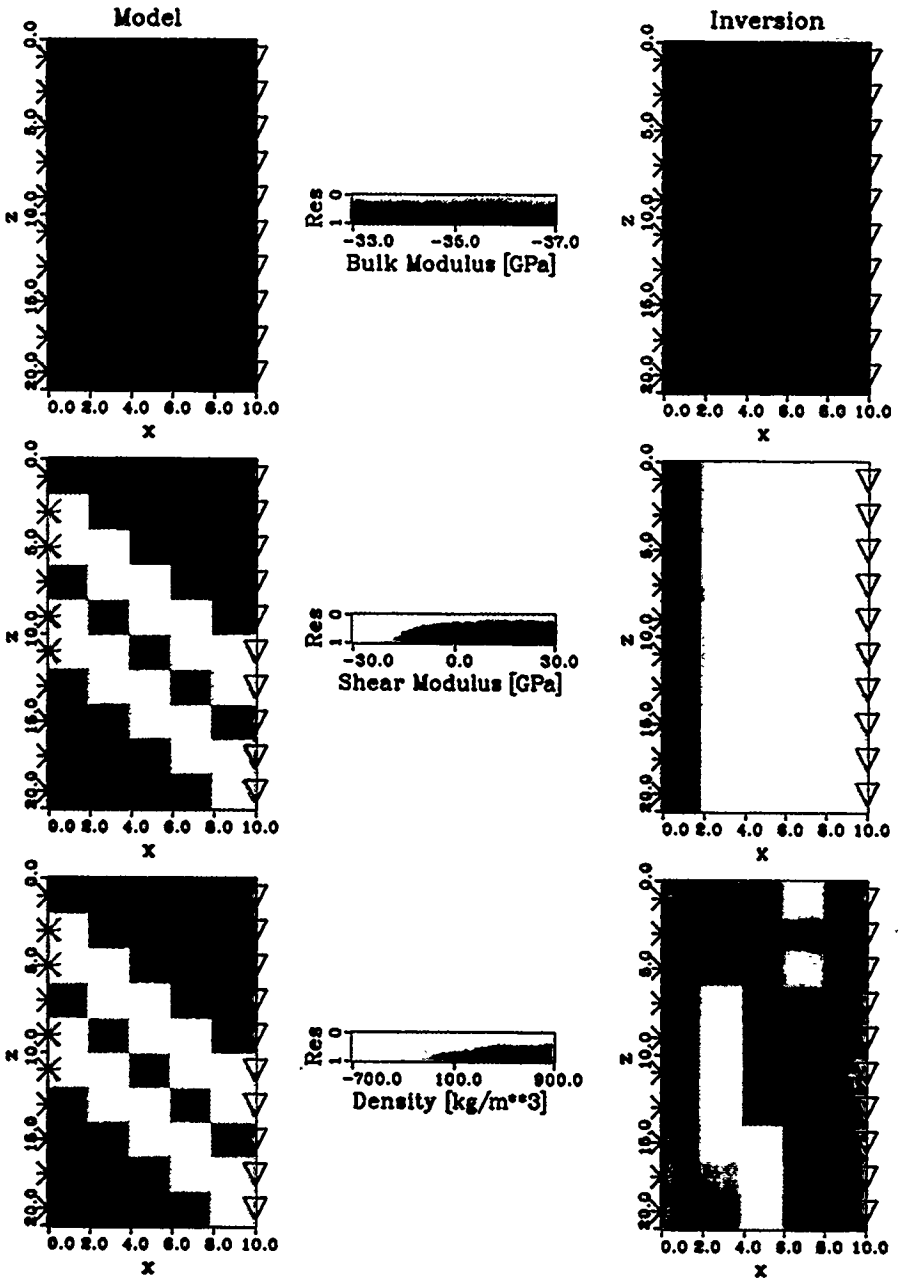

Figure 3.7: Inversion results for the real part of the elastic parameters computed with the far field Green function.

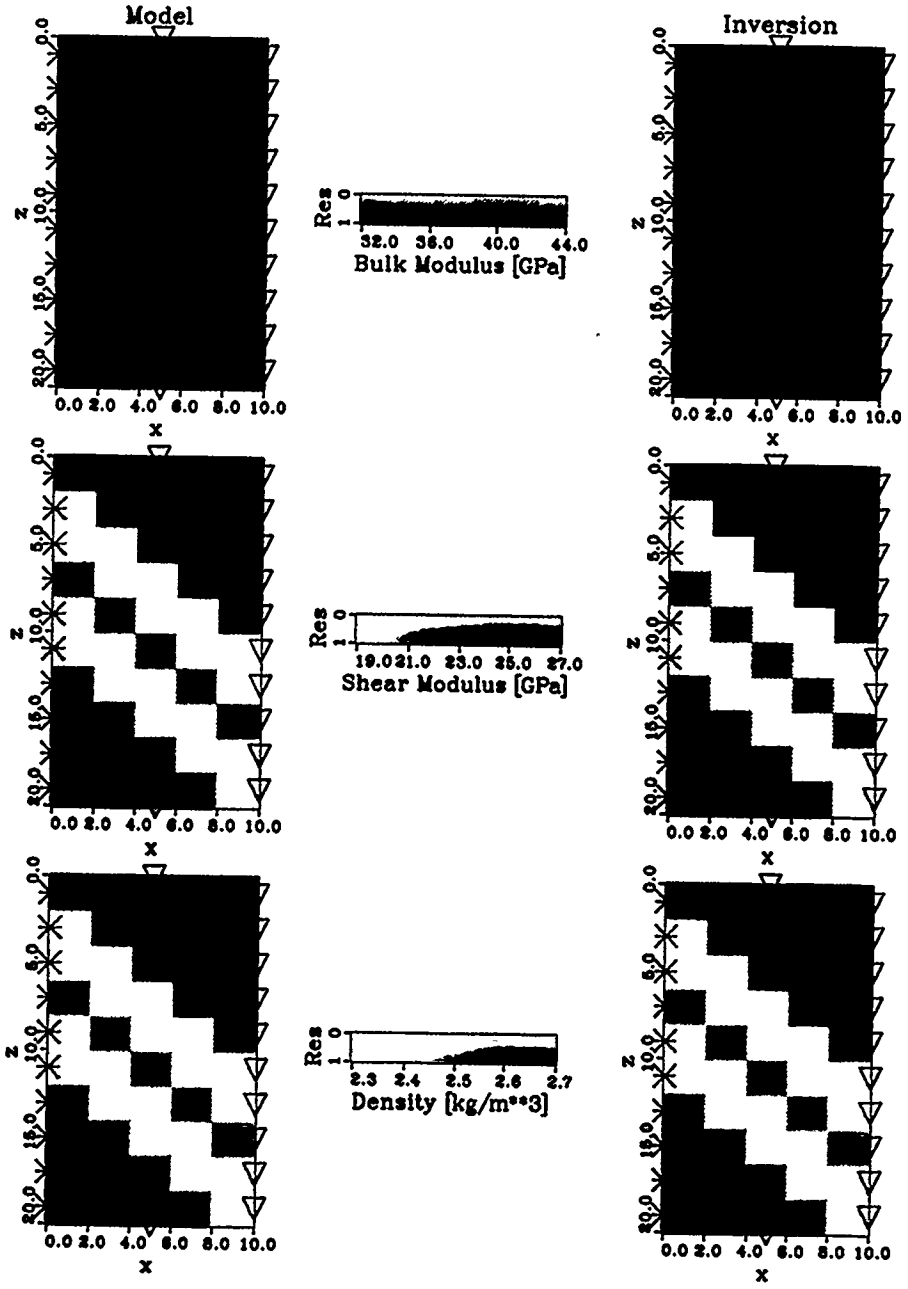

Figure 3.8: Improved inversion results for the real part of the elastic parameters computed with the total field Green function, due to better source receiver coverage. Note the additional receivers at the top and bottom of the panels.

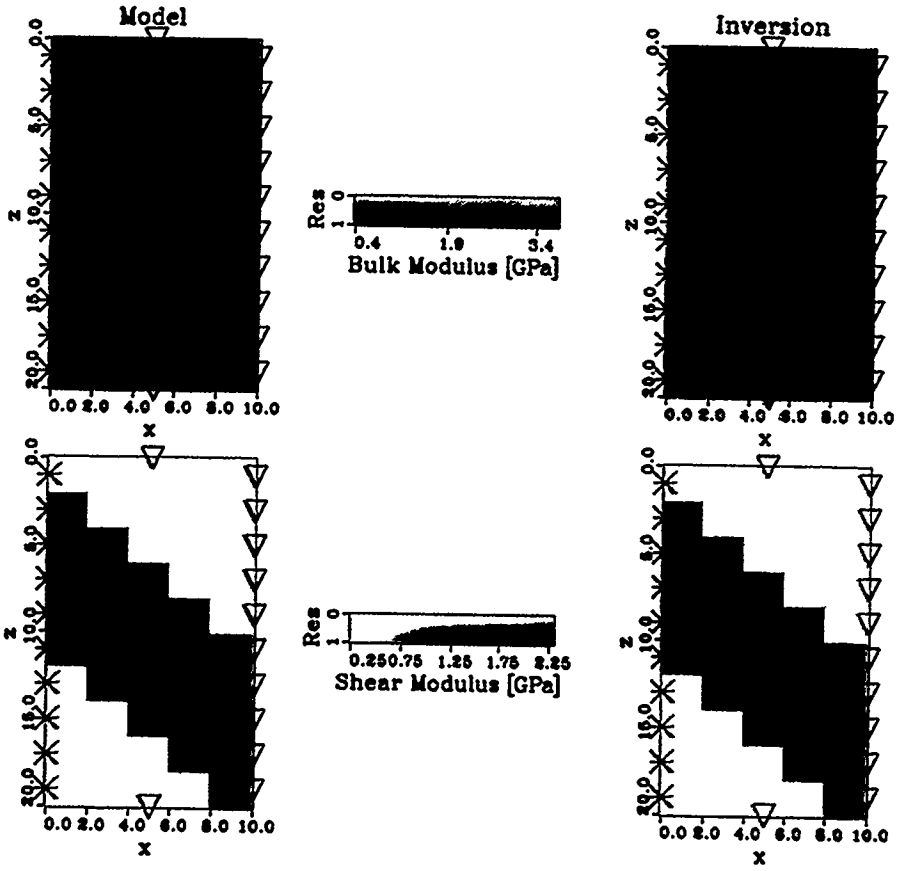

Figure 3.9: Improved inversion results for the imaginary part of the bulk and shear modulus computed with the total field Green funtion, due to better source receiver coverage.

inversion results.

3.6 Numerical Modeling of Strong Nonlinear Scatterers with Particular Consideration of Source Receiver Geometry

A common problem in geophysical exploration is the determination of the location and the size of cavities in the subsurface structure. The reasons are widespread, ranging from the detection of abandonded mine shafts to the verification of underground facilities for military purposes. In the past, attempts have been undertaken to solve this problem (Côte et al., 1995). However, although some methods provide a approximate location for the structure, most fail to give reliable estimates of the actual volume. The present section will address this problem, proposing a detailed study to ensure optimum inversion results for future investigations of this class of problems.

Cavities having a reduction of 100 % in their elastic properties with respect to the surrounding medium comprise a class of strong scatterers. Therefore, inversion approaches relying on a linearized solution are not suitable for the problem, as one of their main restrictions is the assumption of small perturbations in the elastic properties from the background medium. This fact is most unfortunate, considering the possible advantage of a good signal to noise ratio of the scattered waves caused by the large contrast in properties. However, the nonlinear approach introduced in Chapter 3.1 takes advantage of the strong scattered waves without being bound by any limitations regarding the scattering strength. Therefore, the possibility of inverting for the location and the structure of underground cavities is a promising feature of the present approach.

Considering the problem that the location and extent of a near surface cavity needs to be determined, the question arises as to what source and receiver geometry is most promising for a successful survey. Figure 3.11 depicts 4 com-

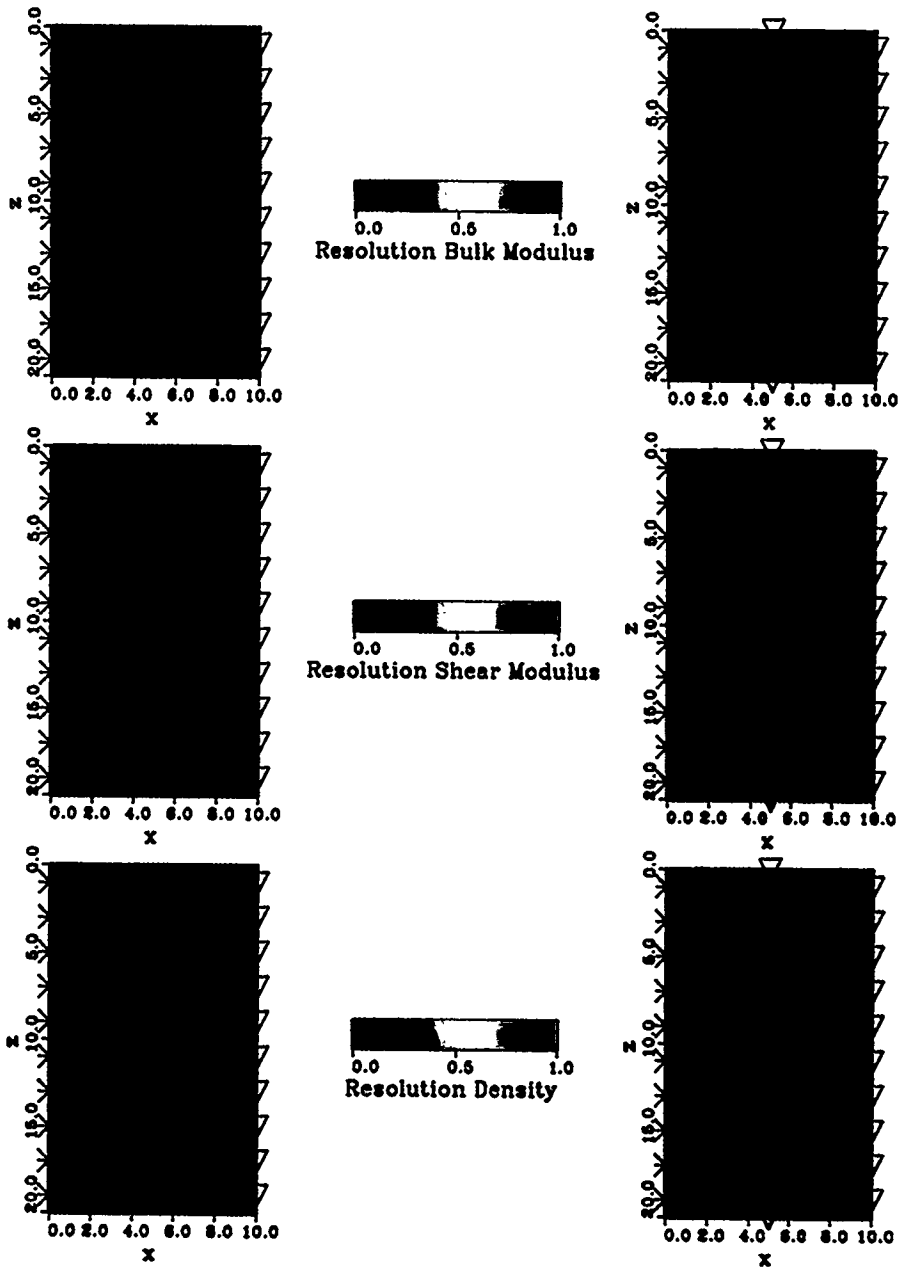

Figure 3.10: Resolution for the real part of the elastic properties for the case of ordinary transmission geometry (left panel) and improved source receiver geometry (right panel). The resolution is indicated by the color scheme (green: perfect resolution), (red: no resolution).

mon geometries in near surface exploration surveys. For the common situation of a cross hole experiment (Case A) the cavity is located in between the boreholes and transmission data is used to study the problem. However, for the case of only one borehole, a VSP survey can be conducted with sources at the surface and receivers in the less noisy borehole environment (Case B). In this case, forward and side scattered energy is considered depending on the exact location of the sources and receivers. Case C shows a situation where sources and receivers are both located in the same borehole and only back scattered waves are recorded. The advantage of this set up is that strong amplitudes from the incident field do not interfere with back scattered energy, and thus removal of the incident wavefield generally is not necessary. This compares to Case D where the same source receiver geometry is located at the surface, in the case where no borehole is available. This case may not be favorable for other reasons, such as multiple scattering in the inhomogeneous surface layers interfering with the primary scattered wavefield.

The question of which geometry is favorable over the others depends highly on the target under investigation. The 3-dimensional scattering of energy by an inclusion is a function of the incident wave, its wavelength in relation to the size of the inclusion, the distance of observation from the inclusion, and the elastic properties of the media involved. The distribution of scattered energy can vary greatly based on these factors, and therefore, it is imperative to study this problem before a successful survey geometry can be assigned. Figure 3.12 shows the scattering diagram of a sphere shaped cavity for an incident P wave generated by a point pressure source at a distance of 2 λ. The wavelength is 12 times larger than the diameter of the cavity. The scattered amplitudes are recorded at a radial distance of 2 λ from the center of the cavity. The P to P scattered amplitudes are plotted on the left side of the graph, while P to S converted amplitudes are given on the right. The scattered amplitudes are symmetric along the axis of wave incidence. It can be seen from this example that little energy is forward scattered for both P and S waves. While most of the scattered P wave energy is back scattered at 180°, the P to S converted

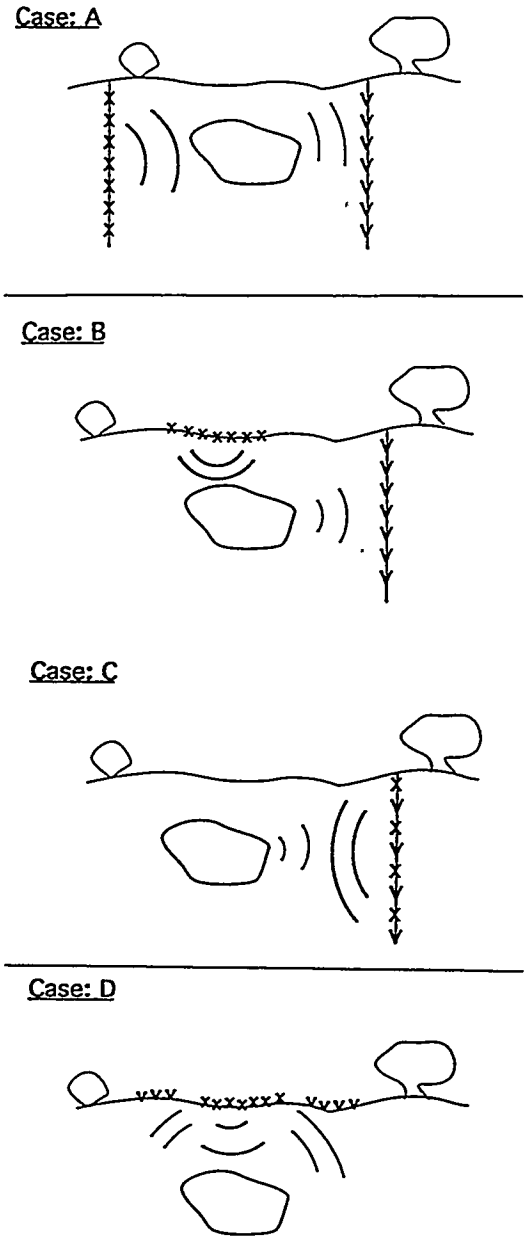

Figure 3.11: Four common geometries used in near surface exploration. X's denote sources while V's denote the receivers. Case A: borehole transmission survey, Case B: VSP survey, Case C: Reflection survey in borehole, Case D: Reflection survey at surface.

energy is back scattered at an angle of 135°. It is evident that more of the incident P wave amplitude is converted to scattered S waves than scattered P waves. In order to detect and to determine the properties of the cavity in this example, seismometers have to be deployed on the source side of the cavity to record the back scattered energy. To determine the bulk modulus, seismometers have to be arranged close to the source to record the back scattered P wave amplitudes which carry the information to estimate the bulk modulus (equation 3.1). As the source is at a distance of 2 λ from the cavity, seismometers should be placed at an equal distance of 2 λ from the cavity and the source to record the back scattered S wave energy under 135°. This energy is essential to constrain the location, as well as the shear modulus and the density which are zero for the case of a cavity. Any other seismometer locations will fail to record the largest scattered amplitudes and thus make it difficult to detect the presence of the cavity by means of scattered waveforms. This example is intended to demonstrate the need for a careful analysis of the complicated nature of the scattering processes.

Several aspects will be addressed in the present numerical example. First, it is important to determine the performance of the nonlinear inversion approach, as outlined in section 3.1, in the presence of a strong inhomogeneity. An appropriate test case is the model of an underground cavity. Second, does the source receiver geometry have as strong an influence as suggested by the last figure? And third, the spatial parameterization in the inversion thus far has always been identical to the parameterization used for forward modeling. In the following example the performance of different parameterizations for forward modeling and inversion is investigated. This case always arises in nature, where the incident wave samples a continuous medium and is affected by inhomogeneities on all scales. However, for the inversion the medium has to be parameterized into discrete blocks whose properties are being investigated. Thus it is desirable that the elastic quantities inside the discrete blocks are averaged over each single volume, therefore producing mean values of the properties which depend on the discretization. For the forward modeling the parametrization presented

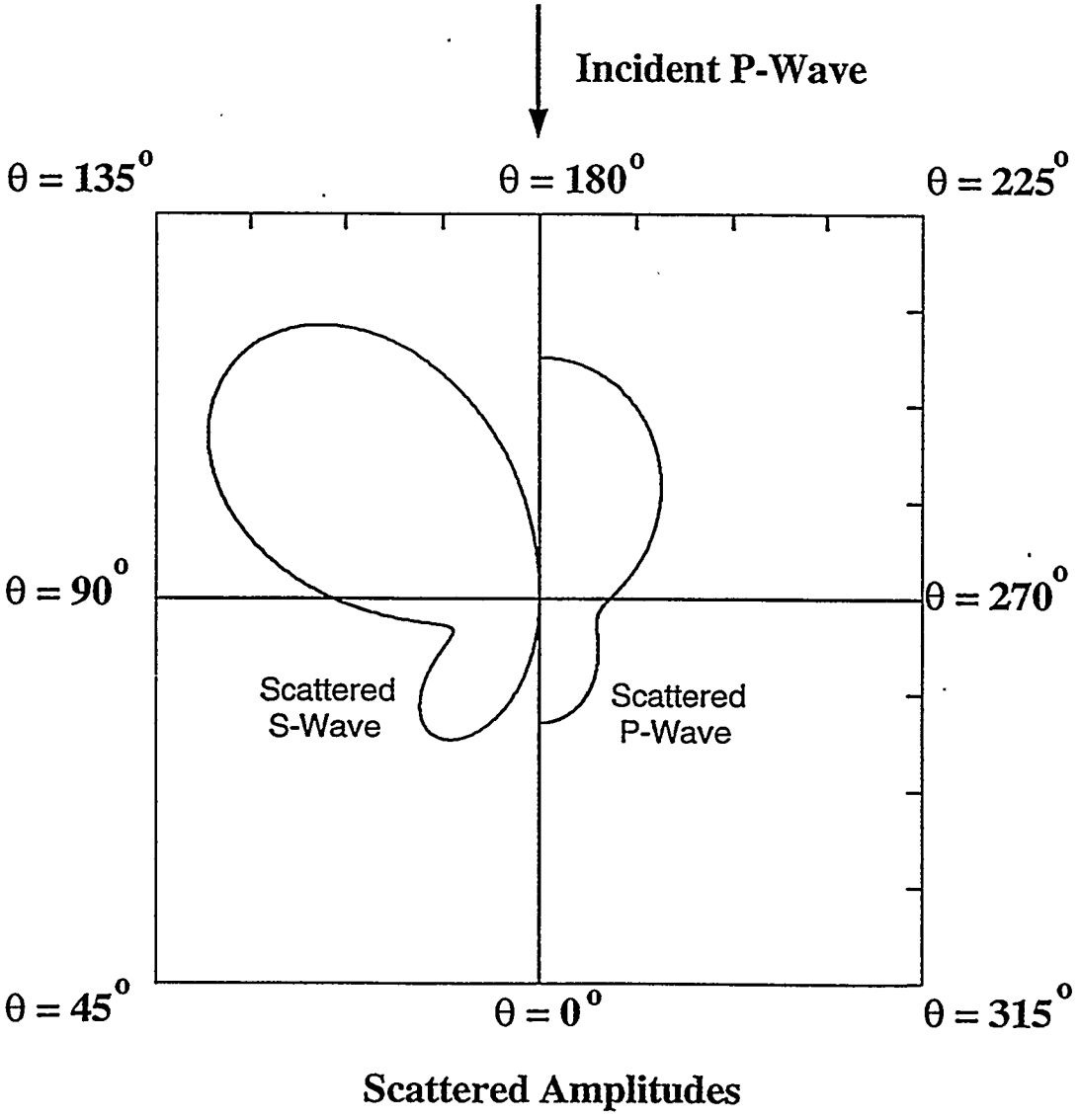

Figure 3.12: Scattering diagram for a sphere shaped cavity for the incidence of a P wave generated by a point pressure source at a distance of 2 λ from the center of the cavity. Although the scattered amplitudes are symmetric with respect to the direction of incidence, the scattered P wave is shown on the left, while the scattered S wave is given on the right of the line of incidence.

in Figure 3.13 (upper panel) is applied. The cavity is comprised of 64 voxels of volume 1 m^3, each of which is considered a small inhomogeneity. As before, the exact scattered wavefield is computed for each single voxel and their superposition calculated for each receiver site. The parameterization for the inversion is shown in the bottom panel of Figure 3.13, where each of the new voxels has a total volume of 8 m^3. The wavelength of the experiment was chosen to be about six times larger than the voxel size of the inversion, to satisfy the conditions for Rayleigh scattering. The purpose of the small discretization for the forward modeling lies in the physics of Rayleigh scattering. One of the underlying principles of Rayleigh scattering is that the wavelength is long compared to the scattering object such that there is no phase relation in the amplitudes that have been scattered by adjacent objects. The consequence for the forward modeling is that either the single voxels are chosen to be as small as possible, which is computationally expensive, or the distance of observation is increased such that the angle between the receiver and neighboring voxels becomes small enough so that the difference in the phases of the scattered waves vanishes. For the inversion, however, the discretization is chosen such that the size is small compared to the wavelength, yet the phase information between neighboring elements has to be preserved to resolve adjacent voxels. Therefore, it is desireable to decrease the distance of observation and keep the angle between adjacent voxels large enough to maintain the phase difference in the scattered waves. As can be seen, a trade off is evident in the modeling experiment between the optimum distance for forward modeling and the inversion. The best compromise for the example under investigation is determined to be at about 2 λ distance from the inhomogeneity. It is found for this distance that the phase relation between the small voxels in the forward modeling decreased sufficiently, while it is still possible to resolve adjacent elements in the inversion. This fact led to the choice of 2 λ as observation distance for the investigation of the scattered amplitudes in the last paragraph (Figure 3.12).

The numerical model of the cavity is shown in Figure 3.14. For reasons of brevity only one vertical slice through the model and only the real parts are

Parametrization for Forward Modeling

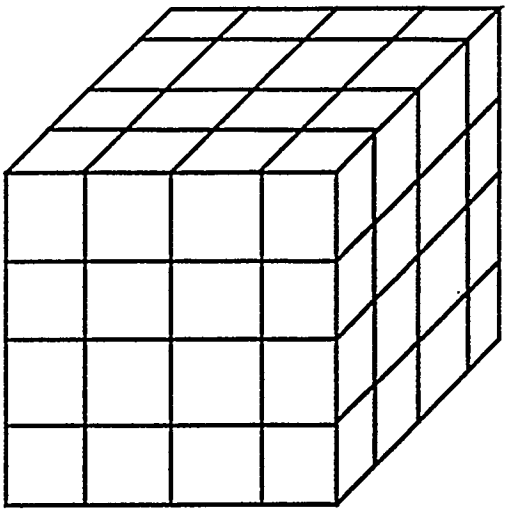

Parametrization for Inversion

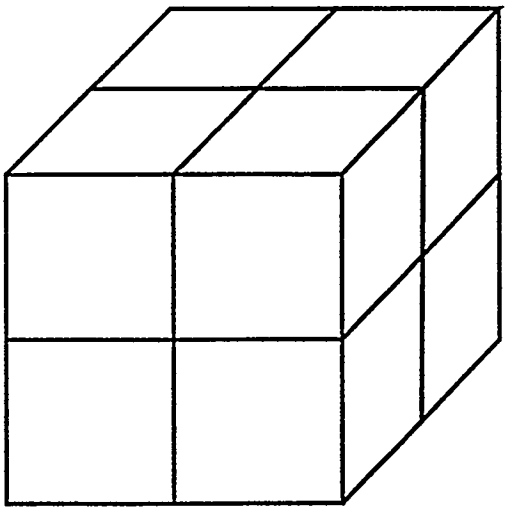

Figure 3.13: Parametrization of the model for the forward modeling (top) and the inversion (bottom). Total volume of the cavity is 64 m^3, with each voxel having a volume of 1 m^3 for the forward modeling (top), and 8 m^3 for the inversion (bottom).

displayed. For the forward modeling background values of $V_p = 4750\ m/s$, $V_s = 2750\ m/s$ and $\rho = 2000\ Kg/m^3$ are selected which translate into the bulk and shear modulus values presented in Figure 3.14. The parametrization, including the background medium surrounding the cavity, was chosen to study possible interferences between neighboring voxels with strong contrast in the elastic parameter. According to the choices of geometries in Figure 3.11, three set ups are selected for the inversion. A transmission survey, representing the cross hole case, a VSP geometry with sources located at the surface and receivers in the borehole, and a reflection survey, representing an array of both sources and receivers either at the surface or located in one borehole. Each of the three set ups consists of groups of 5 sources and 15 receivers. However, to reveal the effect of directivity in the amplitudes of the scattered waves on the performance of the inversion, the receivers are deployed in two different ways. One is a general set up of 15 receivers separated by 1 m spacing located at $\theta = 0°$ for the transmission case, at $\theta = 180°$ for the reflection, and at $\theta = 270°$ for the VSP case (refer to Figure 3.12 for orientation). Second, the receivers are split into 3 groups of 5 each deployed at $\theta = 315°$, $\theta = 0°$ and $\theta = 45°$ for the transmission, at $\theta = 225°$, $\theta = 180°$ and $\theta = 135°$ for the reflection, and at $\theta = 225°$, $\theta = 270°$ and $\theta = 315°$ for the VSP case. The purpose of the second set up is to record the maximum scattered P and S wave energy, simultaneously.

The results for the reflection survey are displayed in Figure 3.15. The results for the split receiver geometry (3 groups of 5 receivers) is shown in the left panel, while the single group geometry (1 group of 15 receivers) is given in the right panel. Because of space limitations in the figure, a star represents a group of 5 sources while a cross denotes 5 receivers. Similarly, the locations of the sources and receivers symbols are not drawn to scale, rather they should indicate their position relative to each other at a distance of 2 λ from the center of the inclusion in the right panel and additionally are separated by a distance of 2 λ in the left panel.

It is evident in the left panel of Figure 3.15 that the inversion produced good results for all three parameters. The background values are well recovered

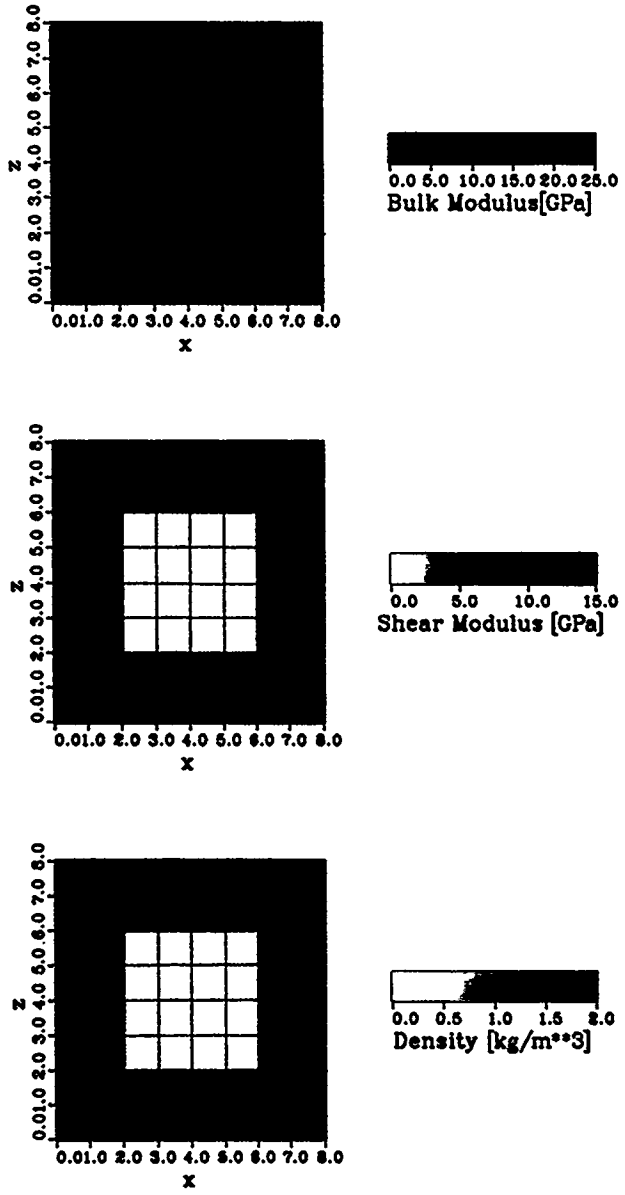

Figure 3.14: Numerical model for the real parts of the elastic parameters for the case of the cavity. The cavity is modeled by sixteen central voxels, while the outer delimiter represents the background medium.

and the values inside the cavity are close to zero. The background values for the bulk modulus show slightly larger deviations due to its decreased constraint depending on the scattered P wave only. No interference is evident between the strong contrasts across the cavity boundary. This is due to the fact that equation (3.1) is nonlinear in the elastic parameters and thus strong deviations can be accommodated in the inversion. In contrast, the inversion using the single receiver array failed to produce a meaningful result. Although the amplitudes scale in the correct magnitude range, their location has no relation to the model. It should be noted that, although a considerable amount of P wave energy is backscattered (Figure 3.12), the result for the bulk modulus reveals no improvement over the other parameters. This suggests that the poor geometry produced coupling between the bulk modulus and the remaining parameters, thus limiting the quality of the inversion result. For the transmission case (Figure 3.16) neither of the two geometries produced correct amplitudes or locations, with amplitudes ranging widely from negative to positive values. However, this is not surprising, as little energy is forward scattered for this example (compare to Figure 3.12). Finally the VSP geometry reveals intermediate results for both receiver arrays (Figure 3.17). In both cases the shear modulus and density show acceptable images, while the bulk modulus again produces no reliable result. Although the amplitudes for the shear modulus underestimate the cavity slightly (negative values) its location is well determined. The inversion for the density produced correct background values while the estimates for the cavity are slightly wrong. The increase in performance of the VSP over the transmission case can be explained by the fact that considerably more S wave energy is being side scattered (Figure 3.12), producing better inversion results for the shear modulus and the density.

This simple numerical experiment clearly demonstrates the complicated nature of the scattering of elastic waves. For a successful detection of a subsurface inhomogeneity it is imperative to incorporate all available information prior to the experiment and to investigate the scattering mechanism of the expected target body. Failure to do so, may lead to a wrong experimental design, which

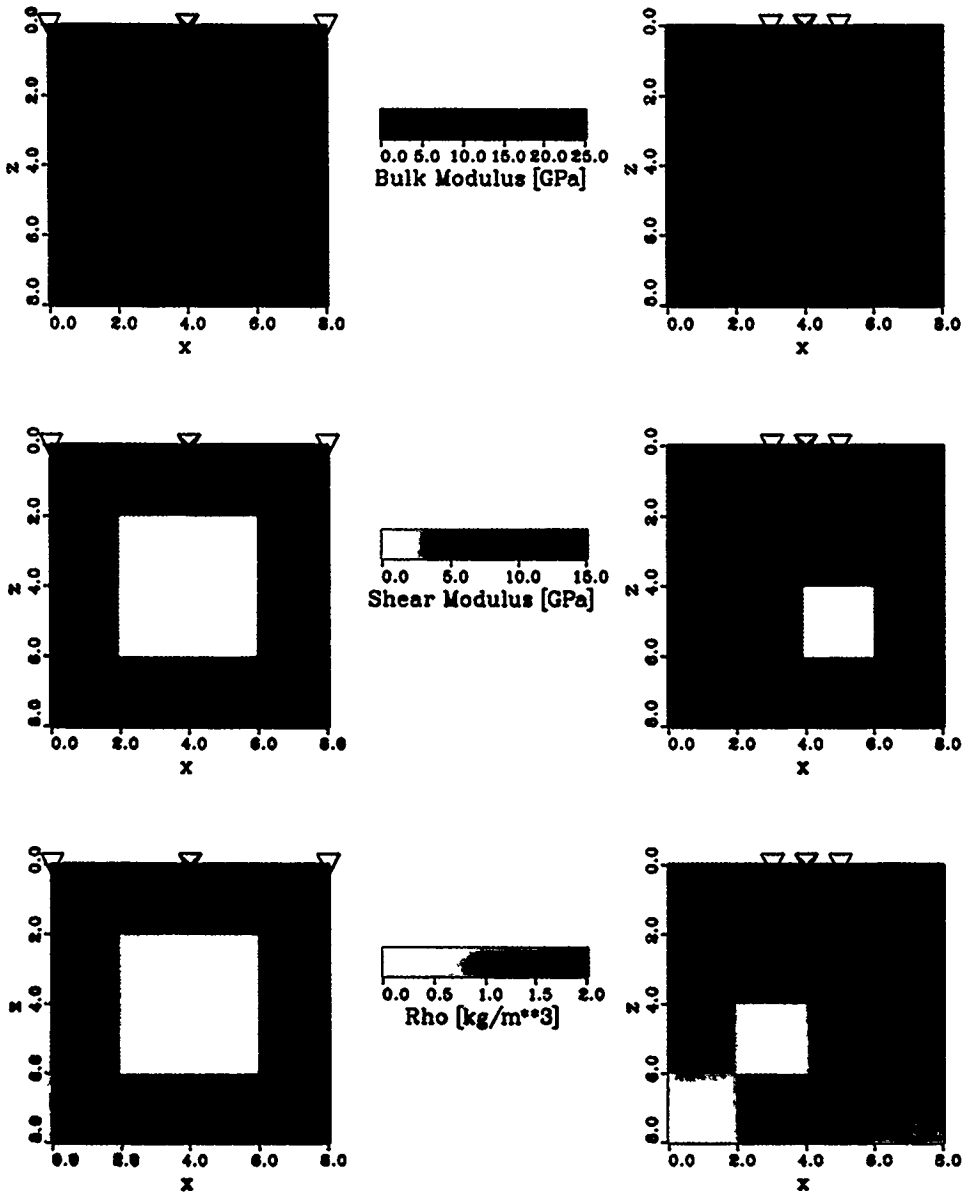

Figure 3.15: Inversion results for the real parts of the elastic parameters of the reflection survey. The cavity is represented by four central voxels, whereas the background is given by the surrounding area. The positions and number of sources and receivers are not to scale. One triangle and one star is representative for a group of 5 receivers and 5 sources, respectively, located at a distance of 2 λ from the center of the cavity. The left panel reveals the results for the geometry using three groups of 5 receivers each, located at $\theta = 225°$, $\theta = 180°$ and $\theta = 135°$ (refer to Figure 3.12 for orientation), while the right panel shows the results for one single group of 15 receivers located at $\theta = 0°$. In both cases the source is located at $\theta = 0°$.

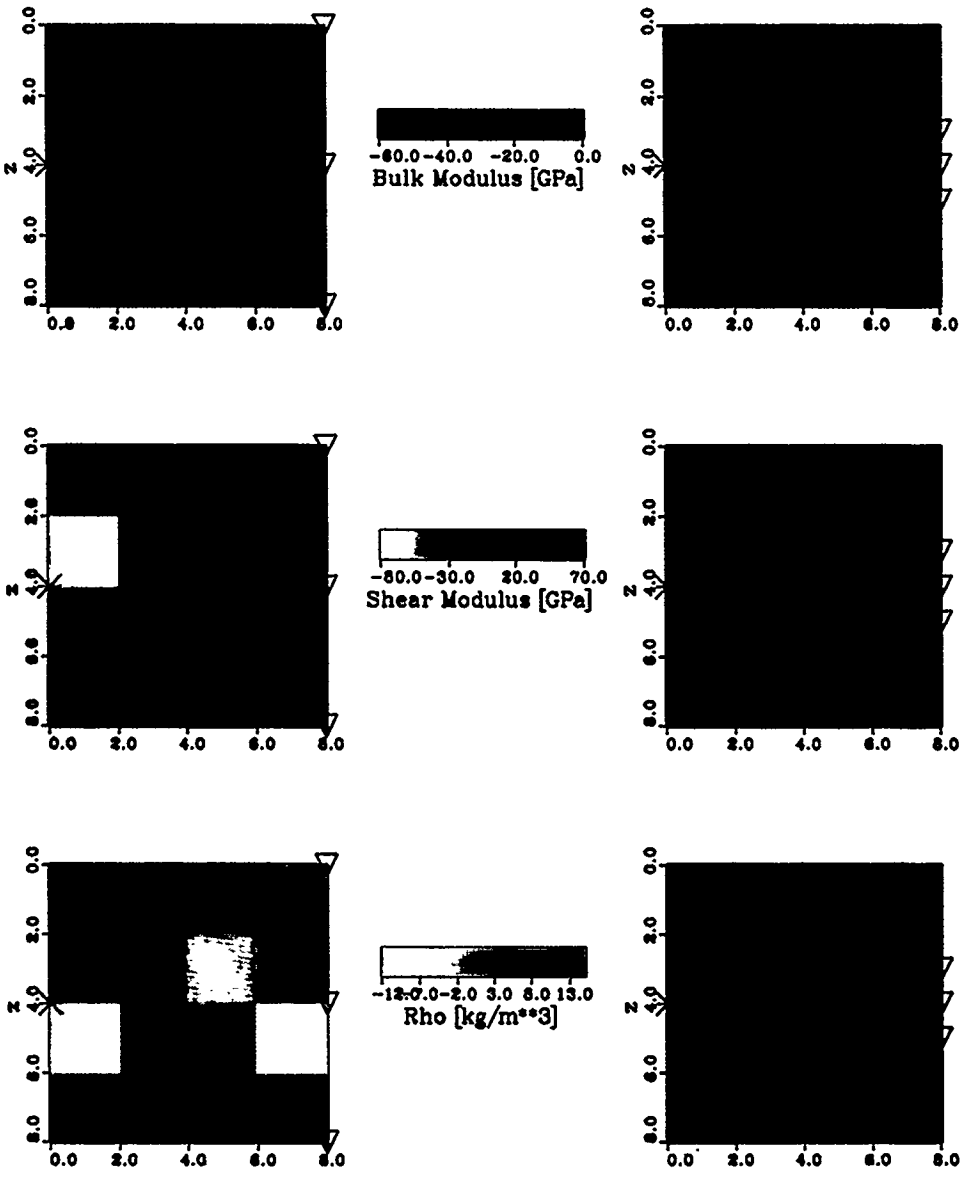

Figure 3.16: Inversion results for the real parts of the elastic parameters of the transmission survey. The notation is similar to that of Figure 3.15, except that the three groups of 5 receivers in the left panel are located at $\theta = 315°$, $\theta = 0°$ and $\theta = 45°$, whereas the group of 15 receivers in the right panel is located at $\theta = 0°$ (refer to Figure 3.12 for orientation).

can produce erroneous results no matter how well the experiment and the data processing are being conducted.

3.7 Inversion of Elastic Waves Scattered by a High Velocity Inclusion

In Chapters 3.5 and 3.6 forward modeling and inversions were performed using identical Green functions. The purpose of the present chapter is to invert synthetic data using different Green functions for both processes and to investigate the performance of the inversion process. Furthermore the effect of correlation will be studied to determine possible leakage between the parameters.

The forward modeling is based on the exact solution for the scattering of elastic waves by a sphere (Korneev et al. 1993a, 1993b), whereas the inversion uses its low frequency Rayleigh approximation. Thus the feasibility to recover an anomaly, by applying a frequency band limited approximation to invert exact broadband data, is investigated. The inhomogeneity consists of a sphere with a 10 % reduction in density relative to the background medium. As the bulk and shear modulus are kept constant, the velocities consequently are increased. The background values are taken from the example in Chapter 3.5 with $K = 37.42\ GPa$, $\mu = 27.14\ GPa$ and $\rho = 2650\ Kg/m^3$ ($V_p = 5270\ m/s$, $V_s = 3200\ m/s$), while the sphere has a density $\rho = 2385\ Kg/m^3$ ($V_p = 5555\ m/s$, $V_s = 3373\ m/s$). Based on these values it is possible to study the correlation between the parameters by inverting for the density anomaly and investigating side effects on the elastic moduli. In the ideal case, correlation should be negligible and the values for the elastic moduli should remain unchanged.

The low density sphere with a diameter of 1 m is located approximately at the center (x=5.3m, z=11.3m) of a crosshole geometry consisting of 20 sources and 20 receivers separated by an interval of $\Delta z = 1m$ each, with a horizontal separation of 10 m (refer to Figure 3.18 for orientation). Figure 3.16 displays

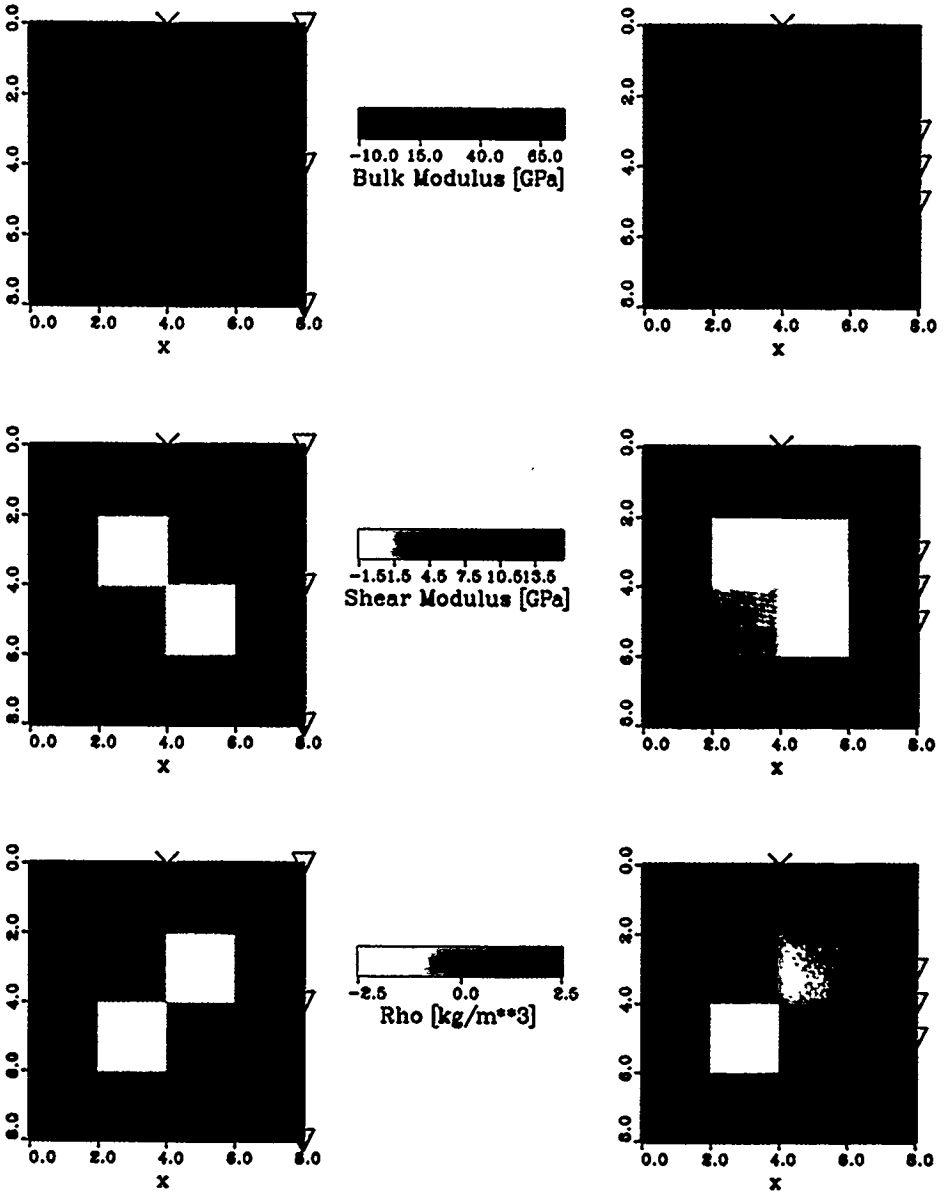

Figure 3.17: Inversion results for the real parts of the elastic parameters of the VSP survey. The notation is similar to that of Figure 3.15, except that the three groups of 5 receivers in the left panel are located at at $\theta = 225°$, $\theta = 270°$ and $\theta = 315°$, whereas the group of 15 receivers in the right panel is located at $\theta = 270°$ (refer to Figure 3.12 for orientation).

the incident wave for a source located at the center (z = 10 m) of the source gather. The x- and z-components are plotted at the top and bottom, respectively. Because of the small size of the sphere and relatively weak decrease in density only, the amplitudes of the scattered field are too small to be observable when they are displayed together with the incident field. Furthermore, the travel time differences between the two wavefields are so small that their phases cannot be separated. Thus the scattered field is plotted in a separate seismogram section, displayed in Figure 3.17. It can be seen that even for the example of a single sphere in a homogeneous medium the scattered wavefield is of complicated nature. Two major wave groups can be seen. The first represents P to P scattered phases, visible in trace 1 in the time window between t = 3.0 ms and t = 3.5 ms, while the second denotes P to S scattering which appears between t = 4.3 ms and t = 4.8 ms. In the first group several arrivals can be seen. The first pulse is the $P_2\ P_2$ phase which is reflected by the sphere. The indices denote the medium in which the waves propagate. The second pulse is a superposition of two phases that arrive almost simultaneously. These are the $P_2\ P_1\ P_2$ and $P_2\ \hat{P}_1\ P_2$ phase. The first propagates through the sphere, while the second is diffracted on the inside of the sphere propagating with the P wave velocity of the sphere. The second wave group represents the same travel paths with the exception that the waves convert to S waves while being scattered from the sphere towards the receivers. Thus they represent $P_2\ S_2$, $P_2\ P_1\ S_2$, and $P_2\ \hat{P}_1\ S_2$ for the first, second, and third arrival, respectively.

The stronger amplitudes of the incident over the scattered field by a factor of more than 10^3 prevented the inversion for the structure of the inhomogeneity without removing the incident field first. The large amplitudes of the incident field produce numerical noise that is much stronger than the signal of the scattered wavefield and hence a coherent image of the inhomogeneity cannot be reconstructed. The incident field is generated by a second set of numerical simulations using the same geometry and elastic parameters for a homogeneous background without the inhomogeneity. The incident field subsequently is subtracted from the total field and the remaining scattered wavefield is used in the

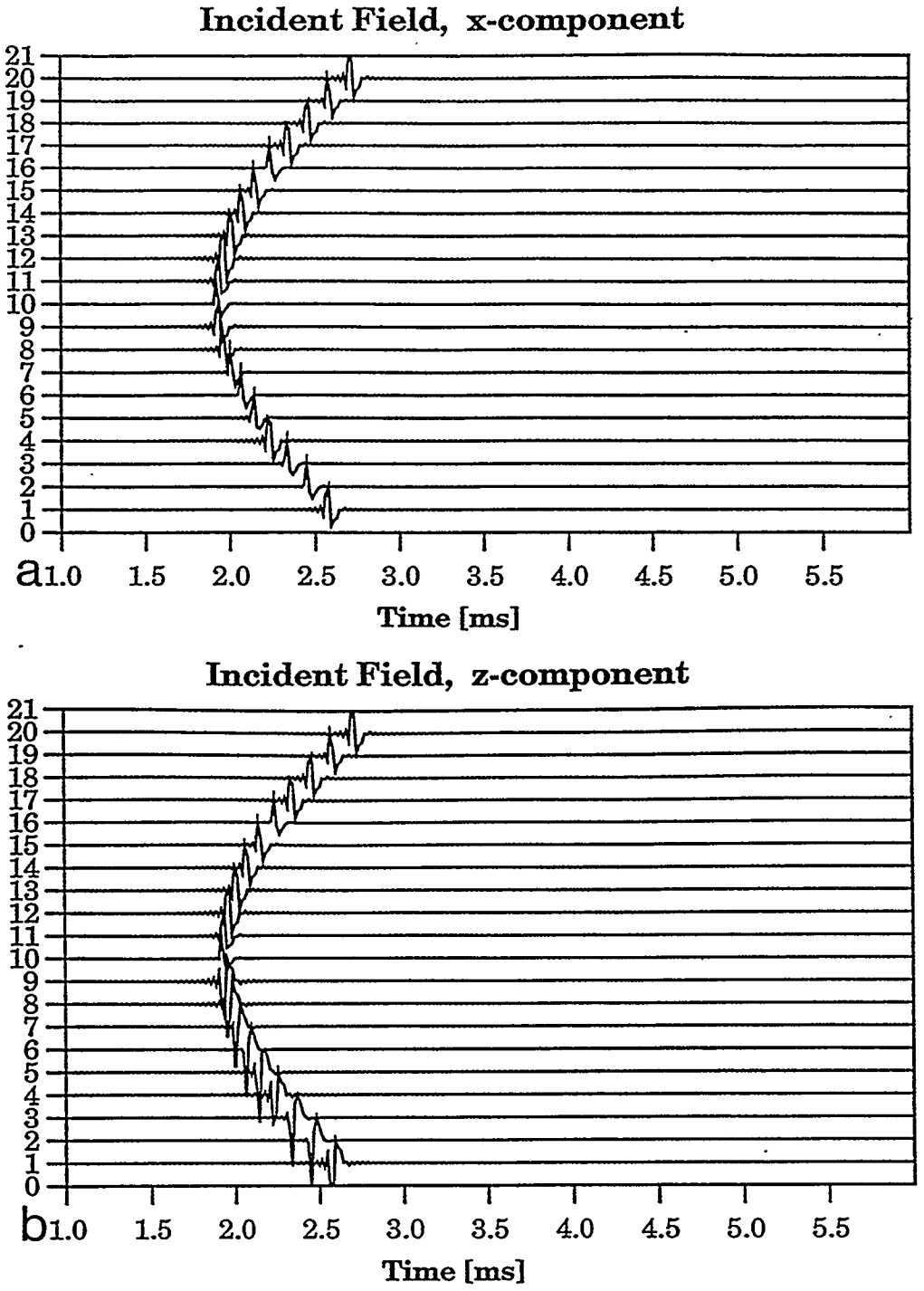

Figure 3.18: Incident field for the source position at $z = 10m$; a) x-component, b) z-component.

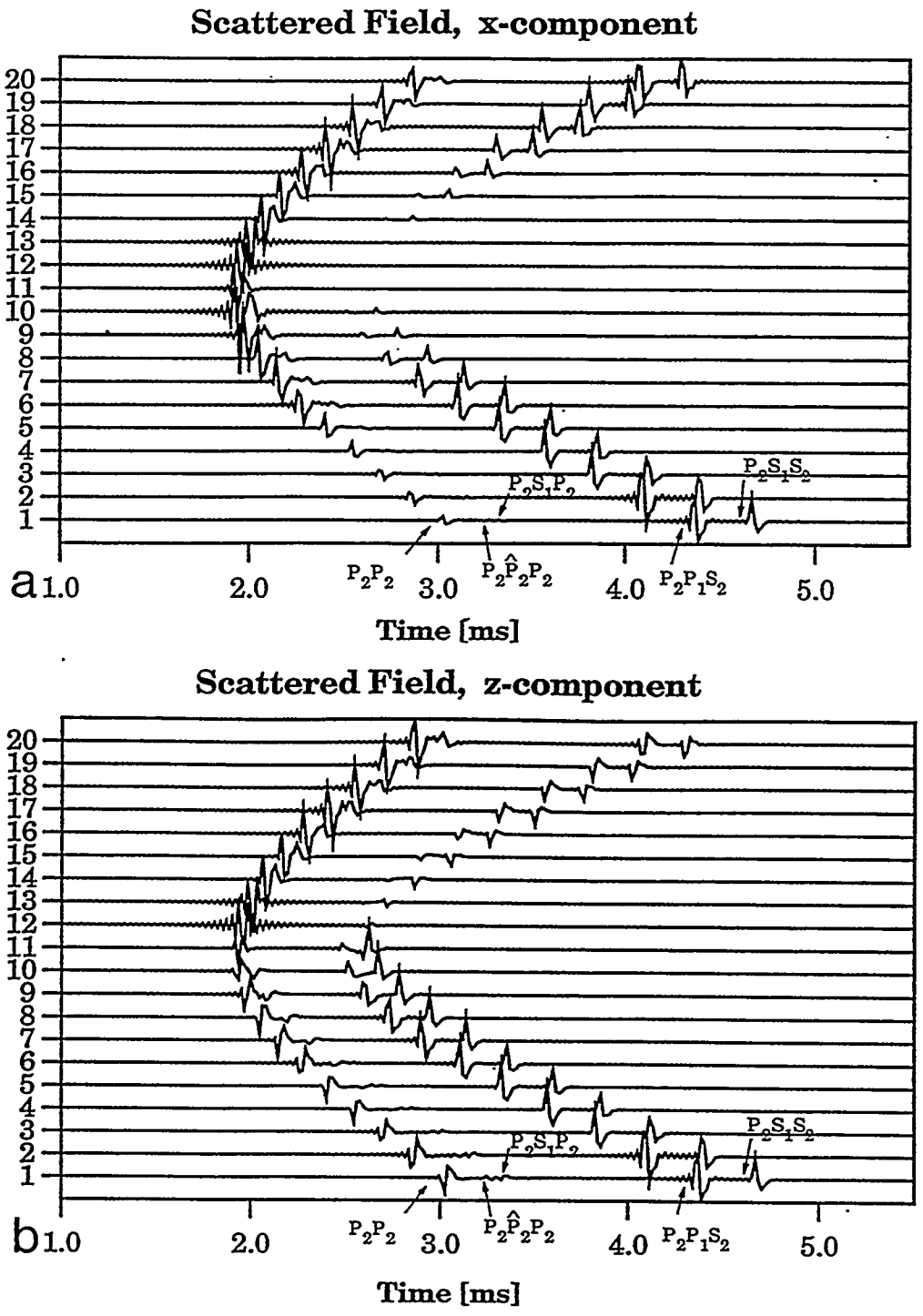

Figure 3.19: Scattered field for the source position at $z = 10m$; a) x-component, b) z-component.

present inversion attempt.

The area to be inverted for consists of 13 x 20 voxels with a side length of 1 m each (Figure 3.18). As before, sources and receivers are denoted by stars and triangles, respectively. The parametrization is extended beyond source and receiver positions to investigate whether scattered waves are being mapped into these locations. The results of the inversion is split into three panels, with bulk modulus, shear modulus, and density plotting at the top, in the middle, and at the bottom, respectively (Figure 3.18). The inversions are computed for a total of 25 frequencies and the results stacked. The frequencies vary from 122 Hz to 5981 Hz. Considering a background velocity of $V_p = 5270m/s$, this translates to wavelengths between $\lambda = 43.2m$ and $\lambda = 0.88m$ for the incident wave, and Rayleigh limits between $k_pR = 0.07$ and $k_pR = 3.56$, respectively. Thus, the wavelength of the incident wave spans the whole range from Rayleigh to Mie scattering. Although the results for the single frequency inversions vary, the averaging process is successful in recovering the density perturbation. It can be seen that for most of the voxels the background values for the three parameters are well recovered. This result can be extended to the source and receiver regions which indicates that no amplitudes are mapped into these positions and the inversion produced stable results. The density reveals a negative deviation from the background value at the approximate position of the sphere. However, the exact location of the sphere is at x = 5.3 m and z = 11.3 m, whereas each voxel of the parametrization is centered around values with 0.5 m spacing. Therefore, the inhomogeneity is parametrized by the four neighboring voxels at (x=4.5m, z=10.5m), (x=5.5m, z=10.5m), (x=4.5m, z=11.5m), and (x=1.5m, z=11.5m), with most of its volume residing in the voxel at (x=5.5m, z=11.5m). Accordingly, the inversion result the strongest deviation in this voxel. Since the returned value of the inversion is a function of the product of the deviation from the background value times the scatterer volume, the deviation in the density in voxel (x=5.5m, z=11.5m) has to be less than the original 10 %, as it parametrizes the scatterer only by a fraction. Therefore, the adjacent voxel at (x=4.5m, z=11.5m) reveals some deviation in density that comprises part of

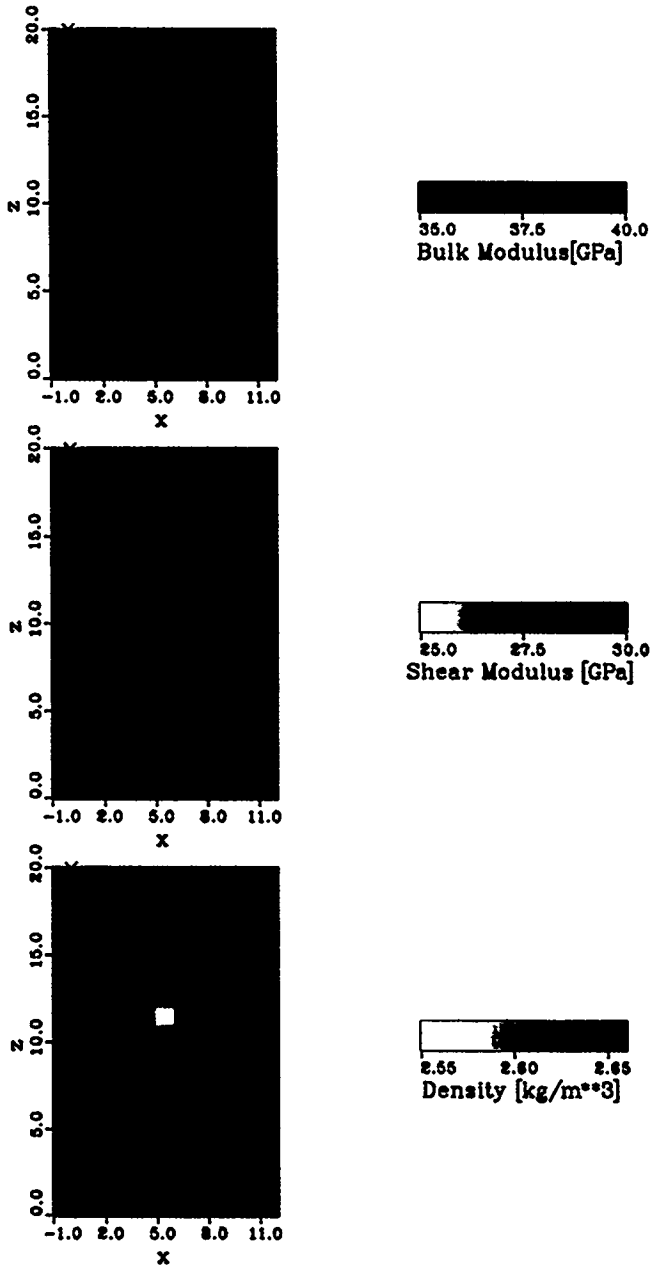

Figure 3.20: Inversion result of the scattered wavefield for the elastic moduli and the density.

the scatterer as well.

Taking the location of the scatterer into consideration, it becomes evident that the most noise in the images of the bulk and shear modulus appears around that particular position. This is caused by correlation between the density and the elastic moduli based on the parametrization of the medium. Figure 3.19 shows the correlation between the value of the density in voxel (x=5.5m, z=11.5m) and the surrounding voxels of the model for each model parameter. The top panel shows the correlation between the density and the bulk modulus, the middle panel the correlation between density and shear modulus, while the bottom part reveals the correlation of the density with itself. The values range from -1 (anticorrelation) to +1 (perfect correlation). As expected, the auto-correlation of the density value at voxel (x=5.5m, z=11.5m) is unity (bottom panel of Figure 3.19), while the neighboring elements surrounding this voxel reveal a correlation of -0.1. The correlation decreases farther away from the object revealing mean background values of 0.0029. The top panel shows a negative correlation of -0.4 between the density and the bulk modulus at the same location. As expected, this correlation amplifies the noise in this region and produces the weak anomaly apparent in the top panel of Figure 3.18. However, the background correlation reveals a very low value of 0.0017. Similarly, the correlation between the density and the shear modulus (middle panel of Figure 3.19) reveals a high value of +0.8 at the location of the object, and amplifies the noise in this area (middle panel of Figure 3.18). The mean background correlation between density and shear modulus is equally low at -0.0017. The overall low mean background value for the correlation means that little energy is smeared from the voxel of the inhomogeneity to neighboring pixels and indicates that the parametrization resolves the model well.

3.8 Conclusion

The thesis of this chapter was to reformulate the nonlinear scattering problem in terms of a direct linear solution and to invert this solution for the elastic

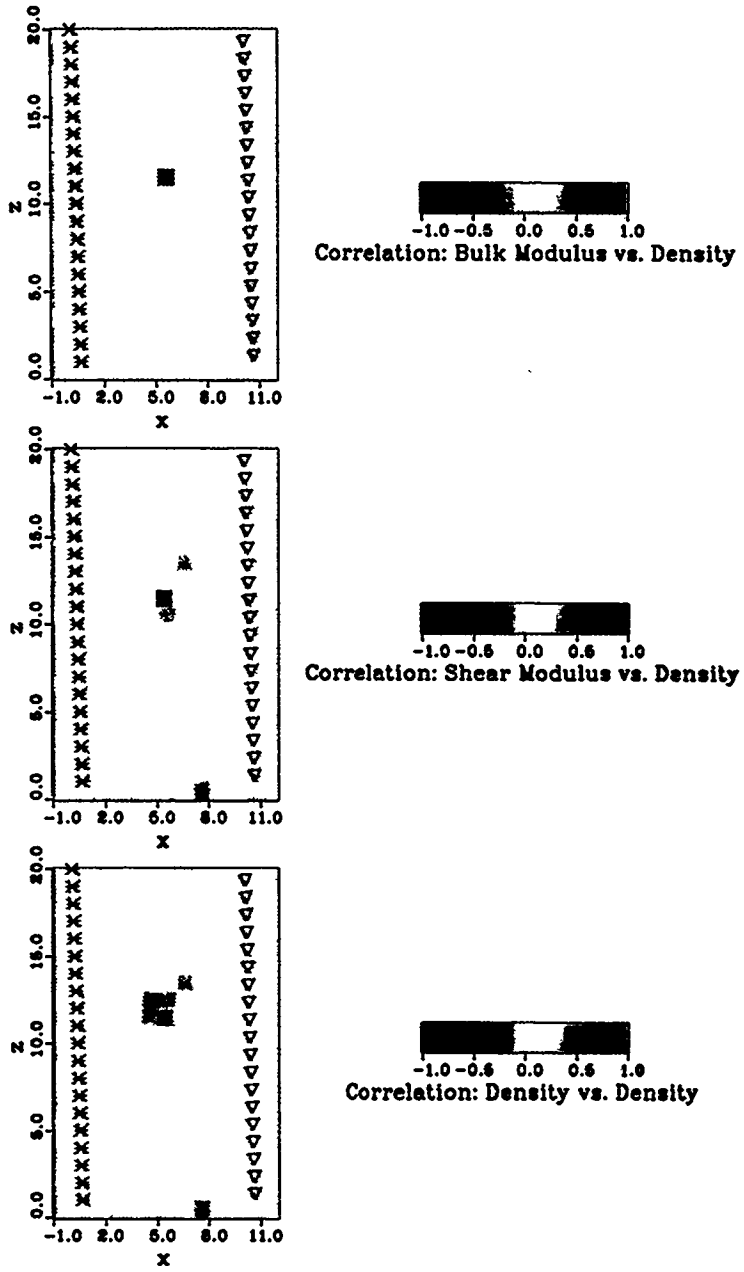

Figure 3.21: Correlation between the density value at voxel ($x = 5.5m, z = 11.5m$) and the model parameters. Top: Correlation between the density and the bulk modulus, Center: Correlation between the density and the shear modulus, Bottom: Correlation among the density values.

parameters of the medium. The inversion was investigated to determine the need for near field terms in certain cross hole situations, the resolving power of several source receiver geometries, the performance in the case of strong inhomogeneities, and the correlation between model parameters.

Reformulating the expression of the scattered field in terms of moments m_K, m_μ, and m_ρ represents a decomposition of the excitation mechanism of the scatterer and has several advantages. The scattered field and the elastic parameters depend linearly on the moments, and therefore, it is possible to solve for the moments first which subsequently can be used to determine the elastic parameters of the medium. This substitution stabilizes the inversion process, as the moments are unitless properties of equal magnitude. Further, strong inhomogeneities can be easily inverted for by solving the equations directly, without having to iterate based on a linearized approximation, derived for weak scatting cases. In most cases the linerized applications fail to produce reliable results for deviations larger than 20 % (compare to Chapter 2.4).

The nonlinear dependence of the deviation of the elastic parameters on the moments reveals that deviations between - 50 % and + 100 % exhibit the strongest nonlinearity, whereas extreme or negative deviations can be approximated by a linear fit but with almost no change in the moments for negative deviations in the elastic parameters. As a consequence it may not be possible to distinguish between a cavity and a solid inhomogeneity with small values in the elastic parameters.

The SVD was selected to invert the matrix system of linear equations as it provides a valuable insight into the physics of the problem. The decomposition into singular values allows the degree of independence among equations in the matrix system to be studied. Equations that are almost linearly dependent produce small singular values that cause instabilities during the inversion and therefore need to be set to zero. An automatic technique was chosen to damp the system, by minimizing the distance between the origin and the trade-off curve. The damping was achieved by progressively setting small singular values and their associated eigenvectors equal to zero until the resulting resolution and

variance produce an optimum value on the trade-off curve. This damping value is found to produce the best result in terms of a trade-off between resolution and variance of the parameters.

The numerical modeling of an underground crosshole situation revealed that in the absence of noise, it is possible to invert Rayleigh scattered waves to solve for the elastic parameters of the medium. It was shown that although the size of a single voxel is small compared to the wavelength, its value was successfully retrieved. As indicated in Chapter 2.3, it was shown that near field terms are important in a crosshole situation when the Rayleigh approximation is used to linearize the scattering problem. The long wavelengths cause the receivers to lie within a distance of 2 λ from the inhomogeneity and near field terms become necessary to produce correct results. Although the model resolution produced by the Green function containing only far field terms reveals an acceptable result, the amplitudes of the elastic parameters deviate from the true model by up to 2 orders of magnitude, and thus may lead to erroneous interpretations. The importance of a good source receiver geometry was presented by adding 2 receivers at selected positions which increased the angular coverage of the model area. This produces equations that are less linearly dependent and therefore add new information to the system. Adding two receivers to an existing array of 10 sources and 10 receivers improved the model resolution in the least resolved areas from 0.6 to 0.9.

The 3-dimensional scattering of energy is a complicated process almost impossible to visualize, as it depends on many parameters. An important factor are the elastic parameters of the medium, and therefore the scattering process strongly depends on the object under investigation and needs to be studied to determine the best geometry for a successful inversion experiment. It was shown for the case of a cavity that a reflection survey provides the most promising geometry, as most of the energy is back scattered. In contrast, the commonly used cross hole geometry proved unsuccessful as the cavity blocks the propagation of most of the waves and little energy is forward scattered. However, the successful result for the reflection survey indicates that the presented theory is applicable

to strong scattering objects.

The numerical case of elastic wave scattering by a high velocity (low density) inclusion was intended to invert data generated with different Green functions and to investigate the influence of the incident field on the inversion. The forward modeling was performed using an analytic solution for the scattering by a sphere, and thus the wavefield was exact over a broad frequency range. The intention was to invert this data set applying the low frequency Rayleigh approximation and to investigate whether it is possible to recover the anomaly within the limited frequency range of the approximation. It was shown that in the case of a small weak inhomogeneity, the incident field has much larger amplitudes than the scattered field and that the travel time difference, due to the small scatterer size, is not observable. Therefore, the incident wave field has to be removed before a successful inversion can be achieved, as the noise in the inversion produced by the incident field dominates over the amplitudes of the anomaly. However, in a field situation, where the incident field generally is poorly constrained, the removal would be problematic, due to interference as the fields almost coincide in time. After removing the incident field in the numerical example, the inversion of the remaining scattered field produced correct results in retrieving the anomaly. An increase in the noise level for the bulk and shear modulus at the location of the anomaly could be explained by increased correlation between the density and the moduli at this location, whereas small background values of the correlation indicate a stable parametrization of the model. This example showed that a successful inversion can be performed on broadband data by applying a low frequency approximation, as long as the incident field can be subtracted from the total wavefield. However, it should be noted that the frequencies applied for the inversion varied from Rayleigh to Mie scattering. Although this appears to be in violation with the strict mathematical application, the stacking process produces a good estimate of the results in terms of resolution of small scale features and in recovering their amplitude anomaly.

The problem of a strong incident wavefield that dominates the recorded data

and its influence on the inversion will be addressed in the next chapter for the case of a field experiment to determine the elastic moduli of a fractured zone in a granitic host rock.

Chapter 4

Inversion of Scattered Waves Applied to a Crosshole Experiment

4.1 Introduction

The last chapter was concerned with the the investigation of the effect of near field terms on the inversion result, as well as the effect of source receiver geometries. Although this is a valuable educational exercise for planing future surveys, the usual strategy to recover anomalies on a small scale is still a crosshole survey with source and receivers in opposite boreholes and the object located in between. The objects vary widely and the survey intentions range from the location and estimation of the volume, e.g for the case of a cavity, to the delineation and possible estimation of elastic or hydrologic parameters for the case of a fractured zone. In the present example, it will be attempted to invert a crosshole data set to determine the location and, if possible, the elastic parameters of a fractured zone. The intention is to study the possibility of modeling a large object by a series of small point scatterers.

A brief overview will be given to describe the experimental design and the geology at the survey site. Transmission crosshole data contain a variety of direct, scattered, and reflected phases that need to be extracted from the data before the scattered waveforms can be inverted. It will be shown what parameters have to be taken into account and whether it is possible to successfully remove unwanted phases. The results of the inversion will be presented based on images of the elastic moduli, the density, as well as the velocities, and it

will be discussed which parameters are suitable for the various objects encountered in subsurface imaging. Finally, an overview will be presented to suggest improvements for the future application of this inversion technique.

4.2 Geology and Experimental Design at the Grimsel FRI Test Site

The United States Department of Energy (DOE) and the Swiss Cooperation for the Storage of Nuclear Waste (NAGRA) conducted several experiments to investigate the effect of fractures on the storage of nuclear waste in underground repositories. The experiment was carried out at the Grimsel test site in Switzerland, with the primary goal to determine the nature of wave propagation in fractured rocks and to relate seismological to hydrological parameters. The experiment described here was carried out at the FRI site with the intention to delineate and determine the elastic parameters of a known fracture zone in a highly foliated granitic host rock. The geometry of the FRI site is shown in Figure 4.1. Two main access tunnels provide access to a zone of fracturing striking NE-SW. The zone appears to be an area with varying concentration of thin fractures, determined from cores taken from two horizontal boreholes (BOFR 87.001 and BOFR 87.002) as indicated by the short lines along the holes in Figure 4.1. In addition to the mapped fractures, a change in color of the granodiorite may indicate an additional feature in the upper half of the panel, indicated by the dashed line. The data were collected between the two boreholes BOFR 87.001 and BOFR 87.002, with 39 sources located in the first and 39 receivers in the second hole, respectively, separated by a distance of 10 m (Figure 4.2). During the experiment, the horizontal holes were water filled to improve the source and receiver coupling. Additionally, the receiver, a 3-component geophone, was clamped to the borehole wall. Although the setup reveals a typical 2-dimensional crosswell geometry, the fracture zone can be expected to extend in both directions perpendicular to the plane. Therefore, scattering in the third

dimension will have an effect on this experiment and is a possible explanation for relatively large amplitudes recorded on the y-component.

4.3 Data Processing

Figure 4.3 shows a typical source gather for a source located at $z = 1.35m$ in borehole BOFR 87.001. The reverberative nature of the incident wave is apparent behind the first arrival, and is caused by multiple reflection in the water filled boreholes. Several faint arrivals, representing reflections off tunnel walls, S waves radiated at an angle of 45° by the source, and tube waves appear in the section after $t = 5.5ms$.

The theory of the presented inversion approach is formulated for the scattered wavefield only, which requires the elimination of the incident wavefield from the recorded data. However, the reverberations in the present example make it difficult to correctly estimate the incident wave and remove it from the data. In addition to the incident field, the data are contaminated by the radiation pattern of the source, the source and receiver coupling to the borehole, and anelastic attenuation in the medium which need to be corrected for before an inversion can be attempted.

To correct for the differences in energy radiation of the source, a cosine operator ($cos\Theta$) is applied, where Θ is the angle between the horizontal and the source receiver direction. This operator was found by estimating the amplitude of the first arrival (after correcting for geometrical spreading and preliminary anelastic attenuation) while the receivers were moved in a crosshole fashion around a fixed source in a homogeneous region of the host rock. The cosine function was found to best fit the amplitude pattern (Majer et al., 1990). In a similar experiment, the P wave velocity was determined as a function of direction of propagation. The granitic rock shows a high level of foliation, parallel to the strike of the fracture zone. This foliation produces P wave anisotropy which reaches up to 8 %, with the symmetry axis normal to the plane of fracturing. Hence, the fast direction is parallel, and the slow direction perpendicular to the

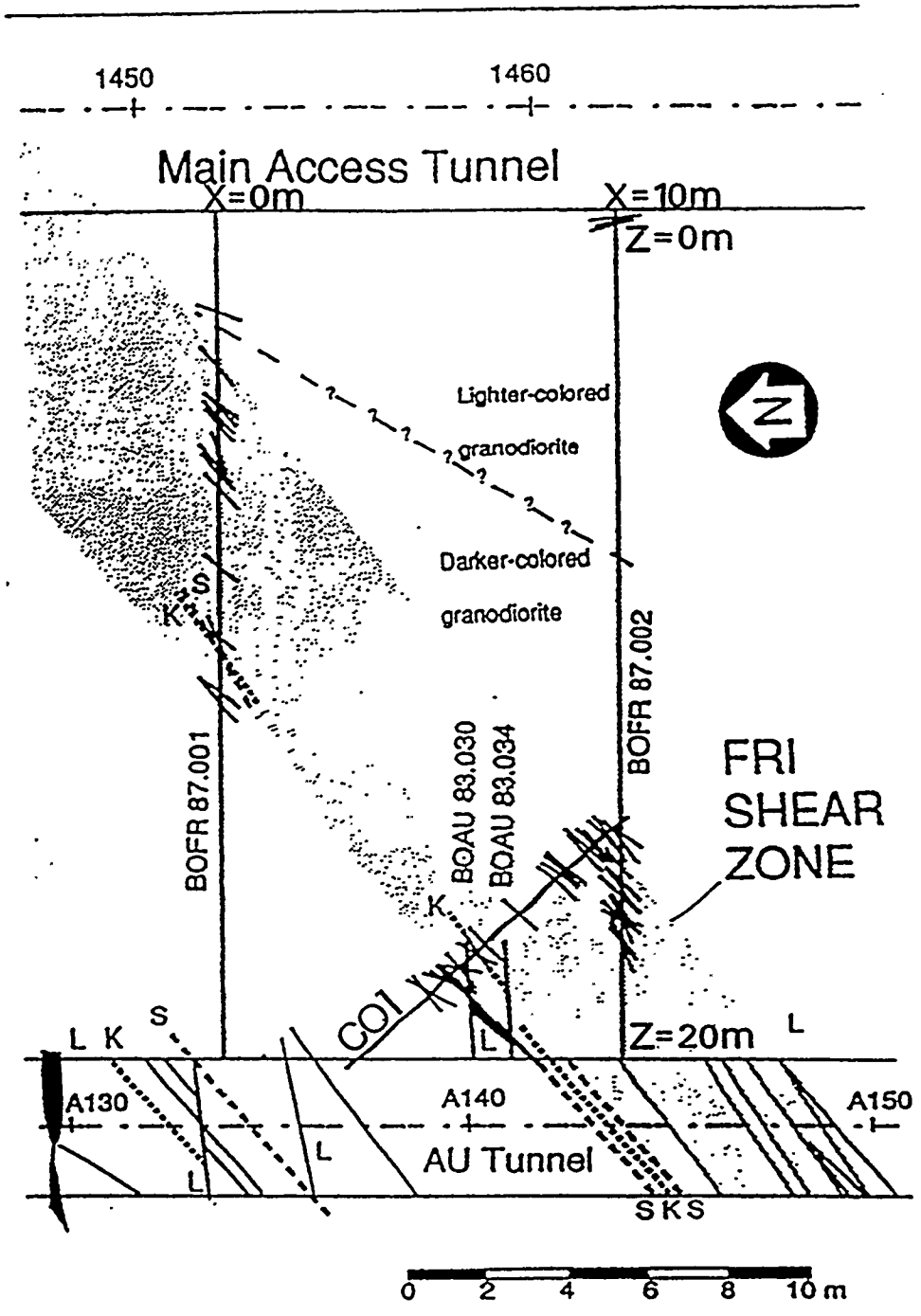

Figure 4.1: Experimental design and geology at the Grimsel FRI site.

Source and Receiver Locations at the FRI Site

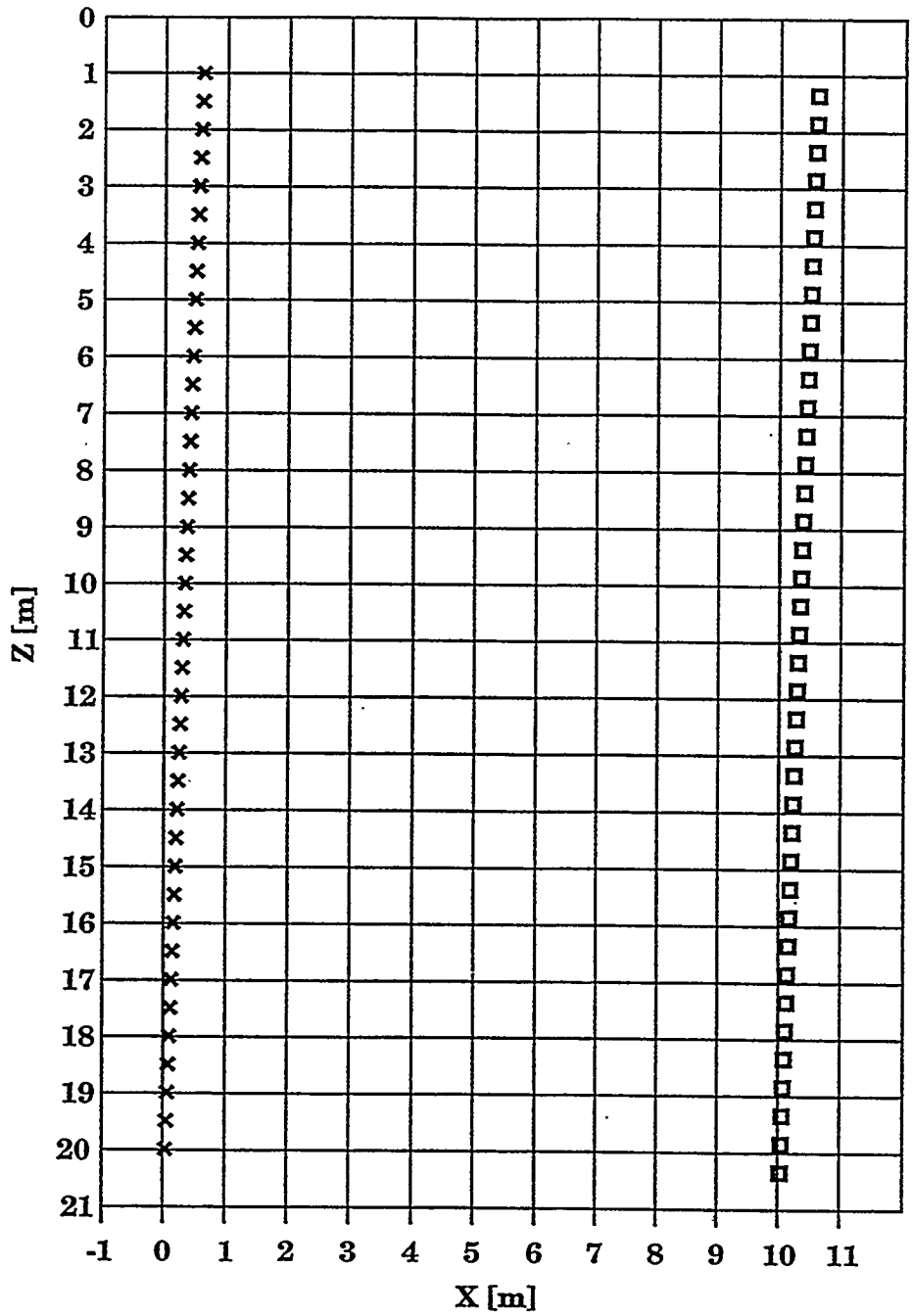

Figure 4.2: Geometry of the field experiment. Sources and receivers are denoted by stars and squares, respectively. The source borehole on the left corresponds to BOFR 87.001 in Figure 4.1, while the receiver hole is represented by BOFR 87.002.

strike of the fracture zone. The average background velocity was determined at $5270m/s$. Although no anisotropy estimation was done for the S wave velocity, the background value was determined at $V_s = 3200m/s$. It is expected, however, that the host rock reveals a similar degree of S wave anisotropy, the lack of which will reduce the quality of the inversion results, as a considerable amount of scattered energy is converted into S waves.

To estimate the mean anelastic background attenuation α and the factors governing the source receiver coupling at their locations in the boreholes, the amplitudes of the first arrivals were measured and the parameters estimated in a least squares sense. The parameters have to be determined simultaneously, as they have similar effects on the amplitude of the wavefield, and an inversion of a single parameter is not possible without estimating the others first. The wavefield is corrected for geometrical spreading and the radiation of the source. Subsequently, the traces are aligned along their arrival times and the amplitudes of the first minima determined. A total of 1521 amplitude values were inverted to solve for the 79 unknowns (39 source and receiver parameters each and the average background deviation α). The background attenuation is estimated to be $\alpha = 0.36m^{-1}$. Assuming a linear frequency dependence for α, a background velocity of $V_p = 5270m/s$, and a peak frequency dominating the incident pulse of $f_0 = 10KHz$, the relation $Q = \pi f/\alpha V_p$ produces a frequency independent quality factor of $Q = 17$. The value for α, although it seems to be low, is not unreasonable for this highly foliated medium considering the short wavelength of 0.53 m of the incident pulse. It is representative of the mean background attenuation, however, and does not take into account local areas of abnormal attenuation.

The results for the normalized source and receiver coupling factors are presented in Figure 4.4. It can be seen that the source factors vary around the value of 1.0 with larger deviations between source position 10 to 20, corresponding to $z = 5m$ to $z = 10m$, respectively. Referring to Figure 4.1 it becomes obvious that this is the range where the assumed fracture zone intersects borehole BOFR 87.001. As the factors are larger than unity towards the edges but less

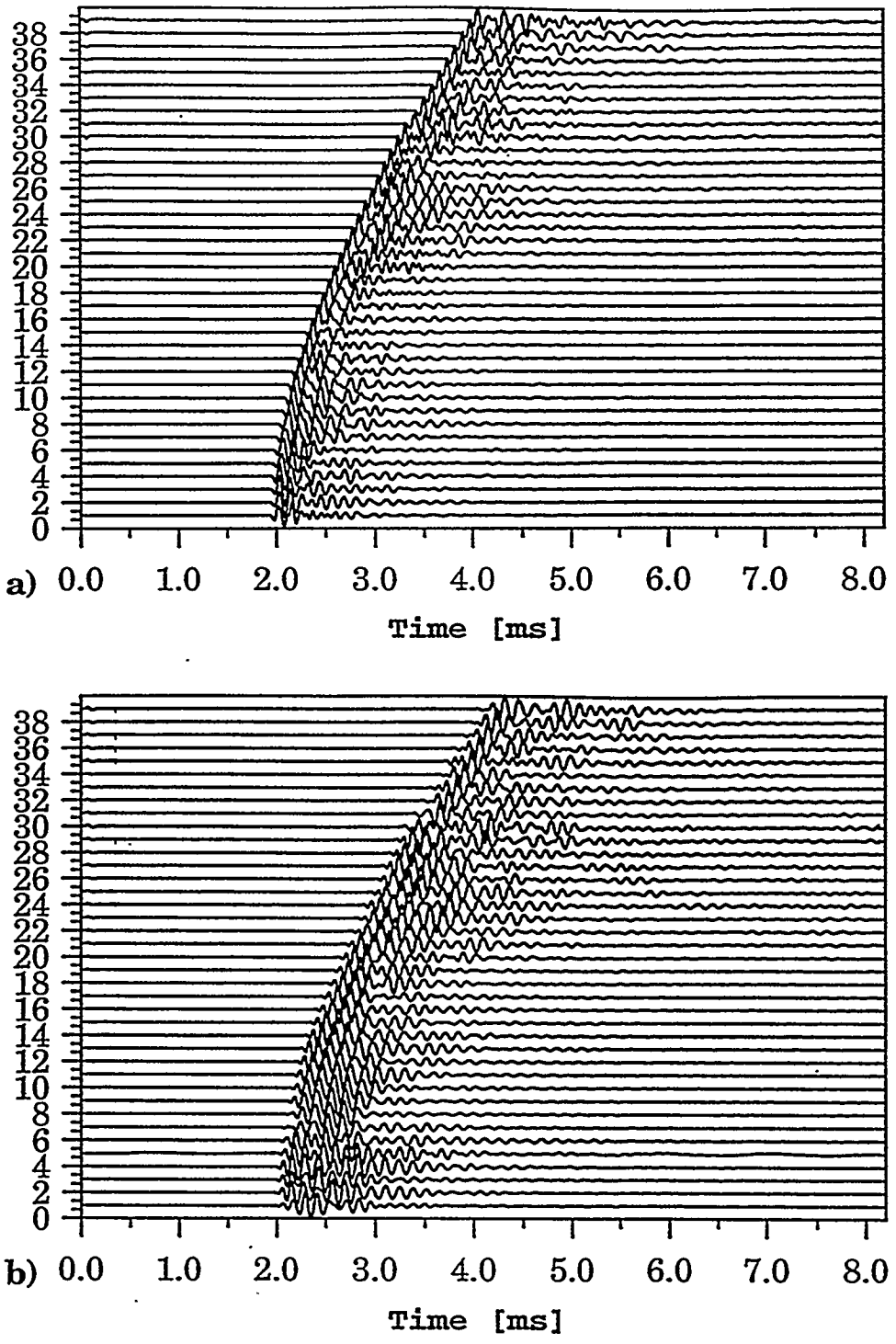

Figure 4.3: Source gather of total wavefield for source location $z = 1.35m$, a) x-component, b) z-component.

than unity in the center of the fracture zone, the physical parameters may be varying across the fault area, indicating that, in fact, this is not a homogeneous fracture, but rather an accumulation of thin parallel cracks. The trend for the receiver factors differs but supports the geological interpretation. A monotonous increase from values around 0.5 to 1.0 between receiver position 1 ($z = 1.5m$) and 15 ($z = 8.5m$) is evident in Figure 4.4b). The low values are too small to be explained by borehole effects only. However, since the inversion simultaneously solves for the mean value of α, but does not recover local attenuation anomalies, any anomaly will have an effect on the wavefield, particularly if these zones are close to certain receivers. Such an anomalous zone was detected by Majer et al. (1990) for a region close to borehole BOFR 87.002 between the receiver position 1 ($z = 1.5m$) and 10 ($z = 6.0m$). This result is mirrored by the low values in Figure 4.4b). Figure 4.1 shows borehole BOFR 87.002 intersecting the fracture zone at approximately ($z = 16.0m$) (receiver position 32). Again, the receiver factors reveal a maximum, before they drop to lower values towards the center of the fracture zone at the end of the borehole. Thus, the source and receiver coupling factors seem to relate to the geological features, indicating a non uniform fractured zone and possibly a high attenuation area in the SE corner of the study area.

After correcting the total wavefield for the source and receiver coupling factors and the background attenuation, the first arrivals should be a good representation of the source wavelet. Therefore, for every source position, the traces are stacked to produce a representative source signal for each source location. Finally, the 39 source wavelets are stacked to produce the common source signal representative of all source positions. This wavelet is shown in Figure 4.5. The reverberative nature is evident after the first impulse for almost $0.6ms$. However, in contrast to many traces, the amplitudes are not constant but appear to be attenuated after the first pulse. The reverberations are caused in part by multiple reflections in the receiver borehole. However, in contrast to the receiver, the source was not clamped in the borehole, as the water was intended as the coupling medium to the borehole wall. Thus, after the first source pulse,

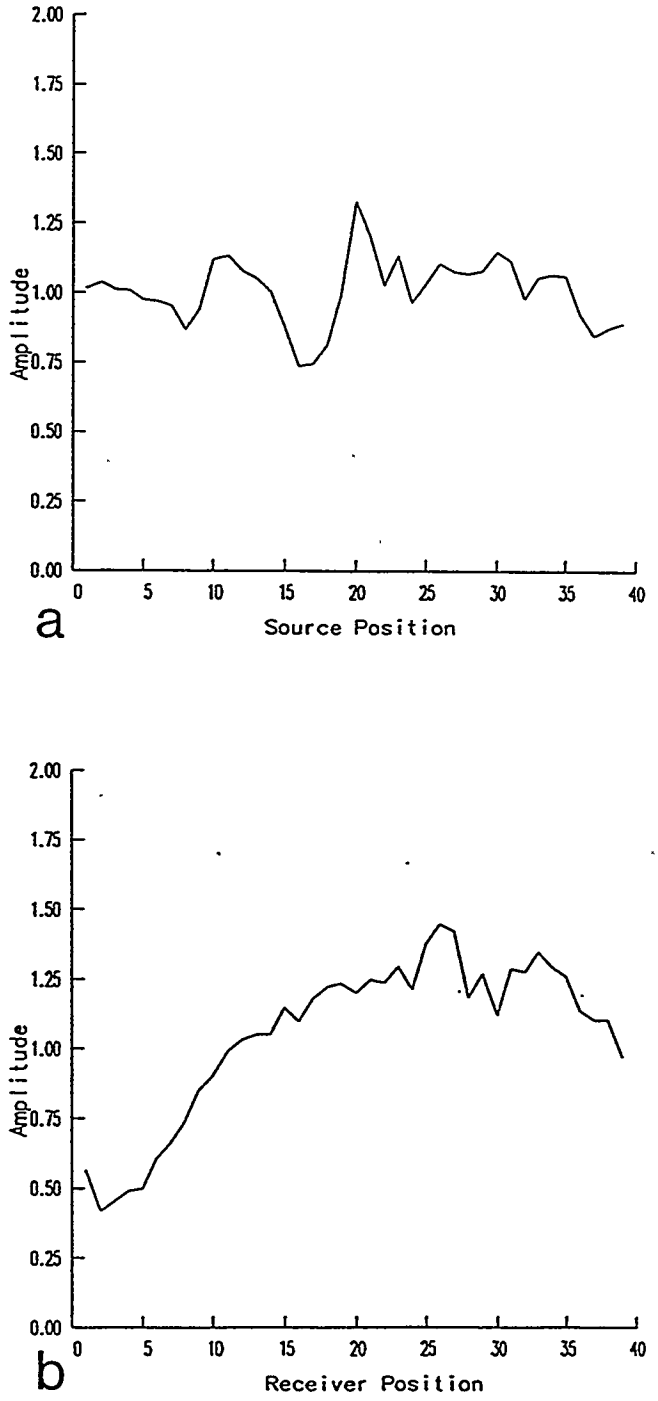

Figure 4.4: Normalized source and receiver coupling factors, a) source factors, b) receiver factors.

a fraction of the energy reverberates in the source hole and each reverberation radiates energy into the formation. Therefore, the multiples are likely to be a mixture of source and borehole reverberations. It will be discussed in a later section what length of the source wavelet provides the best deconvolution operator for the scattered wavefield.

The first $0.6ms$ (150 samples) of the source wavelet are convolved with a 3-d Green function to compute a representative incident field which should be subtracted from the total field. However, because of the large amplitudes of the reverberations in many single traces which did not stack constructively to equally large amplitudes in the source wavelet, it was not possible to remove the incident field and the reverberations effectively. Without the removal of the reverberations, however, the inversion will not produce reliable results as they produce the largest amplitudes in the seismogram after the removal of the incident field. Therefore, the incident field and the reverberations are suppressed by applying a one sided Hamming window to the beginning of the traces, to damp an interval of $0.6ms$ after the first arrival. The window length was estimated from the source wavelet in Figure 4.5, where the reverberations appear to be present up to $0.6ms$. The windowing process simultaneously damped all near field scattered phases that might have been present in the seismogram. These phases appear with little travel time separation from the incident field in the seismogram, since the scattering takes place in the vicinity of the source or the receiver. To avoid incident S waves and tube waves in the coda of the traces, visible after $5.5ms$ in Figure 4.3, the end of the traces are damped, again using a one sided Hamming window. The filtered wavefield representing the bulk of the scattered energy is shown in Figure 4.6, where the geometry of sources and receivers is the same as for Figure 4.3. The windowing process limits the scattered phases to primarily forward scattered energy.

In a final step before inversion, the scattered field has to be deconvolved by the source wavelet, to normalize the amplitudes by the source strength. In the last paragraph, it was argued that part of the reverberative nature of the source wavelet is due to reverberations in the source borehole. In this case

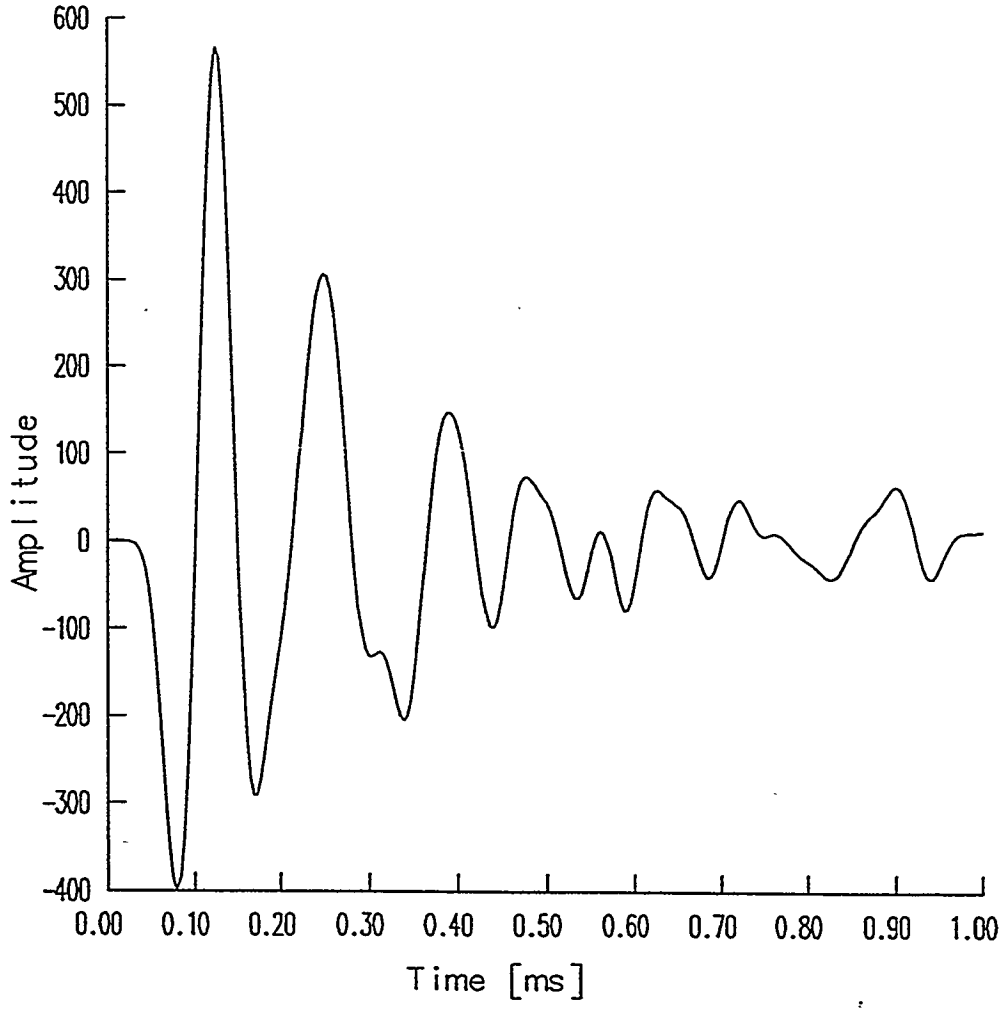

Figure 4.5: Representative source wavelet averaged over all source locations.

the borehole source acts like a pulsar pumping energy into the formation with every reverberation. This additional energy has to be taken into account for a successful deconvolution by the source signal. For this reason the length of the deconvolution operator is chosen to be $0.6msr$, after which the reverberations of the wavelet are sufficiently damped. After deconvolution, the spectral values of the scattered field are taken as input for the inversion algorithm.

4.4 Inversion of the Field Data

The images of the inversion results are compiled by stacking 13 individual inversion results, each computed for one single frequency ranging from $3051Hz$ to $5981Hz$ with an interval of $244Hz$. Assuming a background P wave velocity of $V_p = 5270m/s$, this translates to a wavelength of $\lambda_p = 1.7m$ and $\lambda_p = 0.9m$ for the incident wave, respectively. Unsing a voxel length of $1m$, the wavelengths vary from the Mie scattering range ($\lambda_p = 0.9m$) to a value of ($\lambda_p = 1.7m$) that lies between the ranges of Mie and Rayleigh scattering. The inversion was performed using lower frequencies as well, but the resulting images did not reveal sufficient resolution and therefore were dismissed from the final stack.

The inversion is computed using two criteria. First, the Green function is computed with and without P wave anisotropy in the background medium, and second, the data is inverted with and without corrections for the background attenuation The intention is to study the sensitivity of the inversion to anisotropy and to determine what effect anelastic attenuation has on the inversion result.

Figure 4.7 reveals the geometry of the area which is parametrized in the model. As indicated in Figure 4.2 the boreholes are slightly slanted with respect to the z-axis of the coordinate system. An area $9m$ x $19m$ was parametrized into 171 voxels of $1m^3$ each. Data from all 39 source and receiver positions are used. After the inversion, each panel is smoothed applying a cubic b-spline interpolation after Michelini et al. (1991), generating the final plot. The background values of the inversion are determined using the V_p and V_s values given above and a mean density of $\rho = 2650kg/m^3$ (Majer et al., 1990). This translates into

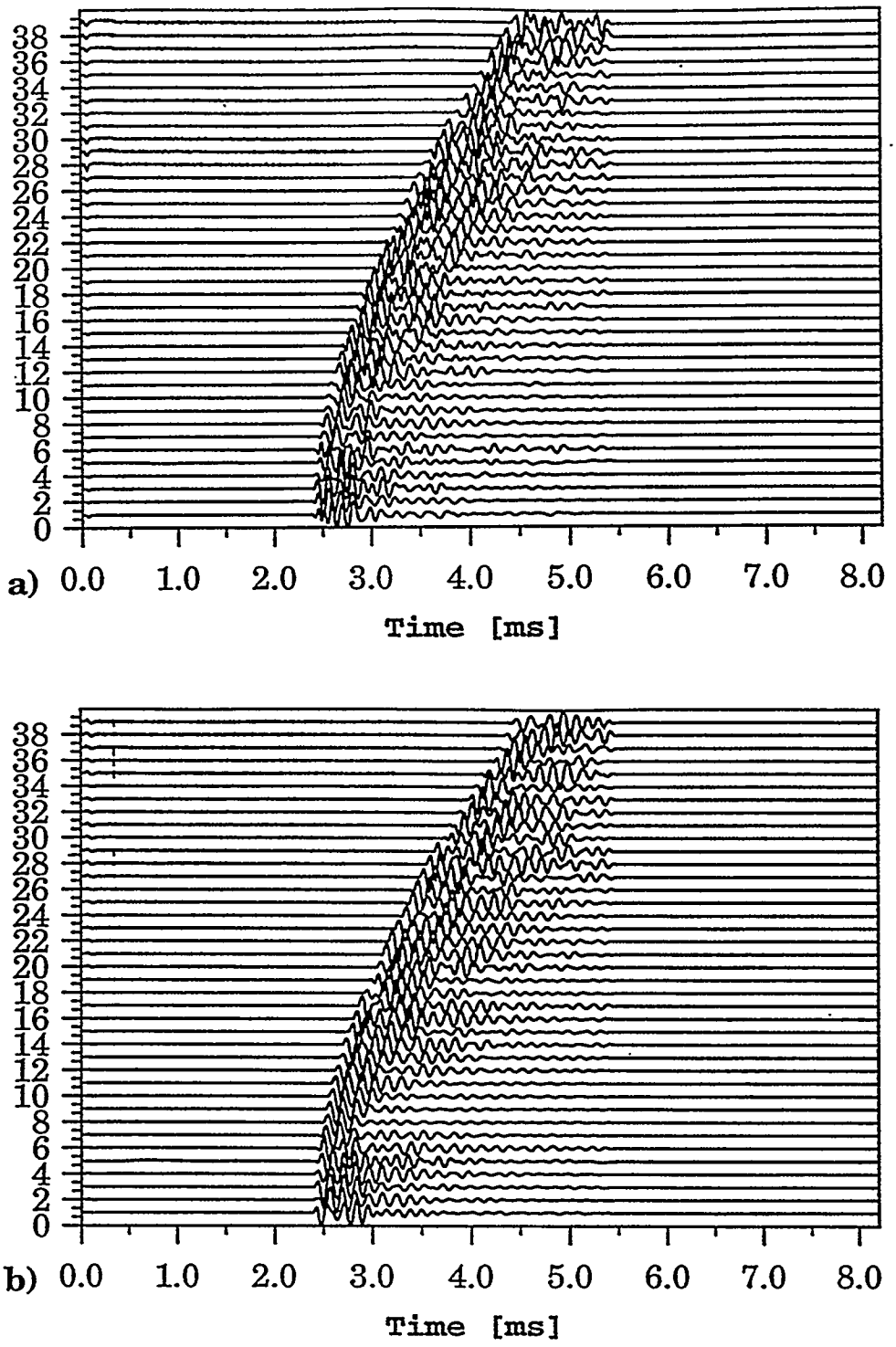

Figure 4.6: Source gather of scattered wavefield for source location at $z = 1.35m$, a) x-component, b) z-component.

a bulk and shear modulus of $32.42GPa$ and $27.14GPa$, respectively.

The inversion results in Figure 4.7 are determined by taking the P wave anisotropy into account but neglecting the correction for anelastic attenuation. Therefore, the scattered amplitudes will be more attenuated, however, since the fracture zone most likely is a zone of higher attenuation, its influence may be mirrored in the data. The image of the bulk modulus reveals several features that can be related to the inferred geological interpretation as suggested in Figure 4.1. In the bottom half of the image ($z = 13m$ – $z = 20m$) a crossing pattern of low bulk modulus anomalies can be seen. The suggested fracture zone is not clearly visible due to a more pronounced feature running from the lower left corner ($x = 2m, z = 18m$) to borehole BOFR 87.002 ($x = 10m, z = 14m$). Referring to Figure 4.1 this could be the effect of the borehole labeled CO 1 connecting the AU Tunnel with borehole BOFR 87.002. A possible explanation may be provided by the nature of the fracture zone. In contrast to a clear fracture, this zone probably consist of several thin parallel fractures with a more gradual reduction in the elastic parameters, and thus it may not reveal such a strong contrast. The borehole, however, provides a sharp contrast to the background medium and therefore constitutes a strong inhomogeneity for elastic waves; although it is not clear whether the relatively small volume of the borehole can produce such strong scattering amplitudes. A similar crossing feature of low values in bulk modulus is visible in the upper half of the panel between ($z = 2m, z = 10m$). The feature crossing from upper right ($x = 10m, z = 2m$) to borehole BOFR 87.001 at ($x = 1m, z = 10m$) is comparable in signature to a low velocity anomaly found by Majer et al. (1990) and Vasco (1995), although this is only supported by a set of fractures found at the beginning of borehole BOFR 87.002, indicated by short lines at ($x = 10m, z = 0m$). Again, a pronounced anomaly is visible striking from ($x = 10m, z = 7m$) at BOFR 87.002 upward towards the source hole ($x = 3m, z = 5m$). The interpretation could be a possible suture zone between two differently colored host rocks in the area (dashed line in Figure 4.1). An explanation could be based on the fact that this welded contact constitutes a better scatterer than the fracture zone and

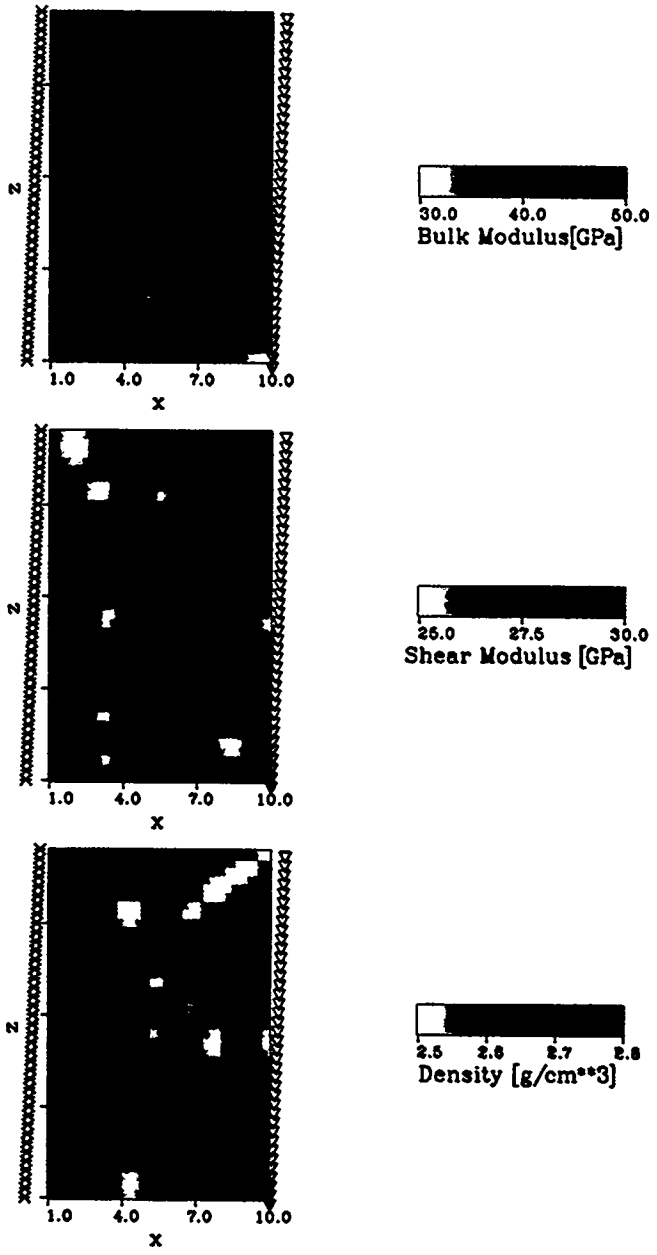

Figure 4.7: Inversion result for the elastic parameters for an anisotropic background medium. Stars denote sources, while receivers are indicated by triangles. The result represents a stack of 13 individual frequencies, ranging from $3051Hz$ to $5981Hz$.

thus produces a more pronounced feature. Side effects from the tunnel walls are not apparent, which is due to the windowing at the end of the traces. The results for the shear modulus partly support this interpretation, although they reveal the smallest perturbation of the three parameters. The fracture zone in the lower left half may be indicated by three point anomalies trending from the lower right corner to the middle of borehole BOFR 87.001. The suggested suture zone appears to be shifted relative to the position in the upper panel. However, S wave anisotropy is not accounted for in the inversion, and therefore the location of the shear modulus may be more affected than for the other parameters. The location of the bulk modulus should be well constrained as it is affected by the P waves only, whereas the density, being constrained by P and S waves, may not be as much affected by deviations in the S wave velocity as the shear modulus. The bottom panel, displaying the density data, shows a strong feature runing from the upper right corner ($x = 10m, z = 0m$) towards the middle of the panel ($x = 4m, z = 6m$). This partly supports the results of the bulk modulus for the location of the anomaly. The suture zone may be indicated by a faint anomaly traversing the upper half of the panel from ($x = 10m, z = 8m$) at borehole BOFR 87.002 towards the middle of the upper panel ($x = 7m, z = 8m$). However, the fracture zone in the bottom half is not well constrained by the density.

The results of the three parameters clearly suggest the complicated process of elastic wave scattering. Because of the limitations in the data processing, the amplitudes of the moduli are the least constrained parameters in the inversion. Similarly, the consideration of S wave anisotropy should improve the location of the anomalies of the shear modulus. However, despite these constrains it is evident that the three parameters are affected in a distinct way by the encountered geological features. It appears that the bulk modulus is more sensitive to drastic changes (e.g. borehole or welded contact) than it is to gradual changes in a zone consisting of several fractures. The density on the other hand may be sensitive to both features, whereas no real conclusion can be drawn for the shear modulus from these results. However, this suggests, as indicated in Chapter 3.1,

that the difference in response of the three parameters may lead to decreased effects in the seismic velocities.

To demonstrate this point, the P and S wave velocities as well as the V_s/V_p ratio are computed for the inversion results of Figure 4.7 and presented in Figure 4.8. As can be seen, the same parameters produce different features when displayed in terms of the velocities. The P and S wave velocities suggest the presence of a low velocity anomaly in the lower right corner of the panel, possibly indicating the fracture zone, which is known to intersect the eastern tunnel (AU Tunnel in Figure 4.1) at $(x = 8m, z = 20m)$. Similarly the presence of borehole CO 1 is indicated by a low velocity anomaly but merges with the fracture anomaly (visible in P wave velocity). The suture zone in the upper half is not visible, whereas the anomaly crossing from the upper right corner $(x = 10m, z = 0m)$ towards the middle of the panel $(x = 6m, z = 5m)$ is evident as a high velocity anomaly, due to the low values in density for the same location in Figure 4.7. Because these features are similar in P and S wave velocities, they do not produce anomalies in the V_s/V_p ration (bottom panel of Figure 4.8). The most apparent feature in the V_s/V_p ratio is what appears to be the borehole CO 1, as this anomaly produced larger negative deviations in the P wave velocity. Therefore, it is evident that the elastic moduli respond distinctively to geological features and are useful in extracting different information which can be displayed in various combinations to provide a more profound understanding of heterogeneous subsurface structures.

The inversion problem is overdetermined since all 39 source and receiver positions are used and total of 513 model parameters are inverted. Thus the model resolution is good for most of the parameters. It ranges for the shear modulus and the density from values of 0.9 along the source and receivers (due to near field terms in the Green function) to values of 0.6 in the center of the image, although the outermost row of voxels for the shear modulus reveals a resolution of only 0.2. However, for the case of the bulk modulus, the resolution is equally good at the edges but drops down to 0.45 in the center of the model. These results confirm the numerical calculations in Chapter 3.5, where a similar

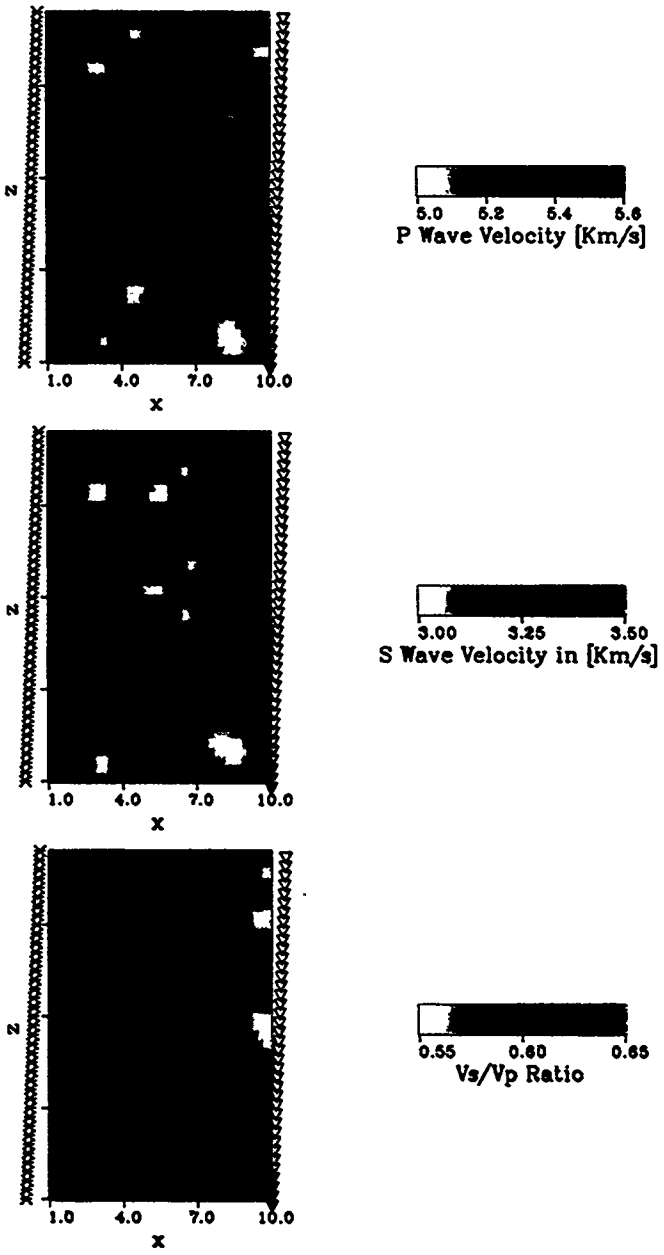

Figure 4.8: Velocity and V_s/V_p-ratio maps determined from the inversion results of Figure 4.7.

behavior in the model resolution was determined. The drop in model resolution for the bulk modulus is caused by the fact that it is only constrained by the scattered P waves, whereas shear modulus and density are determined by both, P and S waves. The drop in resolution in the center relates to the less perfect angular coverage as stated in Chapter 3.5, where the waves are more likely to sample a voxel in a straight transmission manner. Concerning the model resolution, it can be stated that most of the features in Figure 4.7 are resolved and to a certain degree independent from each other.

In contrast to Figure 4.7, Figure 4.9 shows the inversion of the same parameters for an inversion based on an isotropic background P wave velocity of $5270m/s$. It is evident, that the image does not resemble the geological features described in the previous figures. Moreover, it can be seen that the linear features have disappeared and most of the deviations reveal a block like structure. This may indicate that linear features striking either parallel or perpendicular to the symmetry axis of anisotropy can no longer be resolved using a mean background velocity. In this case the velocity in the fast direction is underestimated, while it is overestimated in the slow direction. Therefore linear features striking parallel to the fast direction is are shrunk, while features parallel to the slow direction are elongated. Thus for the case of inverting scattered amplitudes, the Green function has to account for anisotropy if linear features are to be recovered. It can be concluded that S wave anisotropy, which is not accounted for in this example due to the lack of S wave velocity measurements, can be as easily implemented as for the case of P wave anisotropy presented here. The strong amplitudes for P to S scattered waves (refer to Figure 3.12) supports this point. However, in the present example, the effect of scattered S waves may have been suppressed due to the windowing at the end of the traces, which is supported by the weak anomalies in the shear modulus. Additionally, as the wavefield is not corrected for anelastic attenuation and the inversion is done one frequency at a time, the effect is stronger for the S waves as their wavelengths are shorter and therefore they are more strongly attenuated than P waves over the same travel distance.

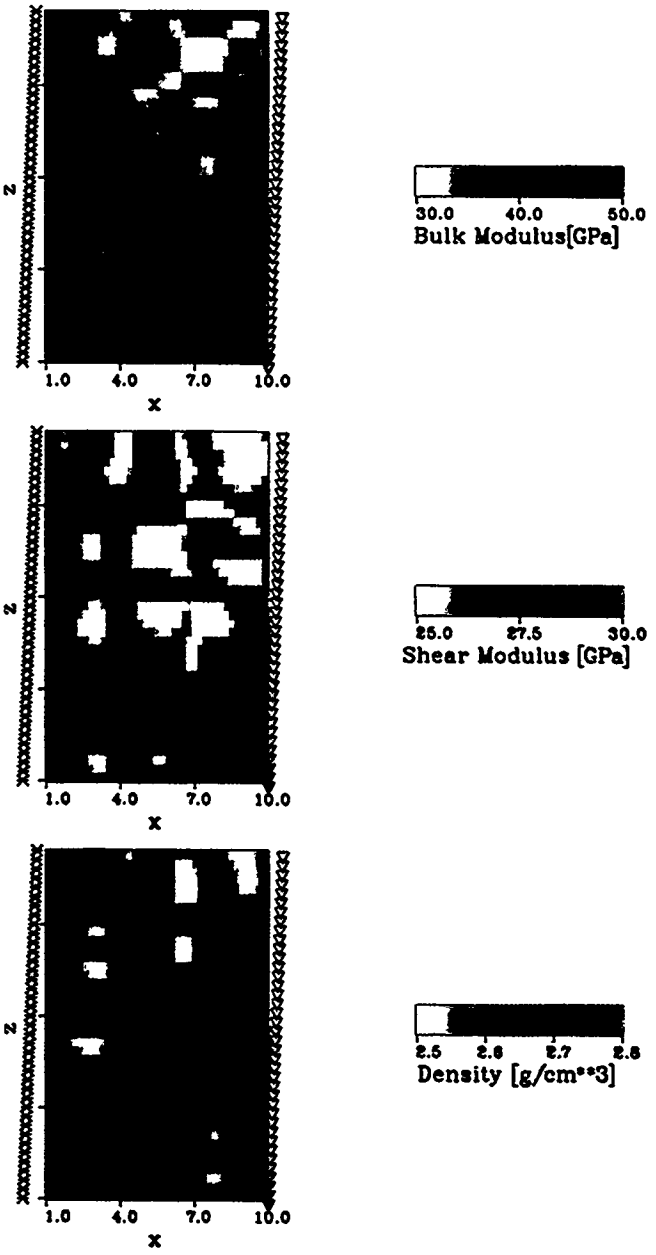

Figure 4.9: Inversion result for the elastic parameters for an isotropic background medium.

The inversions were also performed for attenuation corrected data, however, the results revealed no structure, but rather strong oscillations between high and low anomalies. This may be caused by an overcorrection for the anelastic attenuation $\alpha = 0.36m^{-1}$, as determined in Chapter 4.2. However, inversion results based on a lower value of $\alpha = 0.12m^{-1}$ as determined by Tura (1990), revealed the same problem, and therefore it seems questionable whether the extraction of α is a suitable procedure. A possible solution is suggested in the following chapter.

4.5 Conclusions

The application of inverting scattered waves to detect a fracture zone in a cross hole situation revealed the following results. Before a successful inversion is feasible the raw data have to be corrected for various effects. The source radiation pattern should be determined and corrected before any other parameters can be estimated. Source and receiver coupling to the borehole has to be estimated simultaneously with the anelastic attenuation in the medium, as all parameters have a similar effect on the first arrival and a single estimation cannot be performed without assuming values for the other parameters. The inversion produced meaningful results for the source and receiver factors, which correlate well with the geology encountered in the boreholes. It produces an indication that the fracture zone is not a homogeneous feature along the borehole wall. However, the estimation of α produced an estimate that might be too low for this host rock.

Reverberations in the source and receiver borehole made it difficult to successfully remove the incident wavefield and a robust method of windowing the beginning and the end of the traces was necessary. However, the inversion of the scattered wavefield produced reasonable results that can be related to the geology as determined from the tunnel and borehole walls. It appears that the two moduli and the density respond to different features in different ways, and therefore this may be a good method of distinguishing between e.g. an open

fracture zone and a closed welded fracture. Furthermore, the commonly used images of V_p and V_s velocities and their ratio can be easily computed to support other tomographic studies.

At this point the general finding for the FRI zone are more suggestive than definitive. It appears that the main fracture zone striking NE-SW is an accumulation of several thin fractures producing a blurred image. In contrast an additional zone striking SE-NW from the Main Access Tunnel to borehole BOFR 87.001 seems to be a more narrowly defined feature. In addition, the existence of a welded contact between the two differently colored host rocks appears to be real at about the location indicated on the map in Figure 4.1. However, the quality of the image, although the findings appear significant, is limited. This can be explained by a variety of factors summarized in the following paragraph.

The fracture zone is embedded in a relatively homogeneous granite and it can be expected that it extends to both sides perpendicular to the experimental plane. Thus out of plane scattered amplitudes will be evident in the seismogram traces, which will contribute to an overestimation of the parameters to be determined in the plane. A possible test would be to invert for a 3-dimensional medium consisting of 3 planes parallel to each other extending in the y-direction. Thus out of plane scattering could be traced back to its origin and the image could be improved. However, sufficient source and receiver coverage is necessary. Reverberations in the source and receiver hole prevented the subtraction of the incident wavefield and therefore, the subsequent windowing of traces muted near field scattering as well. A better procedure in subtracting the incident field, e.g. cross correlating the first pulse of a numerically calculated representation of the incident field with the field data and subsequent scaling before the synthetic field is subtracted, should improve the result. Anelastic attenuation is a substantial problem in amplitude inversion. It should be corrected for, if the Green function cannot account for it, although the determination of α seems problematic. A promising procedure in the present approach is the application of a complex Green function to solve for the real and imaginary parts of the

elastic parameters simultaneously, as presented in Chapter 3.5. However, the present example would require a large capacity in computing power, as, in addition to the 39 source and receiver combinations, the number of unknowns would increase from 3 to 5 per voxel. In this case, a reduction from 39 sources and 39 receivers to 20 each could solve the computational constrains, however, it would reduce the resolving power for the model parameters as well, as the number of unknowns is increased while simultaneously the number of equations is reduced. An additional problem is the lack of S wave anisotropy information. As it is obvious by the difference between Figure 4.7 and Figure 4.9, anisotropy has a major effect on the inversion result. One possible approach is to recover the S wave anisotropy from the P wave anisotropy, assuming this quantity is known, which is a likely the case for many experimental geometries. The incorporation of S wave anisotropy should improve the results for the P to S scattered phases. Furthermore, the inversion was limited to wavelengths closer to the Mie than to the Rayleigh scattering range, as the amplitudes associated with low frequencies did not show enough resolving power. However, future applications of broad band technology should provide data with higher energy in the low frequency range.

Chapter 5

Summary

The presented thesis was intented to investigate two areas of elastic wave scattering. The scattering of elastic waves by an inhomogeneity, and subsequently the inversion of these waves to solve for the elastic parameters of the inhomogeneity. Both parts provide a general approach by keeping the results in a general format, and the techniques are applicable to discretionary geometries. The results should be useful for the evaluation of experiments in their planning stage.

In the first part, the problem of low frequency elastic wave scattering by an inclusion was investigated. The low frequency approximation is based on an exact solution for the scattering of elastic waves by a sphere, and therefore, the exact solution was used to evaluate the low frequency approximation under various conditions. The Rayleigh approximation is a useful tool to linearize the problem of elastic wave scattering, and therefore, it often is applied to solve the inverse problem. However, no limits of the approximation had been established thus far, as most of the assumptions were based on strong inequalities, and therefore it was intented to determine bounds for its validity range.

The presented Rayleigh approximation produces excellent results within its validity range. The comparison to the generally used Rayleigh approximation, containing far field terms only, revealed that near field terms play an important role for the evaluation of scattered amplitudes. Within a distance of 2 times the wavelength of the incident wavefield from the inhomogeneity, P and S waves cannot be separated and the scattered amplitudes are up to a magnitude of ≈ 300 times larger than at a distance of 2λ. Therefore the use of the far field

Rayleigh approximation will produce wrong results if applied in this situation, which may arise during crosshole experiments or during the investigation of near surface heterogeneities.

The nonlinear Rayleigh approximation was compared to its linearized and quadratic approximation. It was found that the relative error for these strongly depends on the scattering angle. The $\hat{r}$-component reveals the largest error for forward scattering, whereas the $\hat{\theta}$-component has the largest deviations for a scattering angle of 45°. It was found that the quadratic approximation reduces the error by a factor of 5 over the linear approximation. The result helps to estimate the relative error based on the use of the linearized Rayleigh approximation if the locations of source, scatterer, and receiver are known for a planned experiment.

The relative error of the linear Rayleigh approximation not only depends on the scattering angle but is a function of the parameter perturbation as well. This functional dependence was investigated and produced results that allow an application for larger deviations than previously assumed. Reliable result should be obtained for perturbations up to 20%. However, the dependence of the relative error on the parameter perturbation reveals an asymmetry with respect to the origin, in that the increase for the error is larger in positive than for negative perturbations.

In the past inequalities were used to restrict the Rayleigh limit to values much smaller than unity ($k_p R \ll 1$). However, the Rayleigh limit not only is a function of the incident wavelength and the dimensions of the inhomogeneity, but also depends on the elastic parameters. The dependence of the Rayleigh limit as a function of perturbation in the elastic parameters was investigated and surprisingly high values were found, reaching up to ($k_p R = 0.9$). This opens a broader range for the applicability of elastic wave Rayleigh scattering.

The surprising results established for the Rayleigh scattering process were investigated in relation to their effects in the inversion of scattered waves. Near field effects have to be considered in a crosshole situation where the exact location of the inhomogeneity may fall within a distance of 2λ of the receiver

borehole. In addition, features extending beyond the target area may intersect either borehole and therefore, the lack of near field terms would produce unreliable or false images close to the wells, where the performance of the inversion could be tested by correlating borehole properties with inversion results in the proximity of the wells. The extension of the Rayleigh limit to larger values could help to reduce the computational expenses, since the parametrization of the medium can be coarser with respect to the wavelength of the incident field.

At first, however, a method was presented to solve the inherently nonlinear scattering problem in a direct way. The solution was linearly expressed in terms of moments that decompose the scatterer into three types of force terms, each accounting for the change in one of the elastic parameters. These parameters, although they exhibit a nonlinear dependence on the moments, can be directly recovered based on the symmetry of the scatterer, and therefore, the scattering problem can be solved in an exact direct way. This allows inversion of strong inhomogeneities directly, avoiding time consuming iterations which can only approximate the magnitude of the anomaly.

The nonlinear dependence of the elastic parameters on the moments was performed covering the whole parameter range from a cavity to a rigid inclusion. The dependence is highly nonlinear and very sensitive to large positive deviations, where small changes in the moments cause large variations in the deviation of the elastic parameters. For negative values of the moments, however, the relationship becomes almost linear, but the perturbation in the elastic parameters become almost insensitive to large changes in the moments. Thus it could prove difficult to distinguish between a cavity and a low density yet solid inhomogeneity.

Based on this solution, the effect of near field terms was investigated using a numerical example which models a crosshole geometry. It was found that the Green function containing near field terms returned an almost perfect inversion result, whereas a Green function containing far field terms only produces erroneous magnitudes and locations for the anomaly. However, the model resolution was equally good in both cases, which could lead to wrong interpretations of

the far field Green function results. For the case of the correct Green function, the model resolution was improved to unity for all three parameters by adding one receiver each at the top and bottom of the model area. These receivers improved the angular coverage of the parametrized zone, which is essential for good results in the case of elastic wave scattering.

The influence of source and receiver geometry on the success of an inversion for the location of a strong scatterer was presented for the case of a cavity. It was found that the distinct pattern of scattered energy (P to P scattering under 180°, P to S scattering under 135°) prevented the successful recovery of the image for most geometries, and only a reflection survey, set up to record both P and S scattered phases, proved successful in determining the location and parameters of the cavity. Therefore, it was shown that, prior to a field experiment, the scattering properties of the object have to be thoroughly studied to find the optimum geometry for a successful survey.

The numerical investigation of a small single scatterer with an anomaly in density only, where different Green functions had been used for the forward modeling and the inversion, revealed that in the absence of the incident wave it is possible to retrieve the location and the amplitudes of the inhomogeneity. However, the incident field, due to its large amplitudes in relation to the scattered field and the coincidence in travel time, had to be removed first. It was shown that correlation between the parameters introduced weak anomalies for the less constrained bulk modulus. However, these were almost comparable to the noise level and therefore negligible.

The final chapter applied the inversion technique to the case of a fracture zone in an underground field laboratory. The purpose was to determine whether it is possible to model a fractured zone by an ensemble of point scatterers which would provide a technique to parametrize scatterers of any shape for the future application of this technique. Under this assumption the location and, if possible, the elastic parameters of this highly fractured zone had to be estimated.

Before the inversion was performed the wavefield was corrected for several

effects not related to the scattering process. The source and receiver parameters, describing the coupling to the borehole walls were determined using a least squares inversion approach of the first arrival amplitudes. The results related to the geology encountered in the boreholes indicated that the fracture zone is not a homogeneous feature, but probably consists of three zones; two of which showed a high degree of fracturing at each side of the shaded fracture zone in Figure 4.1, whereas the center section revealed a more homogeneous composition. The same inversion produced a very high background attenuation of $\alpha = 0.36m^{-1}$ for a frequency of 10 KHz. Although the magnitude of this value seems questionable, the high degree of foliation in the host rock will have a severe attenuation effect on wave propagation. Although an attempt was made to subtract the incident field from the data after these correction were applied, it proved unsuccessful, and therefore the beginning and the end of the traces were muted.

The inversion of the data was performed for an isotropic and an anisotropic background medium. The anisotropic model produced reasonable results that could be related to the encountered geology. It was found, however, that the fracture zone does not constitutes a good scatterer and produced a blurry image in the moduli. This may be caused by a gradual change in properties from the host rock to the fractured medium. In contrast, the inversion seems to have detected an additional observation well traversing the study area, as well as a suture zone between two different types of host rock. Both features seem to be stronger scatterers for elastic waves, the borehole because of its strong negative anomaly and the suture zone because of the welded contact, which is the most probable between the two rock types. Displaying the same results in terms of the P and S wave velocities as well as the V_s/V_p ratio, it became evident that different structures appeared in the plots. The amplitude of the small features (borehole and suture zone) were suppressed and the fracture zone became apparent with negative perturbations in the velocities. This confirms results discussed earlier that different physical parameters are each sensitive to different types of inhomogeneities.

The isotropic inversion produced no meaningful results, as all linear features were reduced to block shaped structures. The lack of directionality in the velocities makes it impossible to recover stretched linear features, which, as for the case of the fracture zone, strike parallel to the direction of maximum velocity. Only the data that were not corrected for elastic attenuation provided a reasonable image after the inversion. This implies that the attenuation, which is probably highest in the fracture zone, added information to the data which helped to reconstruct the image. Since S wave anisotropy could not be accounted for, the inversion result is likely to improve if these data becomes available, since P to S scattered phases could not be correctly located in the present example.

The overall result of the inversion raises hope for future applications. Although a fracture zone is not a perfect target for the inversion of scattered waves, it was shown that it is possible to decompose it into an ensemble of point scatterers. The nonlinear approach appears to produce reliable results in the case of a strong scatterer as shown by the probable detection of a third borehole.

Future improvements in the extraction of the incident wavefield and an improved estimation of the background parameters, including anisotropy, should produce better results. The correct subtraction of the incident wave would leave near field scattered phases in the data, which are important to resolve the structure close to the receivers. An increase in resolving power for low frequencies can be expected from applications of broad band technologies, which are currently introduced in many applications of observational seismology. At the same time, improvements in source technology, particular in borehole applications, are desirable, which could produce source signals capable of transmitting a constant amplitude level over a frequency band of at least two magnitudes. It remains to be seen how the inversion performs for the reconstruction of other classes of inhomogeneities, especially strong scattering objects (e.g. cavities). However, the work presented in this thesis indicates that successful results can be expected, as the treatment of large scattered amplitudes associated with

these objects proved successful in the numerical experiments, and therefore, it should produce better results than other techniques that have been applied in the past, which rely on linear approximations of the problem.

References

Aki, K. , 1969. Analysis of the seismic coda of local earthquakes as scattered waves, *J. Geophys. Res.*, 74, 615-631.

Aki, K. , 1980. Attenuation of shear waves in the lithosphere for frequencies from 0.05 to 25 Hz, *Phys. Earth Planet. Inter.*, 21, 50-60.

Aki, K. and Chouet B., 1975, Origin of coda-waves : source, attenuation and scattering effects, *J. Geophys. Res.*, 80, 3322-3342.

Aki, K. and W. H. K. Lee, 1976, Determination of three-dimensional velocity anomalies under a seismic array using first P arrival times from local earthquakes, 1, A homogeneous initial model, *J. Geophys. Res.*, 81, 4381-4399.

Côte, P., Degauque, P., Lagabrielle, R. and Levent, N., 1995, Detection of underground cavities with monofrequency eletromagnetic tomography between boreholes in the frequency range 100 MHz to 1 GHz, *Geophys. Pros.*, 43, 1083-1107.

Devaney, A. J., 1984, Geophysical diffraction tomography, *IEEE Trans. Geosci. Remote Sensing*, GE-22, 3-13.

Doornbos, D. J., 1976, Characteristics of lower mantle inhomogeneities from scattered waves, *Geoph. J. R. A. Soc.*, 44, 447-470.

Frankel, A., 1991, Mechanisms of seismic attenuation in the crust: scattering and anelasticity in New York State, South Africa, and Southern California, *J. Geoph. Res.*, **96**, 6269-6289.

Frankel, A. and Clayton, R.W., 1986 , Finite difference simulations of seismic scattering : Implications for the propagation of short-period seismic waves in the crust and models of crustal heterogeneity, *J. Geoph. Res.*, **91**, 6465-6489.

Frankel, A. and Wennerberg, L., 1987, Energy-flux model of seismic coda : separation of scattering and intrinsic attenuation, *Bull. of Seismol. Soc. Am.*, *77*, 1223-1251.

Gritto R., Korneev V. A. and Johnson L. R., 1995 a, Low-frequency elastic-wave scattering by an inclusion: limits of applications, *Geophys. J. Int.*, **120**, 677-692.

Gritto R., Kaelin B. and Johnson L. R., 1995 b, Analysis of crustal heterogeneity with application to wave propagation at the KTB site, *Geophysics*, submitted.

Haddon, R. A. W. and Cleary, J. R., 1974, Evidence for scattering of seismic PKP waves near the mantle-core boundary, *Phys. Earth Planet. Inter.*, 8, 211-234.

Herraiz, M. and Espinosa, A. F., 1987, Coda Waves: A Review, *PAGEOPH*, 25, 499-577.

Hudson, J. A. and Heritage, J. R., 1981. The use of the Born approximation in the seismic scattering problem, *Geophys. J. R. Astron. Soc.*, **66**, 221-240.

Korn, M., 1990, A modified energy flux model for lithospheric scattering of teleseismic body waves, *Geophys. J. Int.*, **102**, 165-175.

Korneev, V. A., and Johnson, L. R., 1993 a, Scattering of elastic waves by a spherical inclusion - 1. Theory and numerical results, *Geophys. J. Int.*, **115**, 230-250.

Korneev, V. A., and Johnson, L. R., 1993 b, Scattering of elastic waves by a spherical inclusion - 2. Limitation of asymptotic solutions, *Geophys. J. Int.*, **115**, 251-263.

Lees, J. M. and Lindey, G. T., 1994, Three-dimensional attenuation tomography at Loma Prieta: inversion of t* for Q, *J. Geoph. Res.*, **99**, 6843-6863.

Lo, T. W., Toksöz, M. N., Xu S. H., and Wu R. S., 1988, Ultrasonic laboratory tests of geophysical tomographic recontruction, *Geophysics*, **53**, 947-956.

Majer, E. L., Myer, L. R., Peterson, J. E., Karasaki, K., Long, J. C. S., Martel, S. J., Blümling P., and Vomvoris, S., 1990, Joint seismic, hyrological, and geomechanical investigations of a fracture zone in the Grimsel rock laboratory, Switzerland, NAGRA-DOE Cooperative Project Report, pp. 173.

Michelini, A. and McEvilly T. V., 1991, Seismological studies as Parkfield: I. Simultaneous inversion for the velocity structure and hypocenters using cubic b-splines parametrization, *Bull. Seismol. Soc. Am*, **81**, 524-552.

Nolet, G. (ed.), 1987, S&EG Seismic Tomography, *D. Reidel Publishing Com-*

pany.

Peterson, J. E., 1986, The application of algebraic reconstruction techniques to geophysical problems, Ph.D. Thesis, University of California at Berkeley.

Richards, P. G. and Menke, W., 1983, The apparent attenuation of a scattering medium, *Bull. of Seism. Soc. Am.*, **73**, 1005-1021.

Romero A. E., 1995, Application of seismic tomographic techniques in the investigation of goethermal systems, Ph.D. Thesis, University of California at Berkeley.

Romero A. E. Jr., McEvilly T. V., Majer E. L. and Michelini A., 1993, Velocity structure of the Long Valley caldera from the inversion of local earthquake P and S travel times, *J. Geophys. Res.*, **98**, 19869-19879.

Sams, M. and Goldberg, D., 1990, The validity of Q estimates from borehole date using spectral ratios, *Geophysics*, **55**, 97-101.

Sato, H., 1984. Attenuation and envelope formation of three-component seismograms of small local earthquakes in randomly inhomogeneous lithosphere, *J. Geophys. Res.*, **89**, 1221-1241.

Scherbaum, F., 1990, Combined inversion for the three-dimensional Q structure and source parameters using microearthquake spectra, *J. Geophys. Res.*, **95**, 12423-12438.

Shapiro, S. A. and Zien H., 1993, The O'Doherty-Anstey formula and localization of seismic waves, *Geophysics*, **58**, 736-740.

Tarantola A., 1986, A strategy for nonlinear elastic inversion of seismic reflection

data, *Geophysics*, **51**, 1893-1903.

Toomey, D. R. and Foulger G. R., 1989, Tomographic inversion of local earthquake data from the Hengill-Grensdalur Central Volcano Complex, Island, *J. Geoph. Res.*, **94**, 17497-17510.

Tura, M. A. C., 1990, Acoustic and elastic diffraction tomography and its application to fracture detection, Ph.D. Thesis, University of California at Berkeley.

Tura, M. A. C., Johnson L. R., Major E. L. and Peterson J. E. Jr., 1992, Application of diffraction tomography to fracture detection, *Geophysics*, **57**, 245-257.

Tura, M. A. C., Johnson L. R., 1993, A stable method for linearized inversion of elastic parameters, *Geophys. J. Int.*, **115**, 1-13.

Tygel, M., Schleicher, J., and Hubral P., 1994, Kirchhoff-Helmholtz theory in modeling and migration, *J. Seis. Expl.*, **3**, 203-214.

Vasco, D. W., Peterson J. E. Jr. and Major E. L., 1995, A simultaneous inversion of seismic travel time and amplitudes for velocity and attenuation, *Geophysics*, in press.

Vasco, D. W., Peterson J. E. Jr. and Major E. L., 1995, Beyond ray tomography: Wavepaths and fresnel volumes, *Geophysics*, **60**, 1790-1804.

White, B., Sheng P. and Nair B., 1990, Localization and backscattering spectrum of seismic waves in stratified lithology, *Geophysics*, **55**, 1158-1165.

White, B., Sheng P., Zang Z. Q. and Papanicolaou G., 1987, Wave localization

characteristics in the time domain, *Phys. Rev. Let.*, **63**, 1918-1921.

Woodward, M. J., 1992, Wave-equation tomography, *Geophysics*, **57**, 15-26.

Wu, R. S., 1982. Attenuation of short period seismic waves due to scattering, *Geoph. Res. Let.*, **9**, 9-12.

Wu, R. S. and Aki, K., 1985. Scattering characteristics of elastic waves by an elastic heterogeneity, *Geophysics*, **50**, 582-595.

Wu, R. and Toksöz, M. N., 1988. Diffraction tomography and multisource holography applied to sesimic imaging, *Geophysics*, **52**, 11-25.

Yilmaz, Ö, 1987, Seismic data processing, Society of exploration geophysicists, Chapter 4, 241-353.

Zucca J. J., Kasameyer, P. W. and Mills J. M. Jr., 1987, Observation of a reflection from the base of a magma chamber in Long Valley Caldera, California, *Bull. Seis. Soc. Am.*, **77**, 1674-1687.